EVALUATION OF AN IN-LINE PHASE-CONTRAST AND PHASE SHIFT DIGITAL TOMOSYNTHESIS SYSTEM

By

Jeffrey C. Hammonds

Dissertation

Submitted to the Faculty of the
Graduate School of Vanderbilt University
in partial fulfillment of the requirements
for the degree of

DOCTOR OF PHILOSOPHY

in

Physics

August, 2013

Nashville, Tennessee

Approved:

Professor Ronald Price

Professor Edwin Donnelly

Professor David Ernst

Professor Todd Peterson

Professor David Pickens

Professor Michael Stabin

To my parents who have supported me throughout this long journey.

ACKNOWLEDGEMENTS

First and foremost, I must thank my committee chair Dr. Price. He is the most passionate scientist that I have met and has provided generous advice and support to me all throughout my research. I would also like to thank Dr. Pickens and Dr. Donnelly who have both provided their insight and expertise in all things from theory to experiment to programming. I also like to thank my other committee members (Dr. Ernst, Dr. Peterson, and Dr. Stabin) for their feedback and dissertation advice.

Of course, I could not have stayed sane throughout my journey without the help of my friends: Gilma Adunas, Jessica Clark, Lisa Genovese, Hye-Jeong Lee, Ken Lewis, Heungman Park, and Subechhya Pradhan. Spending time with you talking, eating, hanging out and commiserating made the hard days bearable and the good days very enjoyable.

I would also like to take this opportunity to thank all my physics, math and engineering teachers since high school, in undergraduate and graduate school. They have instilled in me the love for learning and the urge to learn even more. Thanks also goes to Dr. Schriver for motivating me to become a better teacher and helping me to get there through teaching a wide variety of classes. I would also like to thank all of the students I had the opportunity to teach during my years as a T.A.

TABLE OF CONTENTS

List of Tables

List of Figures

Chapter I

Introduction

I.1 Planar X-ray Imaging

I.1.1 Traditional X-ray Attenuation

On November 8, 1895, Wilhelm Roentgen discovered x-rays [1]. Since then, x-ray imaging has become an important method for non-invasively examining the internal structures of both biological and non-biological specimens. The creation of an x-ray image entails the placement of the x-ray source on one side of the specimen and an x-ray detector on the other side. The x-rays are produced for a period of time by the x-ray source and travel through the specimen to the detector as shown in Figure 1.1 [2].

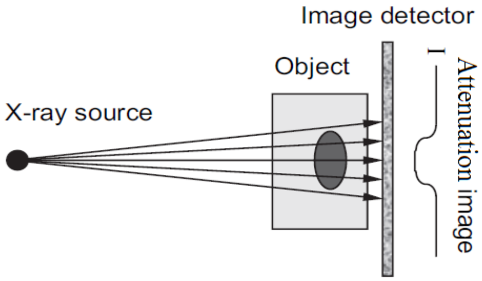

Figure 1.1: Projection radiograph of a compound object producing an attenuation image with an intensity profile I. Adapted from [2].

Within the specimen, some x-rays interact with the specimen's internal composition while other x-rays pass through onto the detector where the x-ray image is formed. Internal interactions take the form of x-ray absorption and scattering and collectively are labeled as attenuation. Since different internal components will in general absorb and scatter x-rays differently, the x-ray image is an image of the differential attenuation of the incident x-ray beam within that specimen. This form of x-ray imaging is called projection (or sometimes planar, absorption, contact or conventional) radiography in that the image produced is a two-dimensional projection of the specimen's three-dimensional attenuation properties.

I.1.2 Limitations in Attenuation X-ray Imaging

Although the utility of x-ray projection imaging was readily apparent, there are two significant image quality limitations: low-contrast and structural overlay. As described above, a projection radiographic image is a two-dimensional projection of a specimen's three-dimensional attenuation properties. The contrast that arises within the radiographic image is due to non-negligible differential attenuation between the internal components. However, if the internal components have similar attenuation properties then the image contrast will be negligible. Additionally, there could be considerable structural overlap within the radiographic image due to the complex internal nature of the specimen.

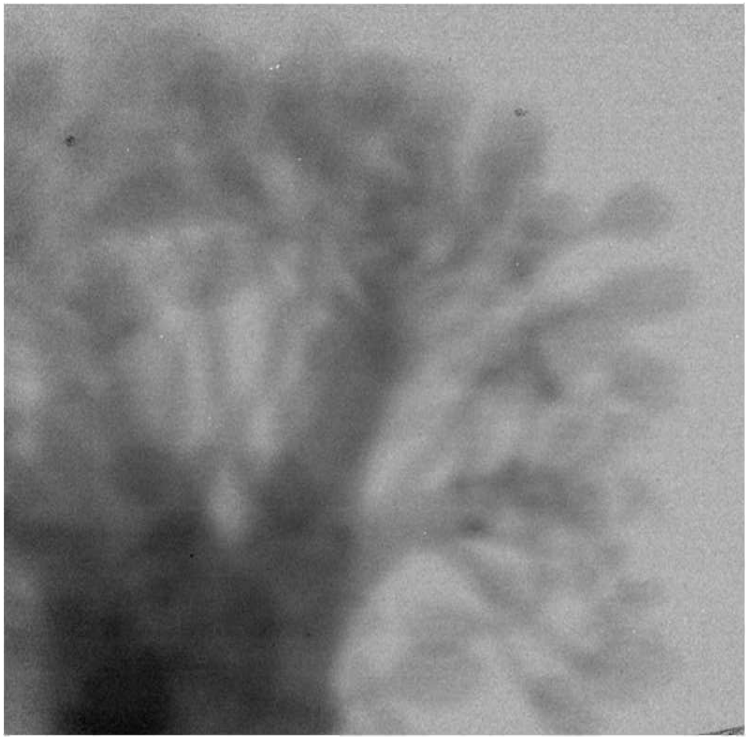

Figure 1.2: Attenuation radiograph of a partial head of broccoli.

Figure 1.2 was obtained using a nominal 50 μm focal spot size resulting in a conventional attenuation image. As can be seen in Figure 1.2, there is low-contrast between the broccoli bulbs and the surrounding air. In the central portion of this figure, there is structural overlap of the broccoli stems. From this radiographic image, it is impossible to resolve the structure of most of the individual stems.

I.1.3 Phase-contrast Radiography

Phase-contrast radiography has been proposed as a potential method for improving contrast sensitivity specifically in objects composed of materials with similar attenuation properties. Phase-contrast radiography differs from attenuation radiography in that it does not rely solely on the differential attenuation of x-rays for image formation. Instead, it also relies upon interference effects due to the differential phase shifts that the x-rays experience as they pass through different materials.

A phase-contrast radiograph may be produced using a partially-coherent, small focal spot x-ray source with a non-zero object-to-detector distance (R_2). As illustrated in Figure 1.3, an intensity

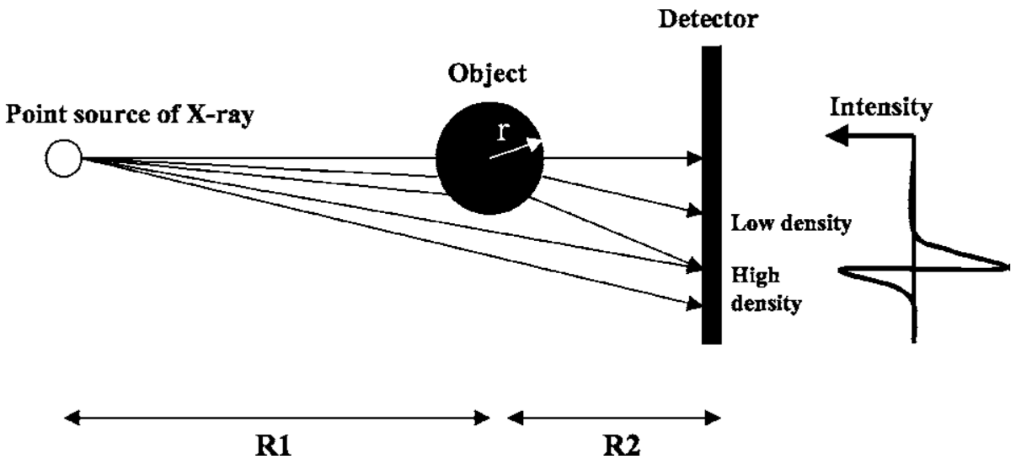

Figure 1.3: Phase-contrast image formation of a homogeneous object embedded in air with a source-to-object distance R_1 and an object-to-detector distance R_2. Since x-rays refract in the opposite direction as that of visible light, there is greater intensity just outside the object's edge and lesser intensity just inside the object's edge. This results in an edge enhancement or edge effect. Adapted from [3].

variation can be created from the interference of phase-shifted x-rays that originate from within the object and the non phase-shifted x-rays from the source [3]. This intensity variation shows both constructive and destructive interference effects occurring at the edge of the object resulting in enhanced visualization of the object's boundary. Thus, for similarly attenuating materials adjacent to one another, phase-contrast radiography's edge enhancement may allow one to discern individual objects that could not be distinguished with an attenuation radiograph [4]. Figure 1.4 is a phase-contrast image of the same broccoli head as in Figure 1.2. In this figure, one can clearly delineate the broccoli bulbs' edges.

This edge enhancement effect may be quantified by using the edge enhancement index (EEI). The EEI measures the "relationship of the edge enhancement effect relative to the absolute change in intensity from absorption differences across the edge" [24]. The EEI is given by the following formula:

$$EEI = \frac{\left(\frac{P-T}{P+T}\right)}{\left(\frac{H-L}{H+L}\right)} \tag{1.1}$$

where P and T are the peak and trough intensity values at the edge and H and L are the average values from the high and low intensity regions adjacent to the edge. Figure 1.5 illustrates the EEI

Figure 1.4: Phase-contrast radiograph of a partial head of broccoli.

variables:

Some potential medical applications for phase-contrast radiographs that have been described previously are:

- Vascular Imaging: Phase-contrast imaging has been used to resolve approximately 30 μm diameter blood vessels in a rat liver by using physiological saline as a contrast agent and approximately 50 μm diameter blood vessels in a mouse liver without using a contrast agent whereas attenuation x-ray imaging was unable to discern this diameter of vascularity [5, 6].
- Muscloskeletal Imaging: It is also now possible to visualize cartilage abnormalities associated with the initial stages of joint disease or osteoarthritis with phase-contrast imaging whereas

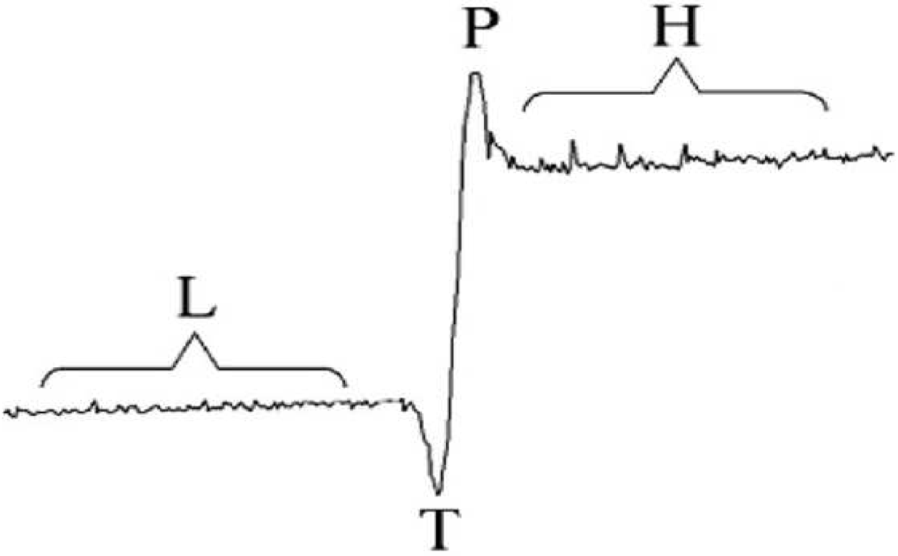

Figure 1.5: Edge Enhancement Index. Adapted from [24].

attenuation x-ray imaging is only sensitive in the advanced stage where there has already been a loss of cartilage [7, 8].

- Pulmonary Imaging: In the case of lung imaging, attenuation radiography has had limited success in detecting the early stages of lung disease. Also, it can sometimes show normal chest radiographs even in the advanced stages of interstitial lung disease [9]. However, with the air-tissue interface, phase-contrast imaging could be used to improve lung imaging as has been shown in the radiographs of mice and rabbit lungs [10, 11].
- Breast Cancer Imaging: The use of attenuation radiography in systematic screening for breast cancer has been limited due to the weak attenuation contrast found in differentiating soft tissues, especially between normal and abnormal breast tissues at small scale [12]. Techniques involving phase-contrast imaging have been developed to visualize the microstructures of soft biological tissues with low radiation doses for mammography applications [13–18].

I.1.3.1 Physical Origins of the Phase-Contrast Effects

Assume there is an incident electromagnetic wave (whose speed in vacuum is c and wavelength is on the order of the atomic dimensions) impinging upon a medium containing many atoms. The interaction of the electromagnetic wave with a medium will result in reflected, transmitted, and scattered waves. If we restrict ourselves to only the forward scattered wave, then the sum of the forward scattered waves from all the atoms and the unscattered incident wave together produce an electromagnetic wave differing in phase compared with the incident wave. This resultant wave passes through the medium with a modified phase-velocity and it is this modified phase-velocity that is the source of the edge enhancement effects seen in a phase-contrast radiograph [19]. This modified phase-velocity (v_ϕ) is given by the formula

$$v_\phi = \frac{c}{n\left(\omega\right)} \tag{1.2}$$

where c is the speed of light in a vacuum and $n\left(\omega\right)$ is the index of refraction of the medium as a function of the incident electromagnetic wave's angular frequency.

The index of refraction can be written as

$$n\left(\omega\right) = 1 - \frac{r_e \lambda^2}{2\pi} \sum_a n_a \left[f^0_{r,a}\left(\omega\right) - i f^0_{i,a}\left(\omega\right)\right] \tag{1.3}$$

where n_a is the electron number per unit volume for element a, r_e is the classical electron radius, λ is the vacuum wavelength, $f^0_{r,a}$ and $f^0_{i,a}$ are the real and imaginary parts of the atomic scattering factor for element a respectively and the sum is taken over all the different types of atoms present in the medium [19, 20]. The real and imaginary parts of atomic scattering factor, $f^0_r\left(\omega\right)$ and $f^0_i\left(\omega\right)$, have been tabulated for all elements from hydrogen to uranium at photon energies from 50 eV to 30 keV for $f^0_r\left(\omega\right)$ and 10 eV to 30 keV for $f^0_i\left(\omega\right)$ [21]. After distributing the constants through, the last two terms in the index of refraction can be rewritten as

$$\delta\left(\omega\right) = \frac{r_e \lambda^2}{2\pi} \sum_a n_a f^0_{r,a}\left(\omega\right) \tag{1.4}$$

$$\beta\left(\omega\right) = \frac{r_e \lambda^2}{2\pi} \sum_a n_a f^0_{i,a}\left(\omega\right) \tag{1.5}$$

Thus the index of refraction can now be expressed as

$$n\left(\omega\right) = 1 - \delta\left(\omega\right) + i\beta\left(\omega\right) \tag{1.6}$$

where $\delta\left(\omega\right)$ is the decrement of the real part of the refractive index that characterizes the phase shifting property and the imaginary part $\beta\left(\omega\right)$ characterizes the attenuation property of the material. The origin of phase shifting is due to a separate material property different from the material's attenuation property. This separation has a potential benefit in that, unlike conventional radiography which relies solely upon the attenuation of x-rays to create image contrast, there is no radiation absorption involved in the production of the edge enhancement.

In addition to $\delta\left(\omega\right)$ and $\beta\left(\omega\right)$, the complex atomic scattering factors may be used to define the atomic absorption cross-section and an analogous atomic phase cross-section [22]:

$$\sigma_{abs}\left(\omega\right) = 2r_e\lambda\sum_a f^0_{i,a}\left(\omega\right) \tag{1.7}$$

$$\sigma_{phase}\left(\omega\right) = 2r_e\lambda\sum_a f^0_{r,a}\left(\omega\right). \tag{1.8}$$

The ratio of σ_{phase} to σ_{abs} can be found using the values of the complex atomic scattering factors obtained at 30 keV for various biologically relevant elements as seen in the following table [21]:

Table 1.1: Absorption and Phase Cross-Sections for Biological Elements at 30 keV.

Element	Z	f^0_r	f^0_i	σ_{abs} [m^2]	σ_{phase} [m^2]	$\frac{\sigma_{phase}}{\sigma_{abs}}$
H	1	1.00	4.40×10^{-8}	1.02×10^{-32}	2.32×10^{-25}	2.27×10^{7}
C	6	6.00	4.43×10^{-4}	1.03×10^{-28}	1.40×10^{-24}	1.35×10^{4}
N	7	7.00	9.39×10^{-4}	2.19×10^{-28}	1.63×10^{-24}	7.45×10^{3}
O	8	8.00	1.81×10^{-3}	4.22×10^{-28}	1.86×10^{-24}	4.42×10^{3}
Ca	20	20.1	1.08×10^{-1}	2.52×10^{-26}	4.68×10^{-24}	1.86×10^{2}

As can be seen from Table 1.1, the ratio indicates at least a factor of three orders of magnitude increase in the phase cross-section (σ_{phase}) over the absorption cross-section (σ_{abs}) at this keV value for the lighter elements (H, C, N and O) that make up soft tissue. Phase-contrast imaging has the potential to offer an improvement in the detection of soft tissue masses over conventional attenuation imaging. However, for the heavier element (Ca), phase-contrast imaging may not show as much an improvement over conventional attenuation imaging.

I.1.4 Experimental Factors Effect Upon Phase-Contrast

I.1.4.1 Temporal or Longitudinal Coherence

Temporal or longitudinal coherence relates directly to the finite frequency bandwidth of the source. Thus it is a measure of the monochromaticity of the x-ray beam. Early (as well as some current) investigators in phase-contrast imaging used x-ray sources with accompanying monochromator crystals to obtain quasi-monochromatic radiation capable of producing interference effects [4, 7, 8, 13–17, 23]. A monochromator is a near perfect crystal consisting of parallel planes of lattice points called Bragg planes. Crystals have different Bragg planes depending upon which groups of lattice points are used to define the Bragg plane.

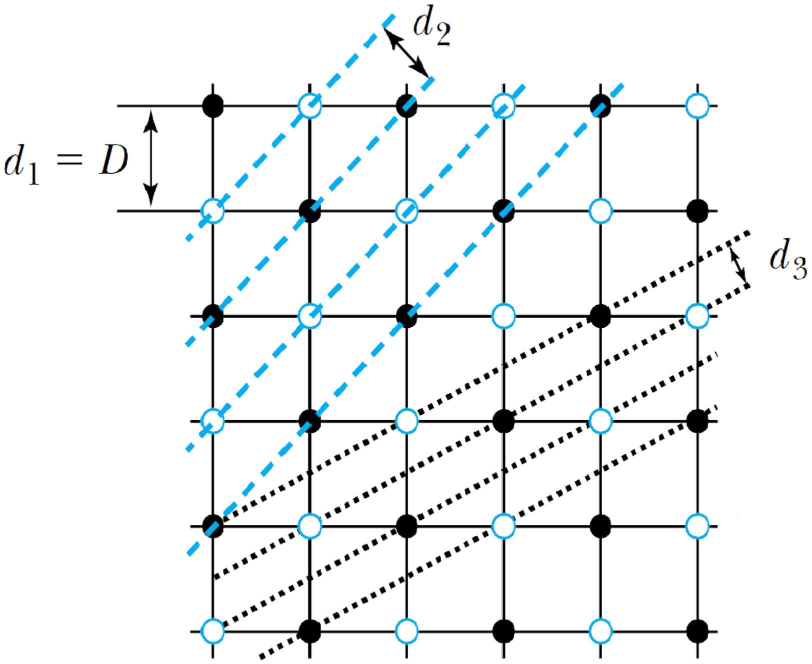

Figure 1.6: Crystal lattice with three different Bragg planes. Adapted from [26].

In Figure 1.6, D represents the interatomic spacing and d_i for $i = 1, 2, 3$ represents the distance between particular Bragg planes [26]. X-rays that are scattered at equal angles from two lattice points in different Bragg planes will be in phase only if the difference in their path lengths is an integral number of wavelengths. This is known as the Bragg condition and is given by:

$$2d_i \sin\theta = m\lambda_i \tag{1.9}$$

where λ is the x-ray wavelength and m is an integer. The Bragg condition is graphically represented in Figure 1.7.

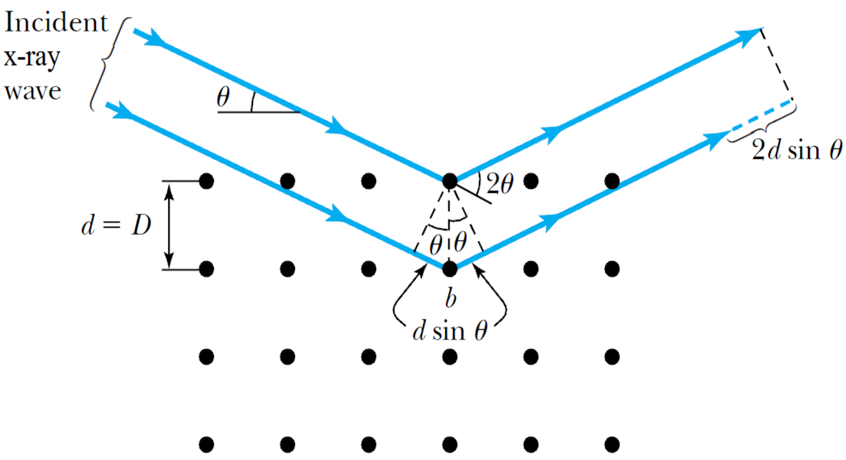

Figure 1.7: Bragg Condition. Adapted from [26].

Ideally, depending upon which Bragg plane is used, a unique x-ray wavelength can be chosen, thus creating a true monochromatic x-ray beam. In reality, a small range of x-ray wavelengths are created and a quasi-monochromatic x-ray beam is produced. To further reduce the spread of x-ray wavelengths, a second monochromator (with its Bragg planes aligned with the first monochromator's Bragg planes) is typically used as an incident crystal for the first monochromator's exit x-ray beam. While a monochromator (or dual-monochromator) can provide a quasi-monochromatic beam, it has been shown that this is not necessary for phase-contrast imaging [27]. Additionally, there are certain difficulties to using monochromator crystals such as obtaining near perfect crystals, aligning the crystals' Bragg planes (for dual monochromator use), the loss of x-ray flux that does not meet the Bragg condition and crystal overheating from a synchrotron source [28].

I.1.4.2 Lateral or Spatial Coherence

Lateral or spatial coherence relates directly to the finite spatial extent of the source. Two point radiators on an x-ray source, separated by a distance that is larger than the x-ray wavelength, will in general have no phase correlation between their respective emitted x-rays. This is especially true for distances close to the source; however farther away from the source, phase correlation can be achieved between two laterally spaced points in the x-ray field. To quantify this correlation, the spatial coherence length is given as

$$L_{\text{coh}} = \frac{\lambda R_1}{f} \tag{1.10}$$

where L_{coh} is the spatial coherence length, λ is the wavelength of the radiation, R_1 is the distance from the source to the point where the spatial coherence length is to be measured, and f is the focal spot size of the x-ray source [24]. The points along the spatial coherence length are in phase with each other and are capable of producing interference effects. The advantage of spatial coherence is that it does not require any monochromator crystals. This allows for the use of a polychromatic x-ray source such as a conventional x-ray tube. The spatial coherence length for a polychromatic source could be modified to allow λ to represent a weighted sum of x-ray wavelengths [24].

I.1.4.3 Source-to-Object Distance (SOD or R_1)

Since equation (1.10) provides no constraints on the size of R_1, it seems reasonable to expect the achievement of any desirable spatial coherent length by simply increasing R_1 (keeping all else constant). However, there are two disadvantages to increasing R_1 to an arbitrary amount. First, it may not be physically possible to increase R_1 due to limitations imposed by where the phase-contrast imaging unit is housed. The second disadvantage manifest itself in the form of the inverse square law which is a consequence of the conservation of energy principle. The inverse square law states that the intensity or irradiance at a point a distance R_1 from the radiation source is proportional to the inverse square of R_1. Thus larger values of R_1 will result in a smaller x-ray intensity that is available to image an object. This in turn would require longer lengths of exposure time leading to increase dose deposition to the object and possible motion blur.

I.1.4.4 Focal Spot Size

In addition to the limitation placed on R_1 by the intensity decrease due to the inverse square law, there is also an intensity limitation due to the size of the x-ray focal spot size f. The smaller the x-ray focal spot, the less x-ray output intensity is produced. However, this limitation is not due to any physical principle but due to current heat-dissipation technology used to manufacture x-ray tubes. Should future advances in x-ray tube design allow for a higher output than that currently available, a larger spatial coherence length or compensation for the inverse square law can be achieved.

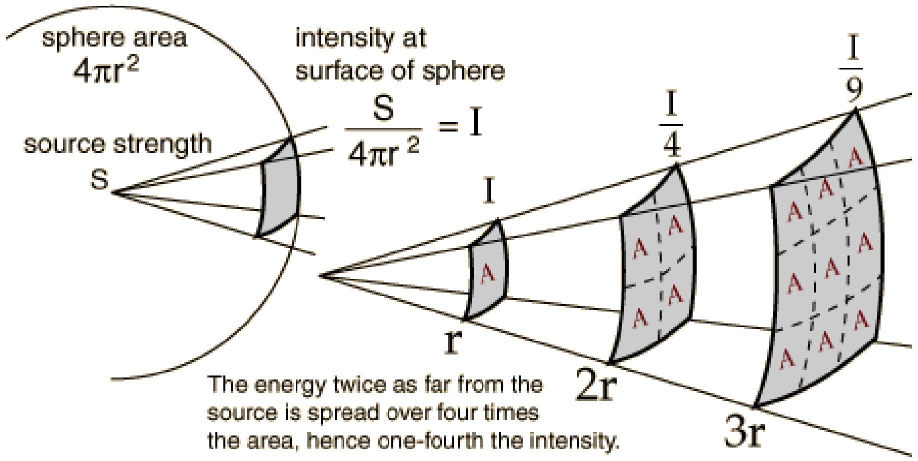

Figure 1.8: Inverse Square Law. Adapted from [31].

I.1.4.5 Object-to-Image Distance (OID or R_2)

As can be seen in Figure 1.3, R_2 is the distance from the object to the detector. While $R_2 \approx 0$ is used in the formation of a contact radiograph, a non-zero R_2 is necessary for the formation of a phase contrast radiograph. X-rays exiting the specimen need this distance in order to generate the interference effects between waves of different phase shifts. Additionally, an advantage that a non-zero R_2 can also provide is scatter rejection without the aid of an anti-scatter grid. This may allow for a reduction in dose without any perceivable loss in image quality when compared to a conventional radiograph using an anti-scatter grid since the use of an anti-scatter grid is usually accompanied by a longer exposure time.

I.1.4.6 Geometric Unsharpness

Geometric unsharpness is a blurring of an object in a radiograph due to the finite spatial extent of the x-ray source. As can be seen on the left of Figure 1.9, there is no blurring when the x-ray source is a point source. However, when there is a spatial extent to the x-ray source, blurring occurs at the edges of the object. This blurring is not only a function of the finite x-ray source size but also of R_1 and R_2. The length of the geometric unsharpness, L_g, associated with an object is equal to

$$L_g = f\frac{R_2}{R_1} \tag{1.11}$$

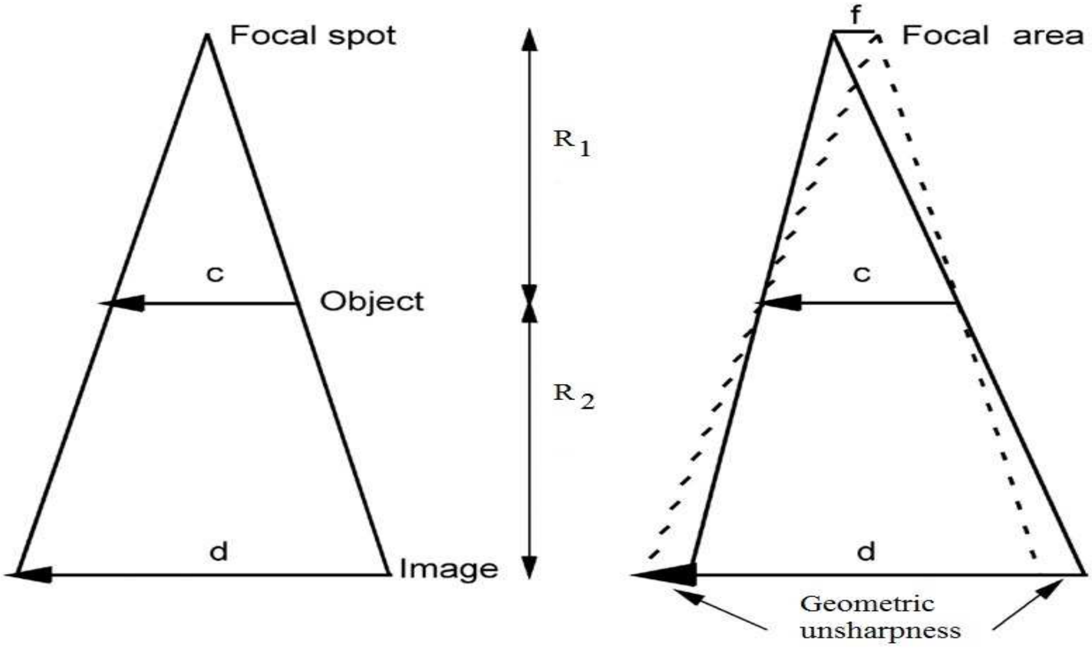

Figure 1.9: Geometric unsharpness due to the finite size of the x-ray source. Adapted from [32].

where f is the focal spot size, R_1 is the source-to-object distance and R_2 is the object-to-image distance. From equation 1.11, a small focal spot size will help to minimize the geometric unsharpness and therefore reduce the blurring seen in the radiograph.

I.1.4.7 Magnification

With a non-zero R_2 necessary for the formation of a phase contrast radiograph, magnification of the specimen will naturally occur. Magnification is given by the equation:

$$M = \frac{d}{c} = \frac{R_1 + R_2}{R_1} = 1 + \frac{R_2}{R_1} \tag{1.12}$$

where all variables are defined in Figure 1.9. While geometric unsharpness will blur the image of an object, it has been reported in the literature that magnification will increase the image sharpness due to a rescaling of the spatial frequency at the detector [29].

I.1.4.8 Phase-Space Shearing Length

It has been argued in the literature that the lateral coherence length is not the sole measure of phase-contrast visibility [30]. In addition to the lateral coherence length, the phase-space shearing length should also be included. This particular length takes into consideration the diffraction of the x-ray as it leaves the specimen and travels toward the detector. The magnitude of phase-space shearing length is given by

$$L_{\text{shear}} = \frac{\lambda R_2 \left|\mathbf{u}\right|}{M} \tag{1.13}$$

where λ is the monochromatic wavelength of the x-ray, R_2 is the object-to-image distance, and $|\mathbf{u}|$ is the spatial frequency of the object's structural component of interest. If a polychromatic source is used, then the monochromatic wavelength may be replaced with the average x-ray wavelength. It was argued that the ratio of the phase-space shearing length to the lateral coherence length is what actually determines the edge enhancement visibility. This ratio is given as

$$\frac{L_{\text{shear}}}{L_{\text{coh}}} = \frac{R_2 f \left|\mathbf{u}\right|}{M R_1} = \frac{(M-1)\, f \left|\mathbf{u}\right|}{M} \tag{1.14}$$

where all variables have been previously defined [30]. Values for this ratio and the physical meaning are given in Table 1.2.

Table 1.2: Ratio of Phase-Space Shearing Length to Lateral Coherence Length

$\frac{L_{\text{shear}}}{L_{\text{coh}}}$	Comments
$<< 1$	The x-ray wave is almost fully coherent over the shearing length. The edge enhancement for the structural component of interest is visible.
< 1	The x-ray wave is partially coherent over the shearing length. The edge enhancement visibility increases with decreasing L_{shear}.
≥ 1	The x-ray wave is not coherent over the shearing length. The edge enhancement is not visible.

I.1.4.9 kVp

Conventional radiography relies upon the absorption of x-rays to produce the contrast seen within radiographic images. This absorption of x-rays leads to radiation dose being deposited in the specimen that may eventually lead to considerable physical or biological damage. This absorption process, known as the photoelectric effect (described in Appendix A), decreases as the x-ray energy increases approximately proportional to E^{-3} where E is the x-ray energy. For phase-contrast imaging, however, the contrast is produced by the transmission and interference of x-rays and not through their absorption. It has also been shown that the x-ray energy dependence of δ is proportional to E^{-2} [23]. This suggest that the use of higher energy x-rays would be possible and could result in a lower radiation dose to the specimen. Research has shown that the phase-contrast edge enhancement is relatively independent of x-ray tube voltages ranging from 30 kVp to 110 kVp [24, 25].

Bibliography

[1] Jerrold T. Bushberg, J. Anthony Seibert, Edwin M. Leidholdt Jr., John M. Boone, *The Essential Physics of Medical Imaging 2nd Edition*, Lippincott Williams and Wilkins (2002)

[2] Shu-Ang Zhou, Anders Brahme, **Development of Phase-Contrast X-ray Imaging Techniques and Potential Medical Applications**, Physica Medica (2008), Vol. **24**, 129-148

[3] S. Matsuo, et al., **Evaluation of Edge Effect Due to Phase Contrast Imaging for Mammography**, Medical Physics, Vol. **32**, No. 8, August 2005.

[4] T.J. Davis, T.E. Gureyev, D. Gao, A.W. Stevenson, S.W. Wilkins, **X-ray Image Contrast from a Simple Phase Object**, Physical Review Letters (1995), Vol. **74**, Number 16, 3173 - 3177

[5] T. Takeda, A. Momose, J. Wu, Q. Yu, T. Zeniya, T.T. Lwin, A. Yoneyama, Y. Itali, **Vessel Imaging By Interferometric Phase-Contrast X-Ray Technique**, Circulation (2002), Vol. **105**, 1708 - 1712

[6] A. Momose, T. Takeda, Y. Itali, **Blood Vessels: Depiction at Phase-Contrast X-Ray Imaging Without Contrast Agents in the Mouse and Rat - Feasibility Study**, Radiology (2000), Vol. **217**, 593 - 596

[7] J. Mollenhauer, M.E. Aurich, Z. Zhong, C. Muehleman, A.A. Cole, M. Hasnah, O. Oltulu, K.E. Kuettner, A. Margulis, L.D. Chapman, **Diffraction-Enhanced X-Ray Imaging of Articular Cartilage**, Osteoarthritis Cartilage (2002), Vol. **10**, 163 - 171

[8] S. Majumdar, A.S. Issever, A. Burghardt, J. Lotz, F. Artelli, L. Rigdon, G. Heitner, R. H. Menk, **Diffraction Enhanced Imaging of Articular Cartilage and Comparison with Micro-Computed Tomography of the Underlying Bone Structure**, European Radiology (2004), Vol. **14**, 1440 - 1448

[9] D.A. Lynch, J.D. Newell, J.S. Lee, *Imaging of Diffuse Lung Disease*, B.C. Decker (2000)

[10] M.J. Kitchen, R.A. Lewis, N. Yagi, K. Uesugi, D. Paganin, S.B. Hooper, G. Adams, S. Jureczek, J. Singh, C.R. Christensen, A.P. Hufton, C.J. Hall, K.C. Cheung, K.M. Pavlov, **Phase Contrast X-ray Imaging of Mice and Rabbit Lungs: A Comparative Study**, British Journal of Radiology (2005), Vol. **78**, 1018 - 1027

[11] R.A. Lewis, N. Yagi, M.J. Kitchen, M.J. Morgan, D. Paganin, K.K.W. Siu, K. Pavlov, I. Williams, K. Uesugi, M.J. Wallace, C.J. Hall, J. Whitley, S.B. Hooper, **Dynamic Imaging of the Lungs Using X-Ray Phase Contrast**, Physics in Medicine and Biology (2005), Vol. **50**, 5031 - 5040

[12] E.A. Sickles, **Breast Imaging: from 1965 to the Present**, Radiology (2000), Vol. **215**, 1 - 16

[13] J. Keyrilainen, M. Fernandez, S. Fiedler, A. Bravin, M.L. Karjalainen-Lindsberg, P. Virkkunen, E.M. Elo, M. Tenhunen, P. Suortti, W. Thomlinson, **Visualisation of Calcifications and Thin Collagen Strands in Human Breast Tumour Specimens by the Diffraction-Enhanced Imaging technique: A Comparison with Conventional Mammography and Histology**, European Journal of Radiology (2005), Vol. **53**, 226 - 237

[14] F. Arfelli, V. Bonvicini, A. Bravin, G. Cantatore, E. Castelli, L.D. Palma, M. DiMichiel, M. Fabrizioli, R. Longo, R.H. Menk, A. Olivo, S. Pani, D. Pontoni, P. Poropat, M. Prest, A. Rashevsky, M. Ratti, L. Rigon, G. Tromba, A. Vacchi, E. Vallazza, F. Zanconati, **Mammography with Synchrotron Radiation: Phase-Detection Techniques**, Radiology (2000), Vol. **215**, 286 - 293

[15] E.D. Pisano, R.E. Johnston, D. Chapman, J. Geradts, M.V. Iacocca, C.A. Livasy, D.B. Washburn, D.E. Sayers, Z. Zhong, M.Z. Kiss, W.C. Thomlinson, **Human Breast Cancer Specimens: Diffraction-Enhanced Imaging with Histologic Correlation - Improved Conspicuity of Lesion Detail Compared with Digital Radiography**, Radiology (2000), Vol. **214**, 895 - 901

[16] M.Z. Kiss, D.E. Sayers, Z. Zhong, C. Pharham, E.D. Pisano, **Improved Image Contrast of Calcifications in Breast Tissue Specimens Using Diffraction Enhanced Imaging**, Physics in Medicine and Biology (2004), Vol. **49**, 3427 - 3439

[17] C. Liu, X. Yan, X. Zhang, W. Yang, W. Peng, D. Shi, P. Zhu, W. Huang, Q. Yuan, **Evaluation of X-Ray Diffraction Enhanced Imaging in the Diagnosis of Breast Cancer**, Physics in Medicine and Biology (2007), Vol. **52**, 419 - 427

[18] V.N. Ingal, E.A. Beliaevskayay, A.P. Brianskayaz, R.D. Merkurievax, **Phase Mammography - A New Technique for Breast Investigation**, Physics in Medicine and Biology (1998), Vol. **49**, 3427 - 3439

[19] R.W. James, *The Optical Principles of the Diffraction of X-Rays*, Ox Bow Press (1964)

[20] David Attwood, *Soft X-rays and Extreme Ultraviolet Radiation*, Cambridge University Press (1999)

[21] B.L. Henke, E.M. Gullikson, and J.C. Davis, **X-ray Interactions: Photoabsorption, Scattering, Transmission, and Reflection at E = 50-30,000 eV, Z = 1-92**, Atomic Data and Nuclear Data Tables 54, 181-342, (1993)

[22] Edwin F. Donnelly, **Development and Evaluation of a Polychromatic Phase-Contrast Radiography Imaging System** , Ph.D Thesis, Vanderbilt University, 2003

[23] T.J. Davis, D. Gao, T.E. Gureyev, A.W. Stevenson, and S.W. Wilkins, **Phase-Contrast Imaging of Weakly Absorbing Materials Using Hard X-Rays**, Nature (1995), Vol. **373**, 595 - 598

[24] E.F. Donnelly, R.R. Price, and D.R. Pickens, **Quantification of the Effect of System and Object Parameters on Edge Enhancement in Phase-Contrast Radiogaphy**, Medical Physics (2003), Vol. **30**, 1 - 9

[25] E.F. Donnelly, and R.R. Price, **Quantification of the Effect of kVp on Edge-Enhancement Index in Phase-Contrast Radiography**, Medical Physics (2002), Vol. **29**, 999 - 1002

[26] S.T. Thornton and A. Rex, *Modern Physics for Scientists and Engineers 4th Edition*, Brooks/Cole, 2012

[27] S.W. Wilkins, T.E. Gureyev, D. Gao, A. Pogany, and A.W. Anderson, **Phase-Contrast Imaging Using Polychromatic Hard X-rays**, Nature (1996), Vol. **384**, 335 - 338

[28] David M. Paganin, *Coherent X-ray Optics*, Oxford Press University (2006)

[29] C.C. Shaw, X. Liu, M. Lemacks, J.X. Rong, G.J. Whitman, **Optimization of MTF and DQE in Magnification Radiography - A Theoretical Analysis**, Medical Imaging 2000:Physics of Medical Imaging, Proceedings of SPIE Vol. **3977** (2000), 467 - 476

[30] X. Wu, H. Liu, **Clarification of Aspects in In-Line Phase-Sensitive X-ray Imaging**, Medical Physics (2007), Vol. **2**, 737 - 743

[31] R. Nave, Inverse Square Law General, Hyperphysics, Web, Georgia State University, $\langle http://hyperphysics.phy-astr.gsu.edu/hbase/forces/isq.html\rangle$

[32] N. Oldnall, Geometric Unsharpness, e-radiography.net, Web, Nick Oldnall, $\langle http://www.e-radiography.net/radtech/u/unsharpness.htm\rangle$

Chapter II

Production of Phase-Contrast Planar and Tomographic Images

II.1 Planar Phase-Sensitive Image Production

In general, as the incident x-ray traverses an object, not only does the x-ray experience attenuation but the phase of the x-ray experiences a shift. An x-ray image may contain this phase shift, ϕ, in one of three different forms: as the direct measure of ϕ, as the gradient of ϕ, or as the Laplacian of ϕ. These three phase shift variations respectively correspond to the following three methods of planar x-ray image production: interferometric, diffractometric or gratings-based, and free-space propagation [1].

II.1.1 Phase Imaging

II.1.1.1 X-ray Interferometric Method

The early development of x-ray phase-contrast imaging was based on the use of x-ray interferometry. This technique was pioneered by Bonse and Hart in 1965 and has been refined by Momose, Takeda, and Sutter [2–5]. X-ray interferometry is the most sensitive method for detecting minute changes in the refractive index. These minute changes in the refractive index correspond to minute physical density variations in the sample and thus the images obtained can be interpreted quantitatively as electron density maps.

The typical configuration for an x-ray interferometer is given in Figure 2.1 and is sometimes known as the triple Laue-type (LLL) x-ray interferometer. This configuration corresponds to that of the Mach-Zehnder interferometer.

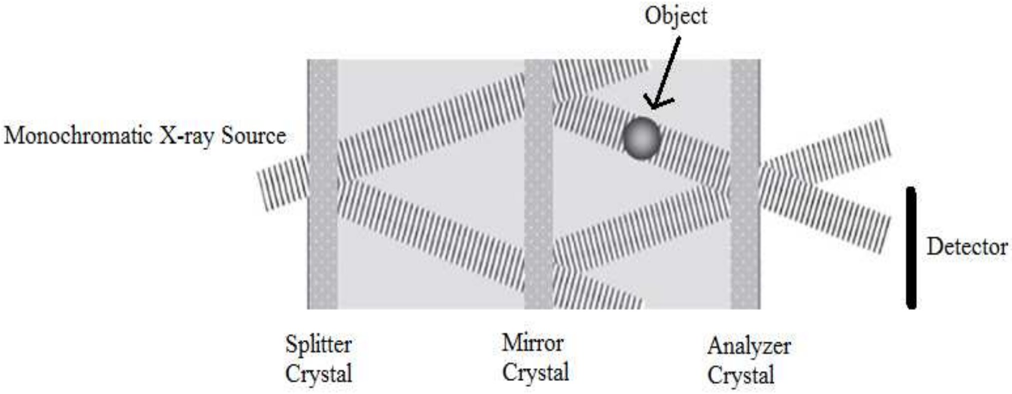

Figure 2.1: An x-ray interferometer with three perfect crystals. Adapted from [5]

Through Laue diffraction (which is equivalent to Bragg diffraction and is a transmission phenomenon rather than a reflection phenomenon), the first crystal acts as a phase-coherent beam splitter for the incident monochromatic x-ray beam. The two emergent coherent x-ray beams are spatially separated before their arrival at the second crystal called the mirror. Again under the Laue condition, four coherent x-ray beams are generated from the two incident coherent x-ray beams. Two of the four generated x-ray beams will overlap at the third crystal called the analyzer. An object placed in one of the convergent x-ray beams will cause phase shifts in that x-ray beam and distort its wavefront. The undistorted reference beam interferes with the distorted x-ray beam and an interference pattern corresponding to the phase shift due to the object is observed at the detector placed behind the analyzer crystal. The recorded interference patterns can not be used immediately because the interference fringes can not be directly linked to a projection of the object and an intrinsic fringe pattern (due to the interferometer or the sample environment) is always present. A phase-mapping image is obtained by adding a set of interference patterns recorded at different phase shift positions between the distorted and undistorted x-ray beams. Using this, the attenuation contrast effects are removed and the intrinsic phase patterns are compensated [6, 7]. This method works best for small or smooth phase gradients since the interference fringe spacing is inversely proportional to the x-ray beam deflection. When the phase varies sharply, the fringe spacings become too fine and are thus unresolvable.

X-ray interferometry is sensitive to density variations on the order of $10^{-3}\ \frac{\mathrm{g}}{\mathrm{cm}^3}$ [6]. This sensitivity demands strict requirements on the alignment and stability of the crystals used, generally on the order of 10^{-2} nm [1]. To achieve such requirements, the x-ray interferometer is usually cut from a perfect, single crystal monolithic block of silicon. This provides the necessary alignment and stability requirements mentioned above. However, the maximum size of such a monolithic crystalline block limits the potential field of view to approximately 3 cm x 3 cm. This field of view is smaller than that used in clinical applications such as mammography (18 cm x 23 cm to 24 cm x 29 cm). Recently, there has been a new x-ray interferometric configuration called the skew-symmetric two-crystal x-ray interferometer that is capable of doubling the field of view of the monolithic x-ray interferometers [8]. This capability of doubling the field of view comes at the expense of an increase in the mechanical rigidity and stability of the skew-symmetric two-crystal x-ray interferometer.

II.1.2 Phase Gradient Imaging

II.1.2.1 Diffraction Enhanced Imaging Method

Diffraction enhanced imaging (DEI) is an x-ray imaging technique that provides images in which the contrast is proportional to the gradient of the phase, $\nabla\phi\,(x, y)$, and to that of the projected electron density, $\nabla\rho_e\,(x, y)$. The technique of imaging the refractive index gradient was first used by Forster and colleagues and was referred to as the Schlieren method [6]. Slightly different variations of the Schlieren method have been used and the utilization of Bragg diffraction from a crystal analyzer as a very sensitive angular filter is the method now known as DEI. Compared with the attenuation contrast found in conventional radiography, DEI enhances the image quality by one or more combinations of different contrast mechanisms such as attenuation, scatter rejection (sometimes referred to as extinction) and refraction.

An example of an experimental DEI setup is shown in the following figure.

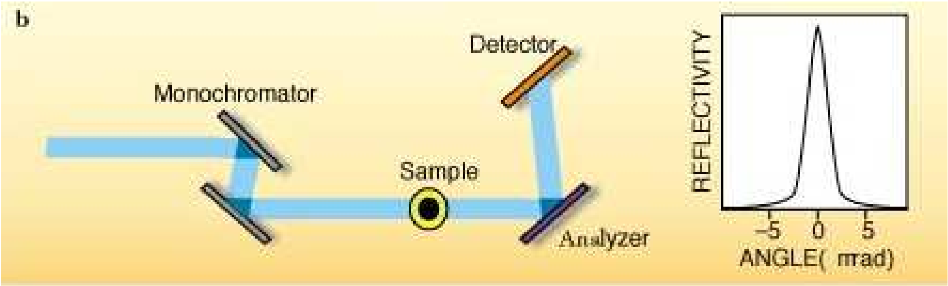

Figure 2.2: (*Left*): Experimantal Setup for DEI. (*Right*): A Rocking Curve. Adapted from [1]

A crystal monochromator is first used to select a narrow band of x-ray energy before traversing the object. As the x-ray beam traverses the object, the beam can be absorbed, scattered coherently or incoherently, or refracted through very small angles due to the variations in the refractive index. After traversing the object, the x-ray beam is analyzed with a tunable perfect crystal. The beam will satisfy this crystal's Bragg condition for reflection (Equation (1.9)) only for a narrow range of incident angles, typically on the order of a few microradians. X-rays that have been scattered outside this narrow range will not be reflected; however, those within this narrow range will be reflected and contribute to the image formation on a detector. The plot of the amount of reflectivity obtained versus the narrow range of acceptable incident angles is called the crystal's rocking curve (see Figure 2.2).

When the analyzer is aligned to reflect the peak of the rocking curve, it will filter out any x-rays that are scattered or refracted by more than a few microradians. The resulting image will resemble an x-ray absorption radiograph except it will have enhanced contrast due to scatter rejection. If the analyzer is tuned to either of the rocking curve tails, it becomes possible to reject the unrefracted x-rays and select the scattered x-rays for image formation. If the image was obtained from an untuned analyzer, then it will include both absorption and refraction effects. By combining images obtained on either side of the rocking curve, these effects can be separated and used to produce images of pure refraction and images of scatter rejection since they rely on different contrast mechanisms.

An intense monochromatic x-ray beam is essential for acquiring a diffraction enhanced image within a reasonable exposure time. This is the main challenge in developing DEI as a viable medical imaging modality since the only radiation source capable of supplying such an x-ray beam is from a synchrotron. These are unsuitable for widespread clinical use due to their limited availability, large dimensions, maintenance and high operating costs [6]. Although research has been done involving tissue specimens and laboratory animals using a monochromatized radiation from an x-ray tube, the low intensities involved would require unacceptably long exposure times [9, 10].

An alternative method of measuring the contrast generated by $\nabla\phi$ is through the use of a Talbot interferometer. Talbot interferometry is based upon the Talbot effect which is a self-imaging phenomenon by a periodic object, such as a transmission grating, under spatially coherent illumination [11]. The self-imaging phenomenon is understood as a result of Fresnel diffraction or multi-beam interference between diffraction orders caused by the periodic object [12]. This interference generates fringes that corresponds to contours of constant differential phase. The experimental set-up is shown in Figure 2.3.

In this set-up, the first grating (G_0) is placed after an incoherent x-ray source. This grating

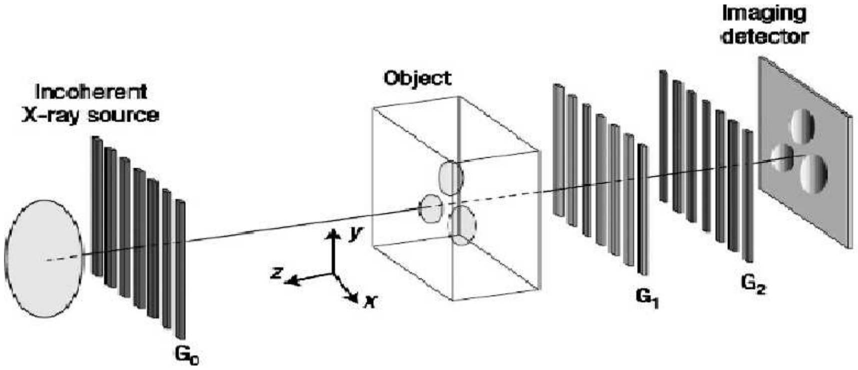

Figure 2.3: X-ray Talbot Interferometer Experimental Set-up. Adapted from Reference [13]

creates an array of individually coherent (yet mutually incoherent) sources. The beam then travels through the object where the phase shift is introduced. Beyond the object, the beam encounters the second grating (G_1). This grating (whose lines show negligible absorption but substantial phase shift) is a phase mask that imparts a periodic phase modulation onto the transmitted x-ray wave. This phase modulation is transformed into an intensity modulation on the plane of the third grating (G_2). This third grating (with absorbing lines) is an absorption mask and is placed immediately in front of the detector at a position on the optical axis so that the self-image of G_1 is formed on G_2. The grating G_1 or G_2 is scanned along a direction transverse to the x-ray wave propagation over the period of the grating and an image is taken. The phases of the intensity oscillations in each pixel are proportional to $\nabla\phi$ [14–17]. While this method needs neither a synchrotron source nor crystal optics, it still has drawbacks in the form of possible inefficient dose delivery due to the two gratings downstream of the sample and the fabrication of better absorption grating (G_2) due to the high penetration power of hard x-rays [5].

II.1.3 Phase Laplacian Imaging

II.1.3.1 Free Space Propagation Method

In this imaging method (used throughout the rest of this dissertation), the resultant image is dependent upon the observation of an interference pattern between diffracted and non-diffracted waves. When $|\nabla\phi|$ and $\left|\nabla^2\phi\right|$ are large, the resulting interference patterns are strong. As a spatially coherent x-ray wave travels through a sample, the x-ray wave experiences a phase-shift. When this phase-shifted, or refracted, x-ray wave interferes with the unrefracted x-ray wave, an observable intensity change occurs depending upon the object-to-detector distance (ODD) (see Figure 2.4).

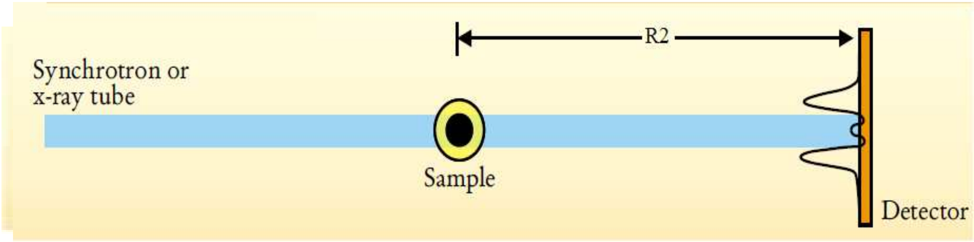

Figure 2.4: Experimental Set-Up for Free Space Propagation (note: $R2$ is the ODD). Adapted from [1]

This distance maybe divided into four regions of space (as seen in Figure 2.5).

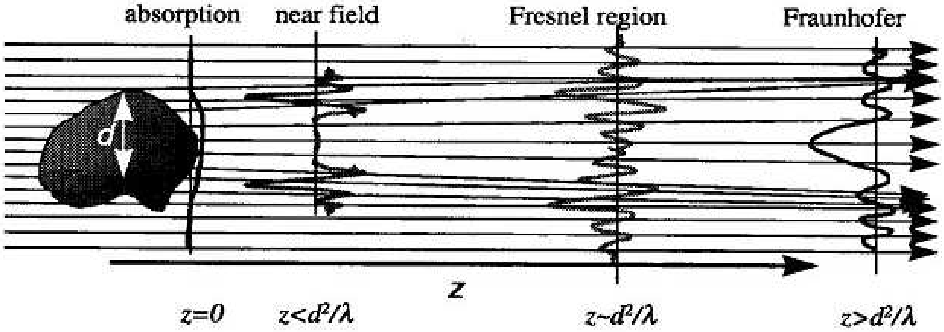

Figure 2.5: Object-to-Detector Distances. Adapted from [18]

In Figure 2.5, z is the ODD, λ is the x-ray wavelength, and d is the object size. When $z = 0$, the resultant image is pure attenuation due to the lack of propagation distance for the refracted x-ray beam. When $z < \frac{d^2}{\lambda}$, the resultant image contains observable light-dark fringes occurring at the interfaces between the structures within the sample. When $z \approx \frac{d^2}{\lambda}$, the resultant image contains more and wider fringes with increasing object-to-detector distance. Finally, when $z > \frac{d^2}{\lambda}$, the resultant image contains ringing artifacts due to even larger interference fringes and thus degrades the image quality. The image contrast between the $z < \frac{d^2}{\lambda}$ region and the $z \approx \frac{d^2}{\lambda}$ region is proportional to the Laplacian of the phase or $\nabla^2\phi$. This is also proportional to the Laplacian of the projected electron density, $\nabla^2\rho_e$. Thus this region is particularly suitable for increasing the conspicuity of edges or boundaries since the Laplacian becomes very significant. The attenuation contrast is still present (except for a pure phase object) such that the two types of imaging methods are complementary thereby providing further information on the sample in comparison to only an attenuation image [6].

The simple design of the free space propagation method is an advantage since it does not rely on crystal optics or gratings and it already resembles clinical radiography systems. Furthermore, this imaging method does not need to use a synchrotron as the x-ray source. Instead, it may use a conventional micro-focus x-ray tube because the focal spot size is small enough to provide the necessary spatial (or lateral) coherence to the incoming x-ray wave. Polychromatic x-rays may be used because the geometric features of the image contrast are wave-length independent. An additional benefit of the wave-length independence is that the x-ray source may be operated at a higher energy leading to a potential reduction of dose deposited to the sample. However, the simplicity of the design also contains some drawbacks including the finding of the appropriate source-to-object and object-to-detector distances to avoid the consequences of the inverse square law and provide enough spatial coherence to the incoming x-ray wave. In using the conventional x-ray source, the focal spot size should be on the order of microns.

Table 2.1: Summary of the X-ray Planar Phase-Contrast Imaging Modalities

Method	Phase shift	Advantages	Disadvantages
Interferometric	ϕ	Most sensitive method for measuring ϕ. Excellent for smooth ϕ changes.	Strict mechanical and thermal stability requirements. Unable to resolve sharp ϕ changes. Limited field of view.
Diffractometric	$\nabla\phi$	Measures phase gradients. Images may contain one or a combination of phase, absorption and scatter information.	Requires synchrotron source for reasonable exposure times. Alignment of crystal optics.
Talbot Interferometric	$\nabla\phi$	Measures phase gradients. Uses mono- or polychromatic source. No crystal optics needed.	Specialized grating fabrications. Brilliant x-ray source required.
Free Space Propagation	$\nabla^2\phi$	Measures phase Laplacian. Enhances boundaries. Simpler experimental design. Proportional to the electron density Laplacian.	Correct geometrical settings. Small focal spot size for conventional x-ray sources. Low output flux for conventional x-ray sources.

II.2 Three Dimensional Tomography

Regardless of the production method, any internally complex object's planar phase-contrast radiograph will show a superposition of regions and boundaries. To overcome this visual impedance, one may resort to the tomographic reconstruction methods of computed tomography or digital tomosynthesis. These methods require multiple planar phase-contrast radiographs from different angular views of the object and are computationally reconstructed to produce a volumetric image.

II.2.1 Computed Tomography

Computed tomography (CT) was the first of the modern slice-imaging modalities using ionizing radiation to non-invasively acquire axial images of the inside of an internally complex object that were not biased by the superposition of the object's internal structures. The fundamental problem of computed tomography deals with how to reconstruct an object from its x-ray projections. These x-rays, as they pass through an object, are attenuated and the amount of attenuation depends upon the orientation of the object's internal structures relative to the x-ray beam. Thus, one projection is not adequate for the object's reconstruction. For a proper determination of the structure, it becomes necessary to irradiate the object from various angles (see Figure 2.6).

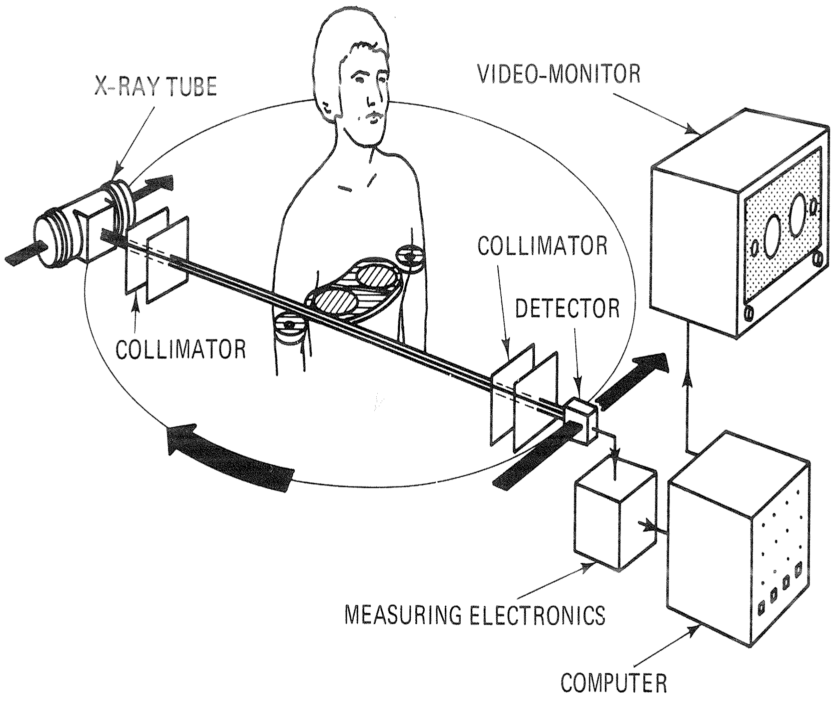

Figure 2.6: CT Image Acquisition. Adapted from [27]

As can be seen in Figure 2.7, there have been basically four distinct generations of computed tomography that have emerged [20]:

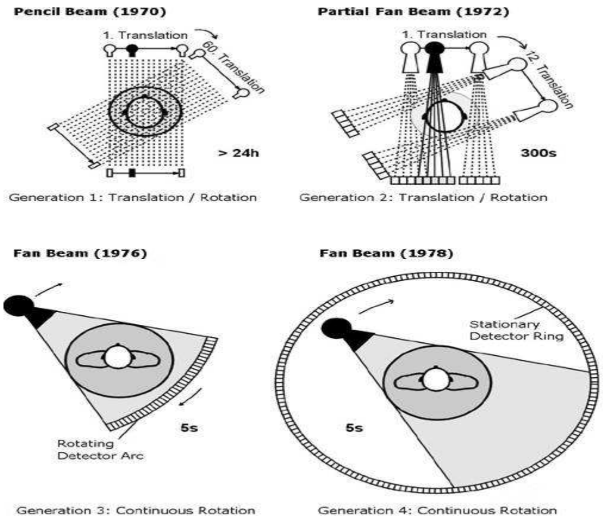

Figure 2.7: The Four Different CT Generations with Approximate Acquisitions Times Noted. Adapted from [28]

- **Pencil Beam Rotation-Translation** The first generation of CT consisted of a highly collimated x-ray beam called an x-ray pencil beam. This x-ray pencil beam was then passed through an object where a single detector would register the transmitted x-ray beam. In synchrony, the x-ray pencil beam and the detector would move linearly across the object until a one-dimensional radiograph was obtained. The x-ray pencil beam and detector would be rotated through some angle and the process would be repeated until a rotation of 180 ° had been achieved.

- **Fan Beam Rotation-Translation** The second generation of CT is similar to the first generation CT except that, instead of an x-ray pencil beam, an x-ray fan beam was used. This also necessitated the replacement of the single detector with a detector array that allowed for shorter acquisition times per radiograph.

- **Fan Beam Rotation, Wide Aperture Fan Beam** The third generation of CT was an extension of the second generation's concept of an x-ray fan beam. The third generation CT substantially increased the x-ray fan beam angle and lengthened the detector array. This has allowed for the potential to simultaneously x-ray the entire field-of-view for every angle. As a result, a complete abandonment of the need for the linear displacement of the detector array had been achieved and it also led to a greater reduction of acquisition times when compared to the second generation CT. The majority of CT scanners currently in clinical use are third generation.

- **Fan Beam Rotation, Fixed Closed Ring Detector** The major difference between the fourth and third generation CT systems lie in the closed, stationary detector ring that is used in the fourth generation. The x-ray fan beam either rotates outside or inside the detector ring. As a result of this configuration, fourth generation CT systems established inverse fan beams that are centered on the detectors rather than on the x-ray source.

Therefore, the reconstruction of the internal structure of the object comes from using multiple x-ray projections. Though the mathematical framework for CT imaging was derived in the early 20th century by the mathematician Radon, it was not until the development of modern computer technology in the later half of the 20th century that allowed for its viability [19]. There are basically three different methods of image reconstruction [29]:

- **Analytical Reconstruction**: Analytical reconstruction methods treat the object as a continuous function, $f(x,y)$, as well as its measured projection data, $g(\theta, L)$. This allows for the reconstruction to be set-up as an integral equation where an exact or approximate solution can be obtained. Some common analytical methods include [35]
    - Backprojection: The backprojection is a simple approach to reconstruction. The reconstructed image starts off as an empty matrix and then, after pre-processing of the projection data, the backprojection is formed by smearing each view back through the image in the direction corresponding to the x-ray path. This is illustrated in Figure 2.8.

      Although simple to comprehend, the backprojection method results in a blurry image of the object being scanned.
    - Fourier: This reconstruction method takes advantage of the Fourier or Projection-Slice Theorem. This theorem states that the one dimensional Fourier transform of an object's projection is a slice of the two dimensional Fourier transform of the object (as illustrated in Figure 2.9).

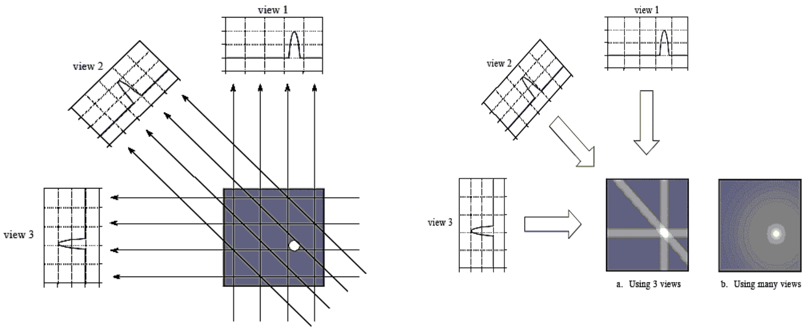

Figure 2.8: (Left) Three views from a CT acquisition of a small circular object. (Right) Backprojection image formation. Adapted from [33]

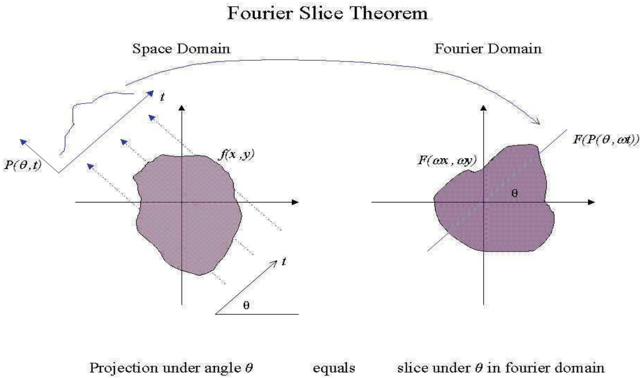

Figure 2.9: Fourier Slice Theorem. Adapted from [34]

The Fourier method takes the one dimensional Fourier transform of each projection and then inserts it into the two dimensional Fourier plane with the corresponding angle. Then the inverse Fourier transform is performed to produce the reconstructed image. The Fourier method is not widely used in CT due to the problem of interpolating the polar data onto a Cartesian grid.

- Filtered backprojection: This reconstruction method corrects the blurring encountered in the backprojection method by filtering each view before it is backprojected. This filtering is done by convolving the projection data with a convolution kernel to create a filtered view. These filtered views are then backprojected to provide a reconstructed image that accurately reflects the object being scanned. This method is usually the preferred method on CT scanners.

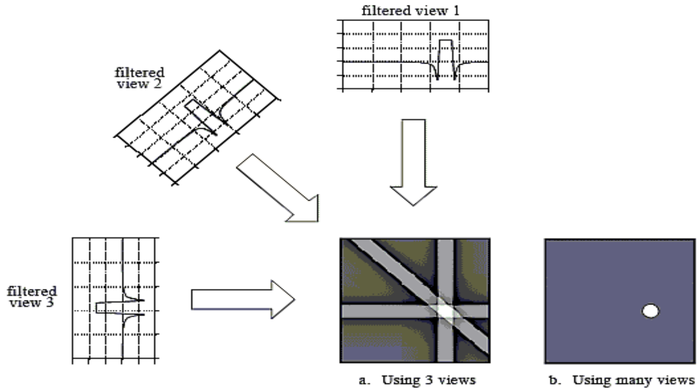

Figure 2.10: Filter Backprojection of the object in Figure 2.8. Adapted from [33].

The advantage of the analytical reconstruction methods is that the algorithms used are robust in their convergence in the presence of noise and the computational times are reduced when compared to the other methods.

- **Algebraic Reconstruction**: Algebraic reconstruction methods treat the object as a discrete instead of a continuous function. For this method, the measured projection data will be expressed as a summation of the object's voxel values that lie along a given ray. This method produces a matrix equation

$$\mathbf{g} = \mathbf{M} \cdot \mathbf{f} \tag{2.1}$$

  where **g** represents the measured data, **f** represents the unknown object and **M** represents the weighting values experienced by the object's voxels. The algebraic reconstruction method attempts to solve for **f** through either a straightforward (though time consuming and error-prone) matrix inversion or through an iterative process.

- **Statistical Reconstruction**: Statistical reconstruction methods model the measured projection data statistically. This is accomplished by iteratively applying the maximum likelihood method which is a statistical estimation method where the image obtained is one that matches the measured projection values best, taking into account the measurement statistics of the x-ray photons. This method is typically used in situations where the number of x-ray quanta on the detectors is quite small and noise can dominate the reconstructed image such as in PET and SPECT imaging. The goal of the maximum likelihood (ML) method is to find the expectation value μ that optimizes the Poisson log-likelihood function, $L(\mu)$. Various algorithms have proposed to optimize $L(\mu)$ such as ML-expectation maximization [21], ML-convex [22, 23] or ML-paraboloidal with a conjugate gradient Polak-Ribiere search strategy [24]. It is also possible to define some prior probability function that penalizes the $L(\mu)$ and suppresses the noise. Those penalty functions yield maximum-a-posteriori (MAP) algorithms [25]. Two such penalty functions that are commonly used are the hyperbolic potential and the anisotropic total variation (TV) norm [26]. Although most clinical CT scanners use analytical methods for image reconstruction, iterative reconstruction techniques have demonstrated the benefit of potential dose reduction and it is believed that there will be a gradual shift toward iterative image reconstruction in the future [20, 30].

II.2.2 Digital Tomosynthesis

Before the advent of CT, tomographic imaging was performed using analog geometric tomography. In analog geometric tomography, the x-ray source and screen-film move in synchrony on opposite sides of the object. The motion of the x-ray source and screen-film may be linear, circular, elliptical, figure 8 pattern, trispiral or even hypocycloidal, see Figure 2.11 [32].

The placement of the x-ray source and screen-film with respect to the object will define a fulcrum plane or slice about which this motion will occur. The resultant longitudinal radiographic image will contain points that are in focus within this fulcrum plane and those points that lie outside of the fulcrum plane or slice are blurred, more so at greater distances. This blurred information that is above and below the fulcrum plane does not disappear but is superimposed on the focused image of the fulcrum plane. This tomographic blur obscures detail in the fulcrum plane and limits the contrast enhancement in the focused image. While analog geometric tomography allows for depth localization and improved conspicuity by removing overlying structures, it is also limited by the fact that only one fulcrum plane can be acquired at a time. This limitation could lead to an excessive patient dose and exposure time during the acquisition of enough radiographic data to produce a volumetric image [31].

Digital tomosynthesis improves upon analog geometric tomography in that it allows for any

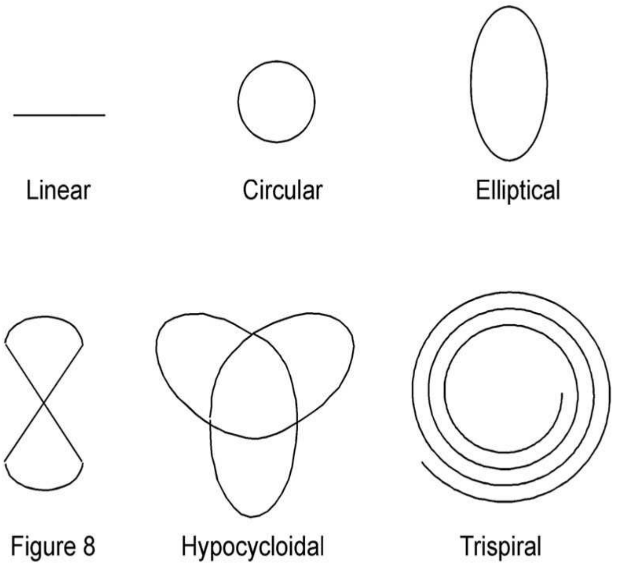

Figure 2.11: The possible motions available in a tomography system. Adapted from [32].

number of fulcrum planes or slices to be generated from a finite set of projection radiographs acquired from a single motion of the x-ray source and detector. The reason for this improvement lies in the technological advancements in both detector design and computer processing power. The switch from screen-film to digital flat-panel detectors that were capable of producing high quality images at rapid read-out represented a significant step toward the implementation of tomosynthesis. The increase in computer processing power allows for the retrospective reconstruction and digital post-processing for any number of planes [20, 31].

The conventional reconstruction algorithm used in digital tomosynthesis is the shift-and-add algorithm (SAA). This algorithm creates a set of slice images from the summation of a set of shifted projection images acquired at different orientations of the x-ray tube. Objects within the sample that are at different heights above the detector will be projected at different positions on the detector as the x-ray tube moves. It then becomes possible to shift and add images such that certain structures in a plane are all lined up and are thus in focus and those structures in other planes are distributed over the image and are blurred.

As seen on the left in Figure 2.12, a sample with two embedded objects labeled A and B is imaged at three different x-ray tube locations. The right shows how either object may be brought into focus by shifting and adding the appropriate projection images. Notice how the structures outside the fulcrum plane are spread or blurred across the resultant image.

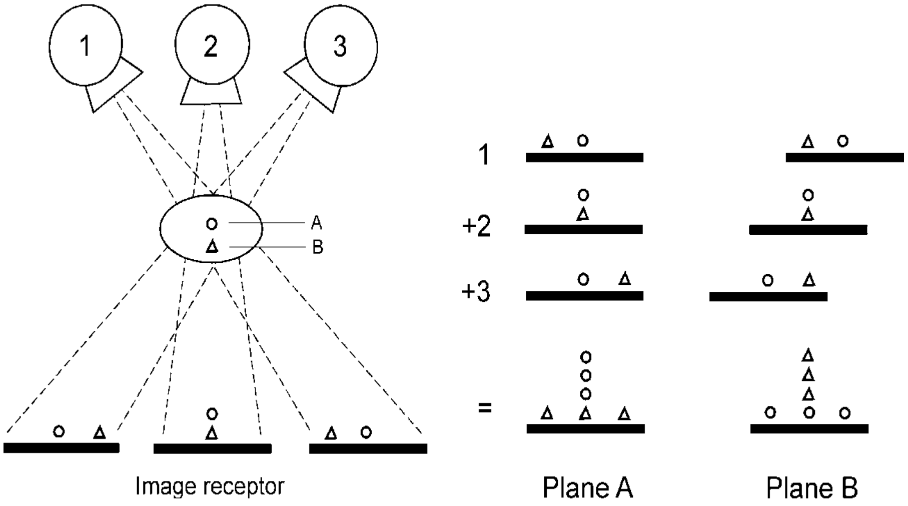

Figure 2.12: (Left) Three Projection Image Acquisition. (Right) Shift-and-Add Reconstruction. Adapted from [31]

Most tomosynthesis systems have the x-ray tube and detector moving anti-parallel to each other. This motion guarantees that magnification in the focal plane remains constant in all projection images. However, there are certain acquisition geometries where this parallel motion is not maintained such as that of a C-arm device. For this case, the motion of the x-ray tube and detector rotate around the isocenter of the system. This type of motion is called an isocentric motion and shall be used throughout the rest of this dissertation (see Figure 2.13).

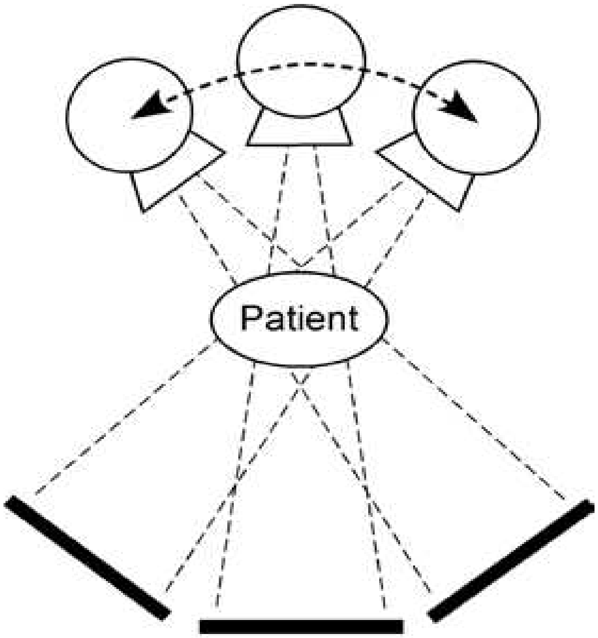

Figure 2.13: Isocentric Motion. Adapted from [31]

Isocentric motion poses two problems [31]:

- The image receptor is not traveling parallel to any plane within the object.
- The angle of the x-ray tube's focal spot varies with respect to the plane being imaged.

These difficulties have been overcome by the development of the multiple projection algorithm [36]. Figure 2.14 shows the experimental set-up used in the description of the multiple projection algorithm.

The point of rotation is located at the isocenter C and the tilt angle is labeled as α. This configuration has projected line CA onto the image receptor forming image C_iA_i. The problem is to convert the projected data of C_iA_i onto a horizontal surface parallel to the plane containing CA. This projected horizontal surface contains the line segment C_hA_h and to perform this procedure is the transformation equation

$$h = \frac{id}{d\cos\alpha - i\sin\alpha} \tag{2.2}$$

where h represents the distance from the origin in the horizontal projection plane C_h, d is the source-to-image (SID) distance, and i represents the distance from the origin in the image receptor

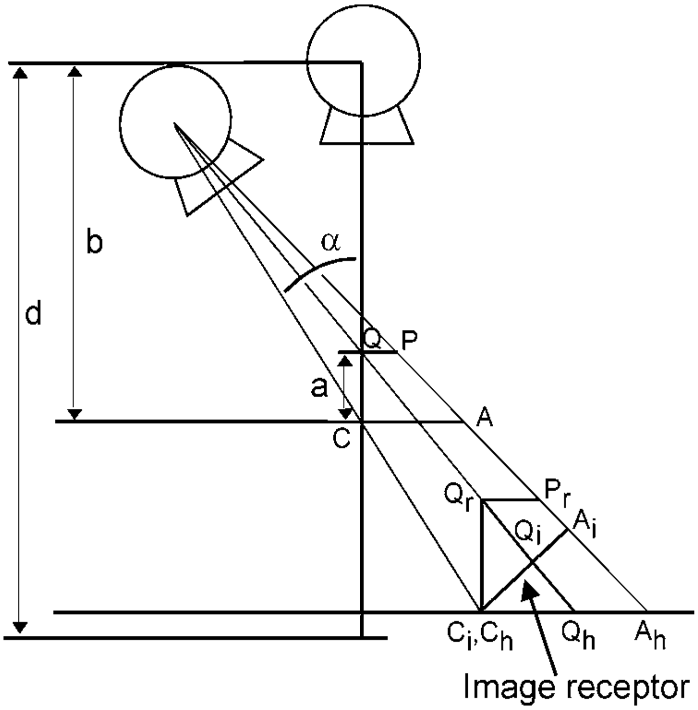

Figure 2.14: Multiple Projection Algorithm. Adapted from [31].

plane C_i with the origin defined as the projected locations of the isocenter C. This transformation represents a stretching of the image data. For any angle α, it can be shown that the projected line segment $C_h A_h$ is constant and that there is no distortion of the projected line CA as a function of angle. Thus, a series of transformed projection images may be added together to form a focused plane of structures that contains the isocenter.

Should a focus plane not contain the isocenter, then a slightly different transformation is required. In Figure 2.14, line segment QP in the plane at a distance a above the isocenter is to be the focus plane. The steps to forming this focus plane is to

1. perform the h transformation as above,
2. shift the horizontal projection image by an amount equal to the line segment length $C_h Q_h$,
3. adjust the scale of the projected and shifted data to account for the differences in magnification as the system rotates.

These last two steps can be summarized together as a single equation:

$$r = \left(h - \frac{ad\sin\alpha}{b\cos\alpha - a}\right)\left(1 - \frac{a}{b\cos\alpha}\right) \tag{2.3}$$

where r is the location in a fictitious plane containing $Q_r P_r$ of an object projected at location h in the horizontal plane. As in the case of a plane containing the isocenter, the fictitious plane that contains $Q_r P_r$ has the property that $Q_r P_r$ does not change its length as a function of α. Thus a series of transformed projection images may be added to give a focus plane containing QP in the object [31].

Bibliography

[1] R. Fitzgerald, **Phase-Sensitive X-Ray Imaging**, Physics Today (2000), July, 23-26

[2] U. Bonse and M. Hart, **An X-ray Interferometer**, Applied Physics Letters (1965), Vol. **6**, 155-156

[3] Atsushi Momose, **Demonstration of Phase-Contrast Computed Tomography Using an X-ray Interferometer**, Nuclear Instrumentation and Methods (1995), Vol. **A352**, 622-628

[4] Tohoru Takeda, Atsushi Momose, J. Wu, Q. Yu, T. Zeniya, T.T. Lwin, A. Yoneyama, Y. Itali, **Vessel Imaging By Interferometric Phase-Contrast X-Ray Technique**, Circulation (2002), Vol. **105**, 1708 - 1712

[5] Shu-Ang Zhou, Anders Brahme, **Development of Phase-Contrast X-ray Imaging Techniques and Potential Medical Applications**, Physica Medica (2008), Vol. **24**, 129 - 148

[6] Jani Keyrilainen, **Diffraction-Enhanced X-ray Imaging of *In Vitro* Breast Tumors**, Ph.D Thesis, University of Helsinki, 2004

[7] Peter Cloetens, **Contribution to Phase Contrast Imaging, Reconstruction and Tomography with Hard Synchrotron Radiation: Principles, Implementation and Applications**, Ph.D Thesis, Vrije Universiteit Brussel, 1999

[8] Akio Yoneyama, Nobuaki Amino, Masamichi mori, Masafumi Kudoh, Tohoru Takeda, Kazuyuki Hyodo, and Yasuharu Hirai, **Non-invasive and Time-resolved Observation of Tumors Implanted in Living Mice by Using Phase-Contrast X-ray Computed Tomography**, Japanese Journal of Applied Physics (2006), Vol. **45**, No. 3A, 1864 - 1868

[9] Viktor N. Ingal, Elena A. Beliaevskaya, Alla P. Brianskaya and Raisa D. Merkurieva, **Phase Mammography - A New Technique for Breast Imvestigation**, Physics in Medicine and Biology (1998), Vol. **43**, 2555 - 2567

[10] Etta D. Pisano, R. Eugene Johnston, Dean Chapman, Joseph Geradts, Mary V. Iacocca, Chad A. Livasy, David B. Washburn, Dale E. Sayers, Zhong Zhong, Miklos Z. Kiss, William C. Thomlinson **Human Breast Cancer Specimens: Diffraction-enhanced Imaging with Histologic Correlation-Improved Conspicuity of Lesion Detail Compared with Digital Radiography**, Radiology (2000), Vol. **214**, 895 - 901

[11] Atushi Momose, Shinya Kawamoto, Ichiro Koyama, Yoshitaka Hamaishi, Kengo Takai, Yoshio Suzuki, **Demonstration of X-ray Talbot Interferometry**, Japanese Journal of Applied Physics (2003), Vol. **42**, L866 - L868

[12] Atushi Momose, Wataru Yashiro, Yoshihiro Takeda, Yoshio Suzuki, Tadashi Hattori, **Phase Imaging with an X-ray Talbot Interferometer**, JCPDS-International Centre for Diffraction Data (2006), 21 - 30

[13] G. Wang, H. Yu, B. De Man, **An Outlook On X-Ray CT Research and Development**, Medical Physics (2008), Vol. **35**, Number 3, 1051 - 1064

[14] F. Pfeiffer, M. Bech, O. Bunk, P. Kraft, E. Eikenberry, C. Bronnimamm, C. Grunzweig, C. David, **Hard X-ray Dark-Field Imaging Using a Grating Interferometer**, Nature (2008), Vol. **7**, 134 - 137

[15] B. Schwarzschild, **Dark-Field Imaging Is Demonstrated with a Conventional Hard X-ray Source**, Physics Today (2008), March, 12 - 16

[16] M. Jiang, C. Wyatt, G. Wang, **X-ray Phase-Contrast Imaging with Three 2D Gratings**, International Journal of Biomedical Imaging, Volume 2008

[17] Timm Weitkamp, Ana Diaz, Christian David, Franz Pfeiffer, Marco Stampanoni, Peter Cloetens, Eric Ziegler, **X-ray Phase Imaging with a Grating Interferometer**, Optics Express (2005), Vol. **13**, Number 16, 6296 - 6304

[18] Andrei Bronnikov, **Phase-contrast CT: Fundamental Theorem and Fast Image Reconstruction Algorithms**

[19] Willi A. Kalender, **X-ray Computed Tomography**, Physics in Medicine and Biology (2006), Volume **51**, R29 - R43

[20] Thorsten M. Buzug, *Computed Tomography From Photon Statistics to Modern Cone-Beam CT* Springer (2008)

[21] K. Lange, R. Carson, **EM reconstruction algorithms for emission and transmission tomography**, Journal of Computer Assisted Tomography (1984), Vol. **8**, 306 - 316

[22] A. DePierro, **On the relation between the ISRA and the EM algorithm for positron emission tomography**, IEEE Transactions on Medical Imaging (1993), Vol. **12** (2), 328 - 333

[23] A. Depierro, **A modified expectation maximization algorithm for penalized likelihood estimation in emission tomography**, IEEE Transactions on Medical Imaging (1995), Vol. **14** (1), 132 - 137

[24] Dominique Van de Sompel, Sir Michael Brady, John Boone, **Task-based performance analysis of FBP, SART, and ML for digital breast tomosynthesis using signal CNR and Channelised Hotelling Observers**, Medical Image Analysis (2011), Vol. **15**, 53 - 70

[25] Paul Suetens, *Fundamentals of Medical Imaging Second Edition* Cambridge University Press (2009)

[26] Andrey Makeev and Stephen J. Glick, **Investigation of statistical iterative reconstruction for dedicated breast CT**, Medical Physics (2013), Vol. **40**, Number 8, 081904-1 - 7

[27] Albert Macovski, *Medical Imaging Systems* Prentice-Hall, Inc. (1983)

[28] Four CT Scanner Generations, mustikamax.blogspot, Web, Blogger, $\langle http://mustikamax.blogspot.com/2012/07/four-ct-scanner-generations.html \rangle$

[29] Willi A. Kalender, *Computed Tomography: Fundamentals, System Technology, Image Quality, Applications 3rd Revised Edition* Publicis Publishing, Erlangen (2011)

[30] Jerrold T. Bushberg, J. Anthony Seibert, Edwin M. Leidholdt Jr., John M. Boone, *The Essential Physics of Medical Imaging 3rd Edition*, Lippincott Williams and Wilkins (2012)

[31] James T. Dobbins III and Devon J. Godfrey, **Digital X-ray Tomosynthesis: Current State of the Art and Clinical Potential**, Physics in Medicine and Biology (2003), Vol. **48**, R65 - R106

[32] N. Oldnall, Alternate Tomographic Motions, e-radiography.net, Web, Nick Oldnall, $\langle http://www.e-radiography.net/radtech/t/tomo.htm\rangle$

[33] S. Smith, Backprojections, dspguide.com, Web, Steven W. Smith, $\langle http://www.dspguide.com/ch25/5.htm\rangle$

[34] Fourier Slice Theorem, www.mssl.ucl.ac.uk, Web, Mullard Space Science Center, $\langle http://www.mssl.ucl.ac.uk/www\_solar/moses/moses-web/Pages/fourier\_backprojection.htm\rangle$

[35] Jerry L. Prince and Jonathan M. Links, *Medical Imaging Signals and Systems*, Pearson Prentice Hall (2006)

[36] Z. Kolitsi, G. Panayiotakis, V. Anastassopoulos, A. Scodras, and N. Pallikarakis, **A Multiple Projection Method for Digital Tomosynthesis**, Medical Physics (1992), Vol. **19**, Number 4, 1045 - 1050

Chapter III

Phase-contrast Digital Tomosynthesis

Jeffrey C. Hammonds[a], Ronald R. Price, Edwin F. Donnelly, and David R. Pickens

Department of Radiology and Radiological Sciences,

Vanderbilt University Medical Center,

Nashville, TN.

(Published in similar format in *Medical Physics* 38(5): pp. 2353 - 2358, May 2011)

III.1 Abstract

Purpose

Phase-contrast (PC) edge enhancement occurs at the boundary between different tissues and is an interference effect that results from the differential phase-shifts that the x-rays acquire while traversing the two tissues. While observable in planar phase-contrast radiographs, the impact of digital tomosynthesis on this edge enhancement effect has not been previously reported. The purpose of this work is to demonstrate: (1) that phase-contrast digital tomosynthesis (PC-DTS) is possible with a conventional x-ray source, (2) that the reconstructed tomosynthesis images demonstrate and retain edge enhancement as compared to planar phase-contrast radiographs and (3) tomosynthesis improves object contrast by reducing the effects of superimposed structures.

Methods

An unmodified, commercially available cabinet x-ray system (Faxitron LX-60) was used. The system contains a tungsten anode x-ray tube that was operated at 24 kVp and 3 mAs for each PC radiographic image taken, with a nominal focal spot size of 0.010 mm. The digital detector uses CsI\CMOS with a pixel size of 0.054 mm x 0.054 mm. Objects to be imaged were attached to a computer-controlled rotating motor and are rotated $\pm 25^\circ$ about a central position in one degree increments. At each increment, three phase-contrast radiographs are taken and then averaged to reduce the effect of noise. These planar images are then used to reconstruct a series of 56 longitudinal tomographic images with an image offset increment of about 0.7 mm.

Results

Tomographic z-plane resolution was measured to be approximately 4 mm. When compared to planar PC images, the tomosynthesis images were shown to retain the PC boundary edge enhancement in addition to an improvement in object contrast.

Conclusions

Our work demonstrates that PC digital tomosynthesis retains the edge-enhancement observed in planar PC radiograph and further improves soft-tissue conspicuity by reducing the effects of superimposed tissue structure.

III.2 Introduction

A number of laboratories have previously reported the creation of planar phase-contrast radiographs using a partially coherent x-ray beam from a conventional x-ray tube [1–6]. Planar phase-contrast radiographs are characterized by an edge enhancement that results from differential phase shifts that the x-ray beam experiences as it passes through different tissues. These differential phase shifts lead to a characteristic edge enhancement at tissue boundaries due to the interference of the original beam and the diffracted x-rays. In addition to the improved conspicuity provided by edge enhancement, there is also considerable enthusiasm for phase-contrast imaging due to its potential for improved sensitivity of soft-tissue mass detection. The potential for improved mass detection sensitivity is due to the fact that the cross-section for the tissue phase shifts is approximately 1000 times greater than the absorption cross-section for x-ray energies within the range of 10 - 100 keV [7].

Due to the random three-dimensional nature of biological materials, planar phase-contrast radiography often results in a complex and frequently confusing pattern of superimposed structures and boundaries. The goal of our work was to demonstrate that phase-contrast radiography can be combined with digital tomosynthesis to preserve boundary conspicuity due to the edge enhancement and, in addition, minimize the confusion of superimposed structures.

The result of this work suggests that phase-contrast digital tomosynthesis deserves further investigation as a potentially new approach for improving soft-tissue lesion detectability in clinical mammography.

III.3 Materials and Methods

The x-ray source used for our work was a conventional small focal-spot, tungsten anode x-ray tube (Faxitron LX-60, Wheeling, IL). In this work, the tube was operated at 3 mAs and 24 kVp with the tube potential being chosen from previous work performed by our group. The nominal focal spot was 0.010 mm. The digital detector employed by this system uses CsI\CMOS elements with 2048 pixels x 2048 pixels across a 110 mm x 110 mm field of view that results in a pixel size of 0.054 mm x 0.054 mm. Additional details about the x-ray system and detector have been previously published by Donnelly et al [3].

Two phantoms were used in the study: the first phantom (Figure 3.1) was a 50 mm long, 13 mm diameter cylinder made from fiberglass resin (Bondo Corporation, Atlanta, GA) with three 2 mm diameter holes, approximately 15 mm, 17 mm, and 19 mm in length, drilled into one end. The second figure (Figure 3.2) phantom was a rectangular acrylic phantom (1 cm x 8 cm x 10 cm)with a 1 mm diameter hole drilled into the 10 cm side. This phantom was used to determine the z-axis resolution. Following the phantom measurements, image quality was assessed using a single head of broccoli (*Calabrese cultivar*).

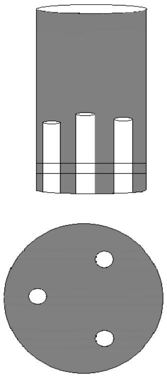

Figure 3.1: (Top) The cylindrical phantom used in the experiment. (Bottom) An enlarged, cross-sectioned view of the cylindrical phantom.

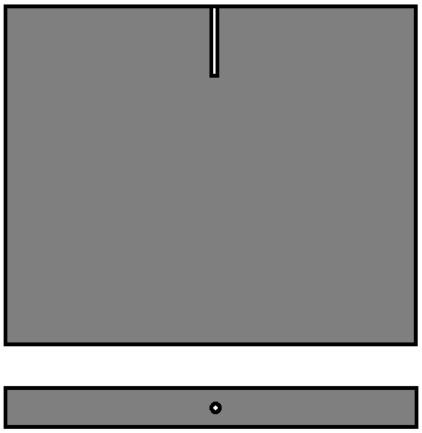

Figure 3.2: The acrylic phantom used in determining the z-axis resolution of the system.

The cylindrical phantom (Figure 3.1) was attached to a computer-controlled rotating stage and located at a source-to-object distance (SOD) of 155 mm. The detector had a source-to-image distance (SID) of 554 mm. The phantom was rotated ±25 ° about a central position in one degree increments.

At each degree increment, three phase-contrast radiographs were acquired and then averaged. The 50 averaged images were combined into one stack of images using ImageJ [8]. Images were then processed by background subtraction and flat-field corrected using a uniform flood image. No other image processing was done. A custom-written ImageJ code performed shift-and-add tomosynthesis on the processed image stack [9].

Our experimental set-up involved a modified isocentric arrangement such that the phantom rotates about an axis while the x-ray source and detector remain stationary (see Figure 3.3). This set-up is equivalent to the more traditional isocentric arrangement of the x-ray source and detector revolving synchronously about a fixed object (see Figure 3.4).

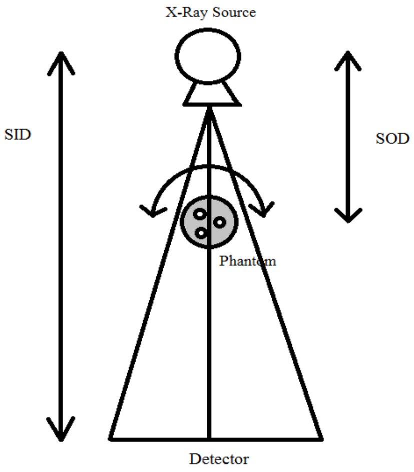

Figure 3.3: The modified isocentric experimental set-up

The ImageJ program processes the stack of phase-contrast radiographs and constructs an image stack of tomographic planes within the phantom. To perform this computation, Kolitsi *et al.* derived two formulas that were used in our tomosynthesis program [9]. The first formula for reconstructing tomographic planes not passing through the center of rotation is given by

$$h = \frac{rb\cos\omega + ld\sin\omega}{b\cos\omega - l} \tag{3.1}$$

where h represents the distance from the projected location of the rotational center on the horizontal projection plane, r is the location in a fictitious plane, b is the SOD, d is the SID, l is the phantom plane height above the rotational center, and x represents the rotation angle. The second formula

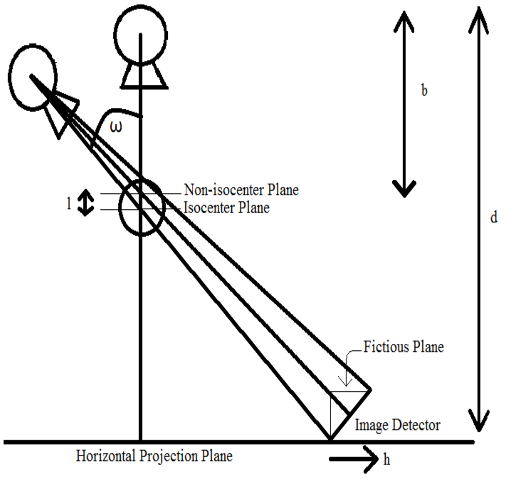

Figure 3.4: Traditional isocentric experimental set-up (Figure b adapted from Figure A1 in [9]).

for a tomographic plane that does pass through the center of rotation is

$$h = \frac{id}{d\cos\omega - i\sin\omega} \tag{3.2}$$

where i is the distance from the projected location of the rotational center in the image detector plane and the other variables are as defined above.

A. Z-axis Resolution

The longitudinal or z-axis resolution of the system was estimated from a series of tomosynthesis reconstruction planes passing through a 1 mm diameter hole in the second rectangular phantom (see Figure 3.2). The images were reconstructed using the same acquisition and reconstruction parameters as described above. After tomographic plane image reconstruction, a region of interest (ROI) was drawn at the center of the hole in each of the tomographic images and the averaged intensity values were plotted as a function of distance along the z-axis.

B. Edge enhancement

The conspicuity of the phase-contrast edge enhancement relative to noise in the reconstructed images was quantified using a modified form of the edge enhancement-to-noise ratio (EE\N) as given by Donnelly *et al* [10]. This modified EE\N is defined by the equation

$$\text{modified}\frac{EE}{N} = \frac{T-F}{\sigma_F} \tag{3.3}$$

where T represents the minimum intensity value of the edge, F represents the average intensities of 12 adjacent background pixels, and σ_F is the standard deviation of the background.

C. Image contrast

To quantify image contrast improvement, we compared image contrast for the same object in both the planar phase-contrast radiograph and the digitally reconstructed tomographic plane passing through the object. The object chosen was one of the 2 mm diameter holes within the first phantom. Identical rectangular ROIs were drawn over the image of the hole (I) and then over the adjacent background (B), first in the digitally reconstructed tomographic image and then in the planar image. Image contrast for each type of image was calculated using the equation

$$\frac{|I-B|}{\frac{I+B}{2}}\ x\ 100\%. \tag{3.4}$$

III.4 Results

A. Z-axis resolution

Images orthogonal to the beam direction were reconstructed at a center-to-center increment of 0.7 mm. The average intensity value from a rectangular region placed within the 1 mm hole was calculated and plotted as a function of distance along the z-axis (see Figure 3.5).

The full-width-at-half maximum (FWHM) of the intensity was used to estimate the spatial resolution along the z-axis. The FWHM was measured to be approximately 4.0 mm. Since we did not take into account the blurring effect of the 1 mm hole diameter, the true resolution is somewhat less than 4.0 mm.

B. Edge enhancement

The ImageJ tomosynthesis reconstruction program produced a series of 56 longitudinal tomographic images (perpendicular to the x-ray beam) reconstructed with an image offset increment of about 0.7 mm resulting in a total volume depth of 39 mm. To illustrate the combined tomographic

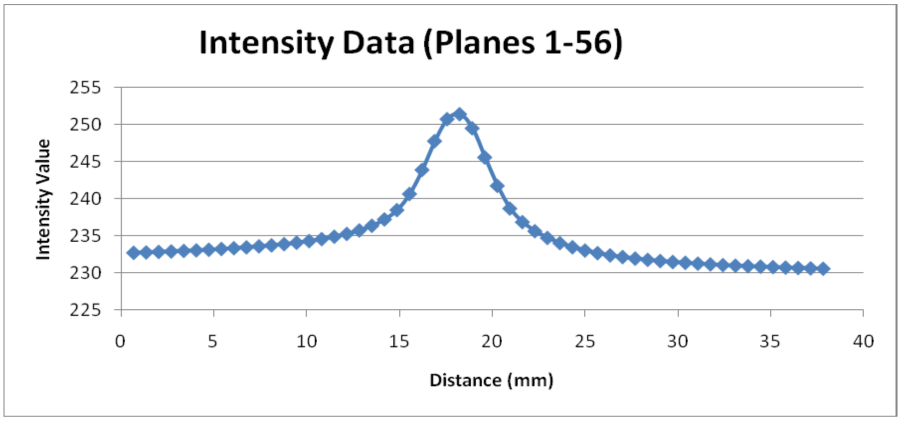

Figure 3.5: Plot of the single, averaged intensity values from the tomosynthesis reconstruction that was used in determining the spatial resolution of the system.

and phase-contrast effect, we have chosen one reconstructed image plane at a depth corresponding to the location of the center of one of the three cylindrical holes. Figure 3.6 and Figure 3.7 are the reconstructed plane and the corresponding intensity profile plot (averaged over 18 adjacent lines). From this profile plot, the phase-contrast edge enhancement is evident at the boundaries of the hole; however, note that the out-of-plane hole shows no edge enhancement.

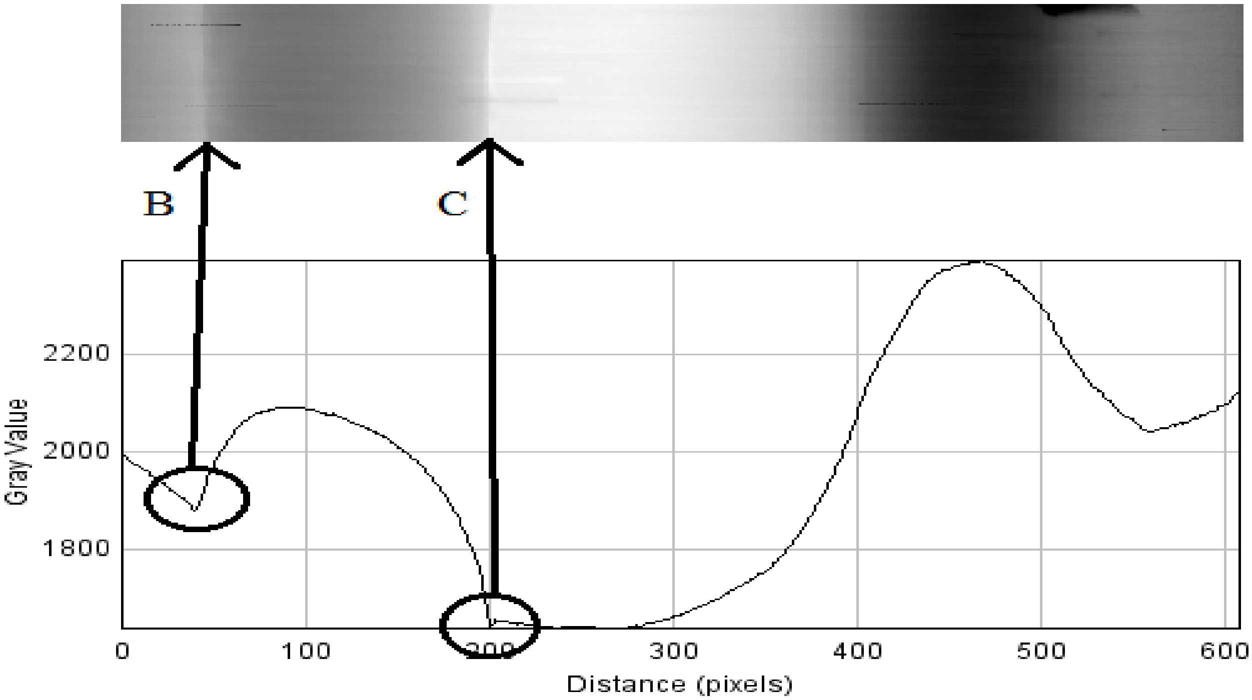

Figure 3.6: The reconstructed tomosynthesis image and the bottom is the intensity profile plot illustrating phase-contrast edge enhancement and their location in the image.

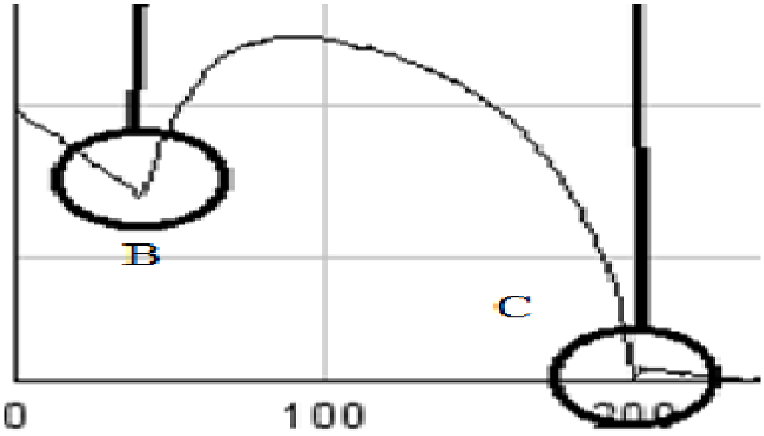

Figure 3.7: A magnified view of the phase-contrast edge enhancement.

For comparison, Figure 3.8 and Figure 3.9 shows the corresponding planar phase-contrast radiograph and intensity profile. Note that with the planar phase-contrast image, edge enhancement is also present for the out-of-plane holes (edges a and d).

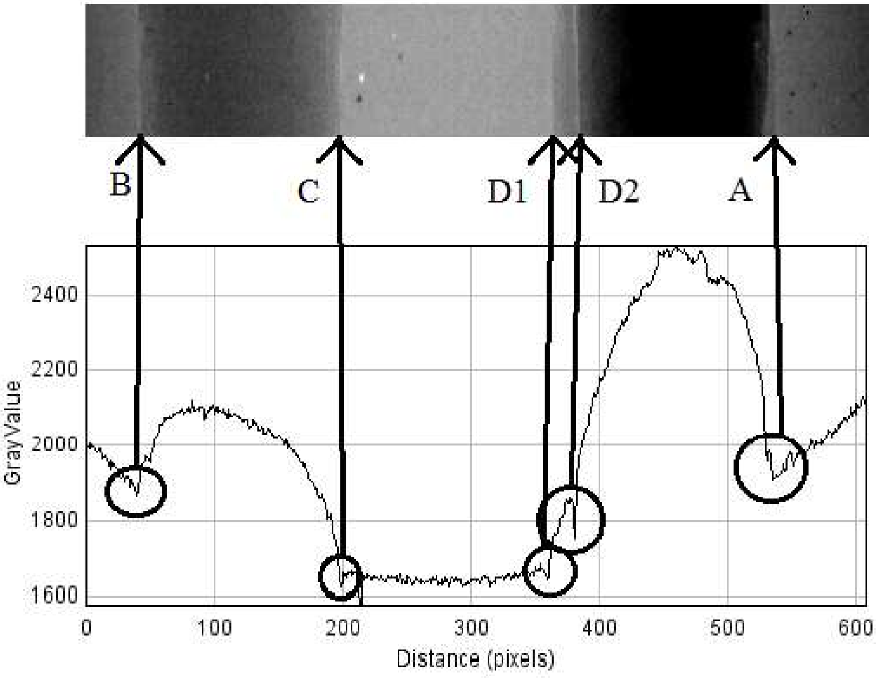

Figure 3.8: This is the phase-contrast radiographic image obtained from averaging three planar radiographs. The intensity profile plot below shows the location of four edge enhancement effects and their location on the radiographic image.

The tabulated results of modified EE\N of edges B and C for both the planar phase-contrast image and the reconstructed tomographic images are given below:

Table 3.1: EE\N

Figures	B	C
Tomographic	21.3	17
PC Radiographic	3.14	7.22

These results illustrate that edge enhancement is retained in the reconstructed tomographic images and may also be more conspicuous than that in planar phase-contrast radiographs primarily

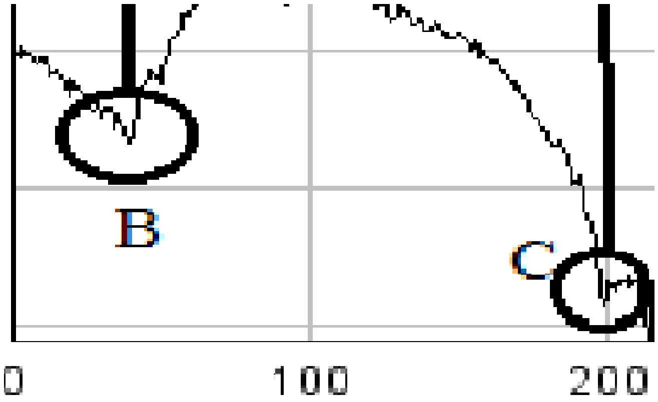

Figure 3.9: A close-up view of the edge enhancement effects. The capital letters will be used in a comparison of the modified EE\N values for the tomographic reconstruction images and this radiograph.

due to the reduced noise level that results from utilizing all 51 images to create each tomographic slice.

C. Image contrast

It is well known that digital tomosynthesis can improve image contrast by reducing the effect of overlying structures. In an attempt to quantify contrast improvement in a phase-contrast tomosynthesis image relative to planar phase-contrast radiographs, image percent contrast was defined as the relative difference of the averaged intensities between two objects (holes 1 and 2 in Figure 3.10 and Figure 3.11) in the planar phase-contrast radiograph and in the reconstructed image.

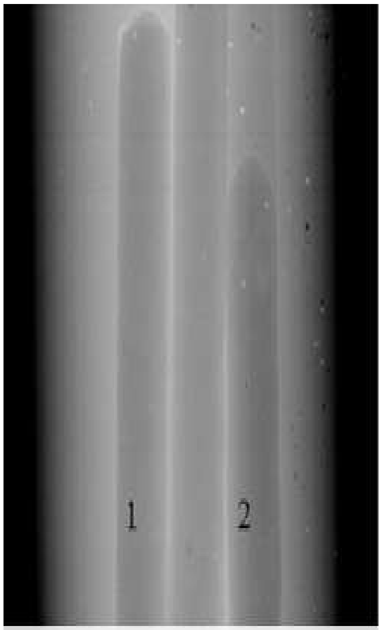

Figure 3.10: The phase-contrast radiographic image showing the two selected holes used in calculating the relative differences for this image.

The tabulated results are shown below:

Table 3.2: Image Contrast

Image	Percent Contrast
Tomographic	14.1
PC Radiographic	7.02

The results show an approximate factor of two improvement in the object contrast from the tomosynthesis reconstructed image relative to the planar radiograph.

D. Phase-contrast tomosynthesis in complex objects

We illustrate phase-contrast digital tomosynthesis when applied to a more complex, three-dimensional body such as a head of broccoli. Figure 3.12 is the planar phase-contrast radiograph and Figure 3.13, Figure 3.14 and Figure 3.15 are three reconstructed tomosynthesis images reconstructed at three different planes within the piece of broccoli.

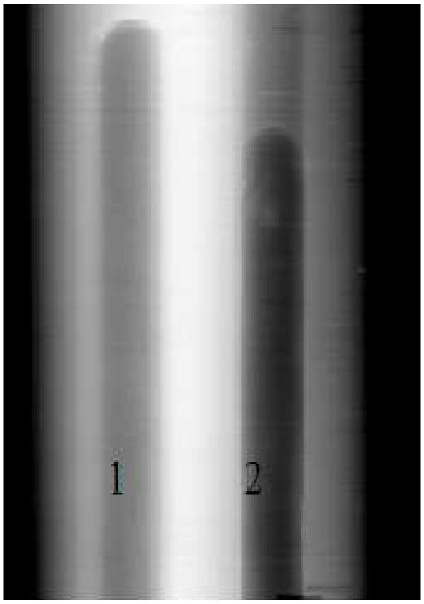

Figure 3.11: The reconstructed tomosynthesis image plane also showing the same two selected holes used in calculating the relative differences for this image.

The right-most arrow in Figure 3.12 points to two stalks that are completely superimposed. Figure 3.13 is a reconstructed image passing through the right-most stalk while the left stalk is completely blurred into the background intensity. The left arrow in Figure 3.12 points to a bulb that is completely superimposed by multiple bulbs. Figure 3.14 is a reconstructed slice through one of the superimposed bulbs. Figure 3.15 illustrates another in-focus bulb. The phase-contrast edge enhancement manifests itself as dark lines at the boundaries of the broccoli stalks and bulbs.

In Figure 3.16, we illustrate that edge enhancement is also retained in the reconstructed image of a broccoli bulb. Figure 3.16 shows a rotated, magnified view of Figure 3.13. The intensity profile from the rectangular ROI shown in Figure 3.16 illustrates the edge enhancement observed at the boundaries labeled A and B in the figure.

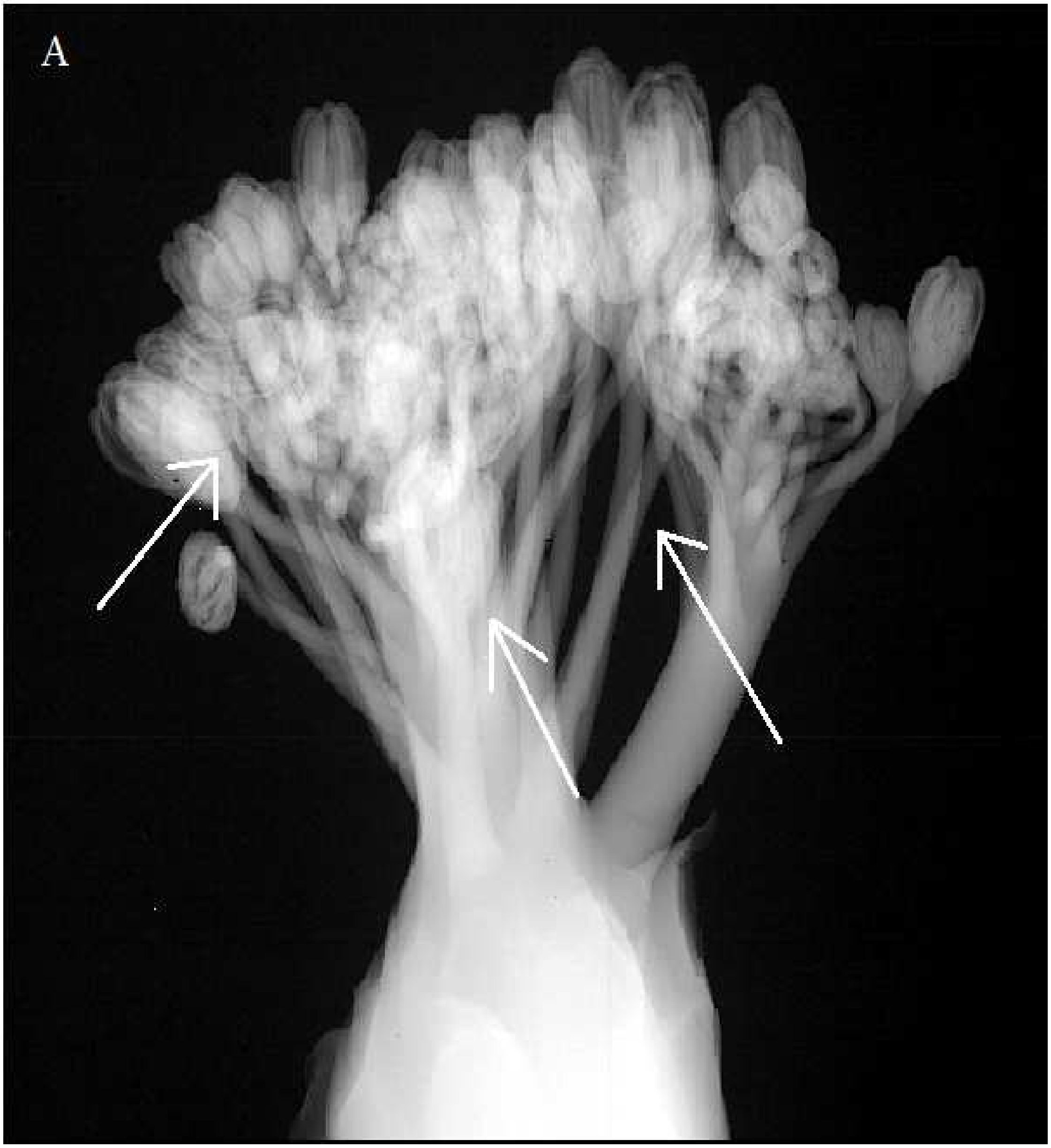

Figure 3.12: The phase-contrast radiographic image.

Figure 3.13: Plane where three broccoli stalks are in focus.

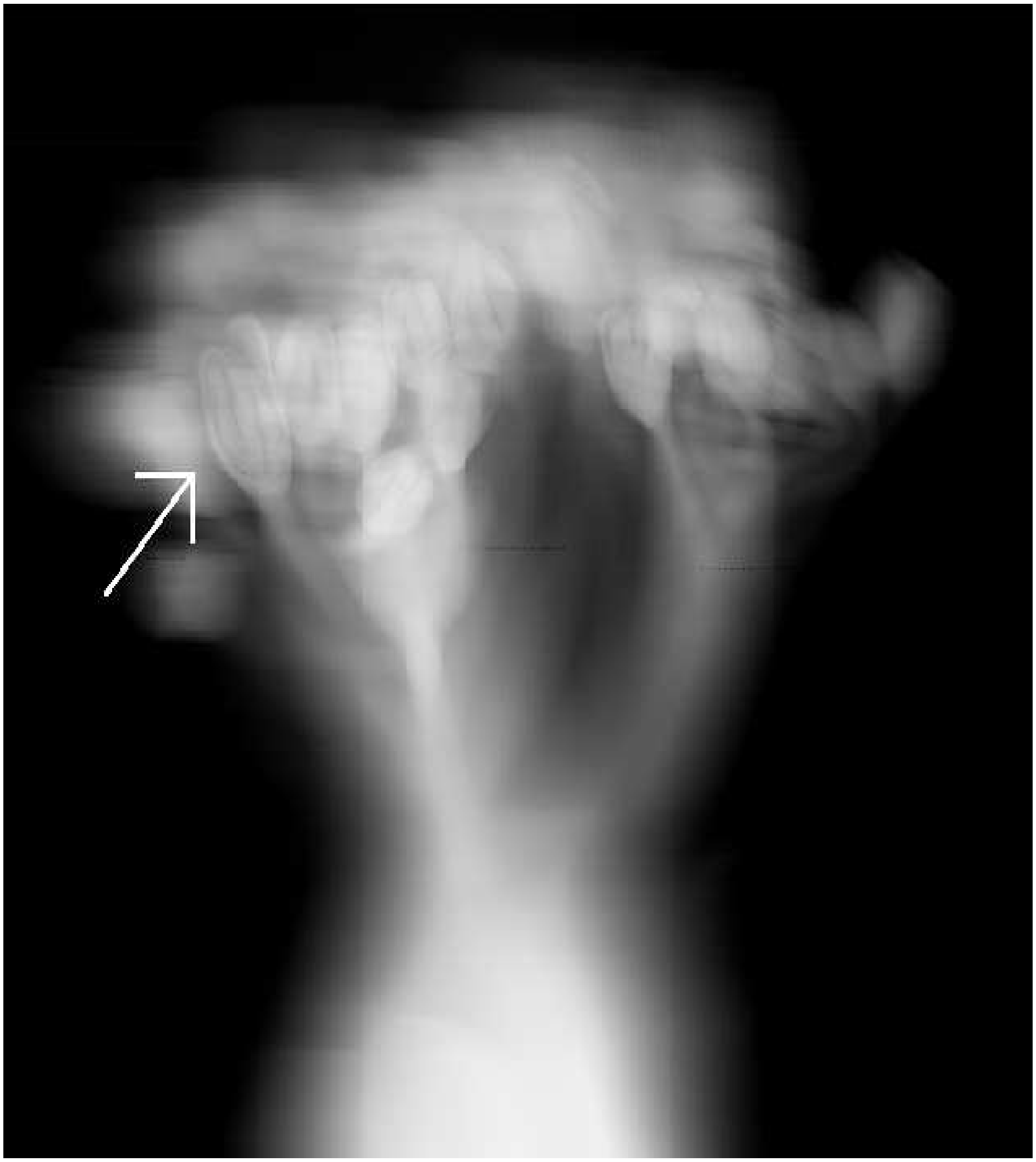

Figure 3.14: Plane where a row of broccoli buds are in focus.

Figure 3.15: A single broccoli bud in focus.

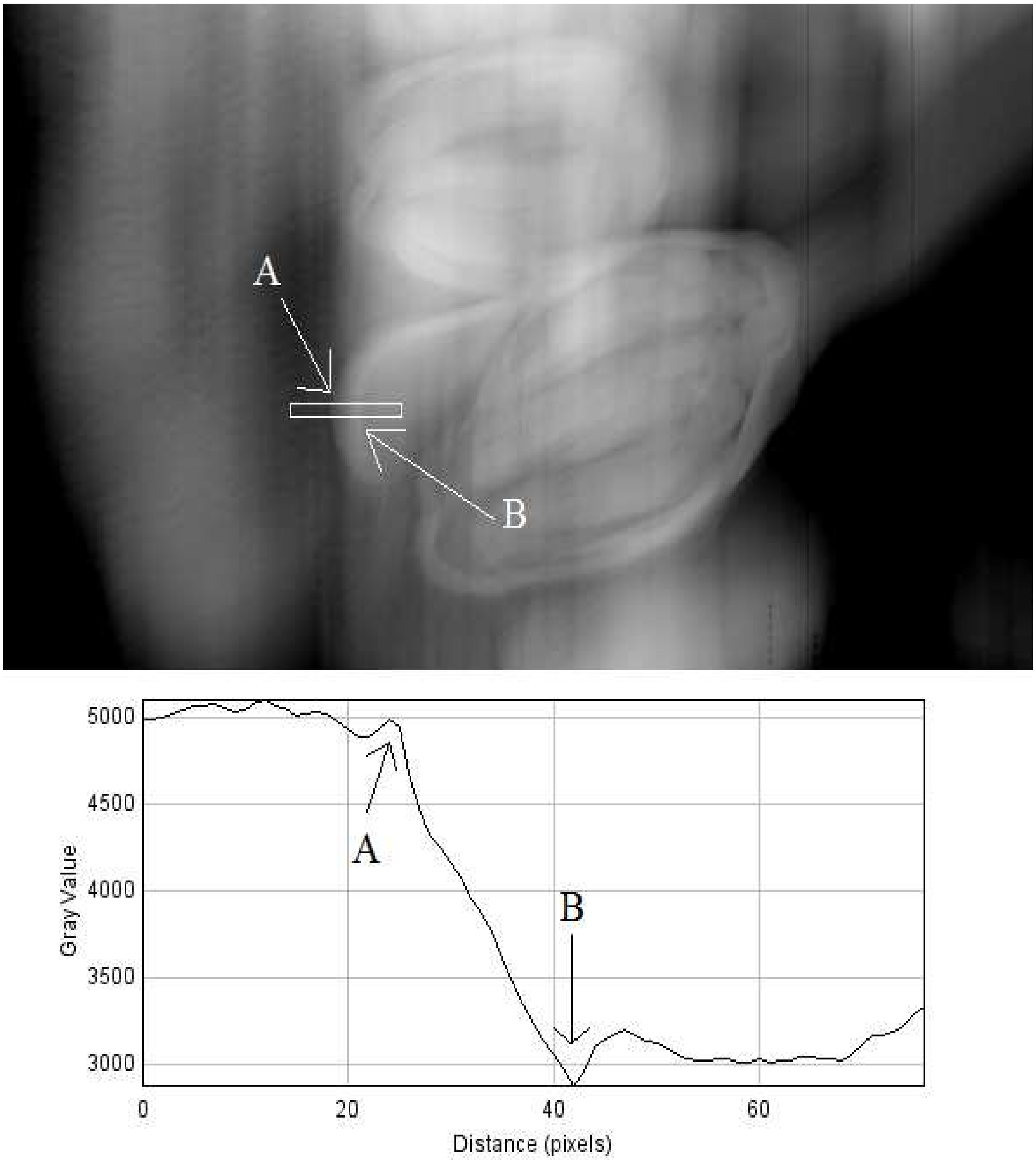

Figure 3.16: (Top) A magnified and rotated view of the bottom left image in Figure 3.14 with a ROI drawn across the boundary of a single, in-plane broccoli bulb. (Bottom) The intensity profile plot of the ROI. The letters in the image correspond to the letters in the profile.

E. Radiation exposure

It should be noted that our experimental set-up does not utilize a clinical mammography system and the radiation exposure measured does not necessarily reflect exposure in a clinical setting. At a technique of 24 kVp, 3 mAs and a 0.025 mm Mo filter with a HVL of 0.18 mm Al, the average entrance skin exposure for our system was measured to be 1280 mR per image. The total exposure for a complete tomosynthesis procedure would be approximately equal to the product of the single exposure and the number of angular increments used. At this point we have made no attempt to address dose reduction by either reducing the number of angular increments or by a reduction in the mAs per image. Dose reduction is a focus of our continuing development research. It should also be stressed that the HVL of our system is considerably lower than for a conventional mammography system (0.30 to 0.45 mm Al) and results in a somewhat higher entrance skin exposure value than clinical systems operated at the same kilovolt (peak) [11].

III.5 Conclusions

In this work, we have demonstrated that by combining phase-contrast effects with digital tomosynthesis, one can both preserve phase-contrast edge enhancement and improve object contrast. It has been reported previously that edge enhancement in planar phase-contrast radiographs of breast tissue provides significantly enhanced soft tissue conspicuity when compared to conventional planar mammography [12–14]. Independently, studies comparing digital tomosynthesis to conventional planar mammography have also shown a significant increase in diagnostic information [15, 16]. Based on our measurements of the entrance skin exposure, we believe that the dose would be comparable to conventional mammography [17]. Thus, we feel that this work has established the feasibility of phase-contrast digital tomosynthesis providing an improved method of breast imaging.

Bibliography

[1] S. Wilkins, T. E. Gureyev, D. Gao, A. Pogany, and A. W. Stevenson, **Phase-contrast imaging using polychromatic hard x-rays**, Nature (London) **384**, 335 - 338 (1996).

[2] T. J. Davis, T. E. Gureyev, D. Gao, A. W. Stevenson, and S. W. Wilkins, **X-ray image contrast from a simple phase object**, Phys. Rev. Lett. **74**, 3173 - 3176 (1995).

[3] E. F. Donnelly, K. G. Lewis, K. M. Wolske, D. R. Pickens, and R. R. Price, **Characterization of the phase-contrast radiography edge enhancement effect in a cabinet x-ray system**, Phys. Med. Biol. **51**, 21 - 30 (2006).

[4] A. Olivo and R. Speller, **A coded-aperture technique allowing x-ray phase-contrast imaging with conventional sources**, Appl. Phys. Lett. **91**, 074106-1 - 074106-3 (2007).

[5] T. Tanaka, N. Nitta, S. Ohta, T. Kobayashi, A. Kano, K. Tsuchiya, Y. Murakami, S. Kitahara, M. Wakamiya, A. Furukawa, M. Takahashi, and K. Murata, **Evaluation of computer-aided detection of lesions in mammograms obtained with a digital phase-contrast mammography system**, Eur. Radiol. **19**, 2886 - 2895 (2009).

[6] C. Honda and H. Ohara, **Advantages of magnification in digital phase-contrast mammography using a practical x-ray tube**, Eur. J. Radiol. **68S**, S69 - S72 (2008).

[7] *Biomedical Photonics Handbook*, edited by T. Vo-Dinh (CRC Press, Boca Raton, FL, 2003).

[8] W. S. Rasband, Image J, U. S. National Institutes of Health, Bethesda, Maryland, USA, $\langle http://rsb.info.nih.gov/ij/ \rangle$, 1997 - 2008.

[9] Z. Kolitsi, G. Panayiotakis, V. Anastassopoulus, A. Scodras, and N. Pallikarakis, **A multiple projection method for digital tomosynthesis**, Med. Phys. **19**, 1045 - 1050 (1992).

[10] E. F. Donnelly, R. R. Price, and D. R. Pickens, **Quantification of the effect of system and object parameters on edge enhancement in phase-contrast radiography**, Med. Phys. **30**, 2888 - 2896 (2003).

[11] J. T. Bushberg, J. A. Seibert, E. M. Leidholt, Jr., and J. M. Boone, *The Essential Physics of Medical Imaging, 2nd ed.* (Lippincott Williams and Wilkins Publishing, Philadelphia, PA, 222 - 224 2002).

[12] F. Arfelli, V. Bonvicini, A. Bravin, G. Cantatore, E. Castelli, L. Dalla Palma, M. Di Michiel, M. Fabrizioli, R. Longo, R. Hendrik Menk, A. Olivo, S. Pani, D. Pontoni, P. Poropat, M. Prest, A. Rashevsky, M. Ratti, L. Rigon, G. Tromba, A. Vacchi, E. Vallazza, and F. Zanconati, **Mammography with synchrotron radiation: Phase-detection techniques**, Radiology **215**, 286 - 293 (2000).

[13] A. Olivo, L. Rigon, S. J. Vinnicombe, K. C. Cheung, M. Ibison, and R. D. Speller, **Phase contrast imaging of breast tumors with synchrotron radiation**, Appl. Radiat. Isot. **67**, 1033 - 1041 (2009).

[14] D. Dreossi, A. Abrami, F. Arfelli, P. Bregant, K. Casarin, V. Chenda, M. A. Cova, R. Longo, R. H. Menk, E. Quaia, L. Rigon, T. Rokvic, D. Sanabor, M. Tonutti, G. Tromba, A. Vascotto, F. Zanconati, and E. Castelli, **The mammography project at the SYRMEP beamline**, Eur. J. Radiol. **68**, S58 - S62 (2008).

[15] L. T. Niklason, B. T. Christian, L. E. Niklason, D. B. Kopans, D. E. Castleberry, B. E. Opsahl-Ong, C. E. Landberg, P. J. Slanetz, A. A. Giardino, R. Moore, D. Albagli, M. C. Dejule, P. F. Fitzgerald, D. F. Fobare, B. W. Giambattista, R. F. Kwasnick, J. Liu, S. J. Lubowski, G. E. Possin, J. F. Richotte, C. Y. Wei, and R. F. Wirth, **Digital tomosynthesis in breast imaging**, Radiology **205**, 399 - 406 (1997).

[16] S. P. Poplack, T. D. Tosteson, C. A. Kogel, and H. M. Nagy, **Digital breast tomosynthesis: initial experience in 98 women with abnormal digital screening mammography**, Am. J. Roentgenol. **189**, 616 - 623 (2007).

[17] F. Arfelli, M. Assante, V. Bonvicini, A. Bravin, G. Cantatore, E. Castelli, L. Dalla Palma, M. Di Michiel, R. Longo, A. Olivo, S. Pani, D. Pontoni, P. Poropat, M. Prest, A. Rashevsky, G. Tromba, A. Vacchi, E. Vallazza, and F. Zanconati, **Low-dose phase-contrast x-ray medical imaging**, Phys. Med. Biol. **43**, 2845 - 2852 (1998).

Chapter IV

Corrosion Evaluation with Phase-Contrast Imaging

IV.1 Introduction

Corrosion is a deterioration of a material by chemical or electrochemical processes that causes the thinning of aircraft structure skins leading to a degradation of structural integrity and is a significant issue in the aging United States Air Force fleet. Aircraft such as the KC-135 and B-52 have been in use for over 50 years and have an average fleet age of 42 years [1]. Corrosion is not only an issue with older aircraft but can be a significant problem in newer aircraft due to harsh environmental conditions encountered. In fiscal year 2004, corrosion cost the Air Force 1.5 billion dollars [2]. Much of this cost is due to scheduled maintenance activities that often require the stripping of paint from the aircraft or the complete disassembly into component parts for inspection. These maintenance activities are time consuming and result in an aircraft being out of service from months to over a year. The ability to detect corrosion within an aircraft without disassembly is the main goal of non-destructive evaluation (NDE).

There are five common methods of NDE [3–5]:

- Visual Imaging: This is performed whenever the aircraft surface is visible by sight or to imaging equipment such as digital cameras or a magnifying glass. This method is fast, easy to accomplish, provides whole-field imaging and is low cost. However, problems with this method arise when there exist inaccessible regions within the aircraft to be inspected, variations in the surface quality, different lighting conditions and issues related to inspector variability. The inability of visual inspections to penetrate through the surface coatings is its major drawback.
- Ultrasonic Imaging: This method is probably the oldest and one of the most commonly used

method of NDE available. It requires the insertion of mechanical vibration energy, through contact or non-contact means (via laser-ultrasonics or electromagnetic acoustic transducers), into the aircraft substrate in the form of acoustic waves that propagate through the substrate. The aircraft structure is assessed by monitoring the speed of these waves as they propagate through the material where any localized cracks or corrosion would cause the acoustic waves to scatter. Ultrasound imaging can provide area inspection coverage and, depending on the frequency and energy level used, can obtain spatial resolutions of 10s of microns and have loss level sensitivities of 5 - 10%. However, they are time consuming, somewhat complicated to set-up and operate and require a highly trained inspector.

- Electromagnetic or Eddy Current Imaging: This is the major method of choice for detecting corrosion in aircraft structures. In this method, a probe or coil generates a localized ac electromagnetic field that is transmitted into a part of the aircraft structure and then detects that part's response due to the induced eddy currents. Defects such as corrosion and cracks perturb the eddy current and are picked up as an impedance and phase variation in the probe circuit. The advantages of the eddy current method are the capability to detect damage in thick, metallic, multi-layered structures and complex geometry structures as well as its robustness to variations in paint thickness, rivet heads and surface warping. However, like ultrasound imaging, this method is time consuming, complicates measurement procedures and typically requires a highly trained inspector. Also, the detection sensitivity and spatial resolution levels do no approach the levels as found in ultrasonic imaging.

- Thermographic Imaging: This is a relatively new NDE method that utilizes the thermal differences between the corrosion and the surrounding substrate due to the different thermal emissivities and diffusion rates. These differences can be imaged using infrared cameras and are recorded as variations in the image brightness. Thermographic imaging has the advantage of being a rapid, non-contact technique of detecting corrosion through the aircraft paint. While it is particularly useful in detecting large, near-surface corrosion areas, deeper or multi-layered regions would typically require computer enhancement.

- Radiographic Imaging This is another traditional NDE method where the x-ray energy interacts with the material and the corrosion is measured as a change in the thru-transmission material density level and provides a local measurement of the material loss. The large-area and real-time inspections are advantageous to this method but concerns about the lack of access to both sides of the component in question, the cost of inspection may be higher than the other NDE methods and possible hazardous radiation conditions still limit its widespread use.

In this chapter, phase-contrast radiography will be shown as a potential NDE method that is more sensitive to corrosion than attenuation radiography. In addition, phase-contrast digital tomosynthesis (PC-DTS) will be shown to provide corrosion depth information that is not obtainable from the previously mentioned radiographic methods. Using engineered and actual corrosion samples provided by Positron Systems Inc. and Wyle Labs, different radiographic images will be taken and the contrast ratio (CR), contrast-to-noise ratio (CNR), edge enhancement index (EEI) and the edge enhancement-to-noise ratio (EE/N) will be measured and compared. The PC-DTS volumetric images will also be obtained using both types of corrosion samples.

IV.2 Materials and Methods

Three corrosion phantoms were obtained:

- a 1/8 inch thick aluminum, engineered corrosion phantom with different geometric patterns of 0.0038 inch thick aluminum oxide (see Figure 4.1) was obtained from Positron Systems Inc. This phantom had a circular area of radius 1 inch centered on the phantom's midpoint milled down to an approximate thickness of 0.022 inches,
- a 1/8 inch thick aluminum, engineered corrosion phantom (labeled as 3C) similar to the one above except that it did not have a 1 inch radius circular area milled from the back and the aluminum oxide thickness was 0.0046 inches,
- 2 halves of an aluminum lap joint (each 1 mm x 98 mm x 76 mm) with natural corrosion (see Figure 4.2), from exposure to the natural environment at Hickam Air Force Base in Honolulu, Hawaii for one year, was obtained from Wylie Laboratories.

The milled aluminum phantom was utilized in various experiments to determine the operational system parameters while phantom 3C and the aluminum lap joint were used in the effectiveness of digital tomosynthesis in the determination of corrosion depth.

The x-ray source used for this investigation was a TFX-3125 EW dual focal spot, tungsten anode x-ray tube (Tru-Focus Corp., Watsonville, CA). The focal spot used throughout the investigation has a

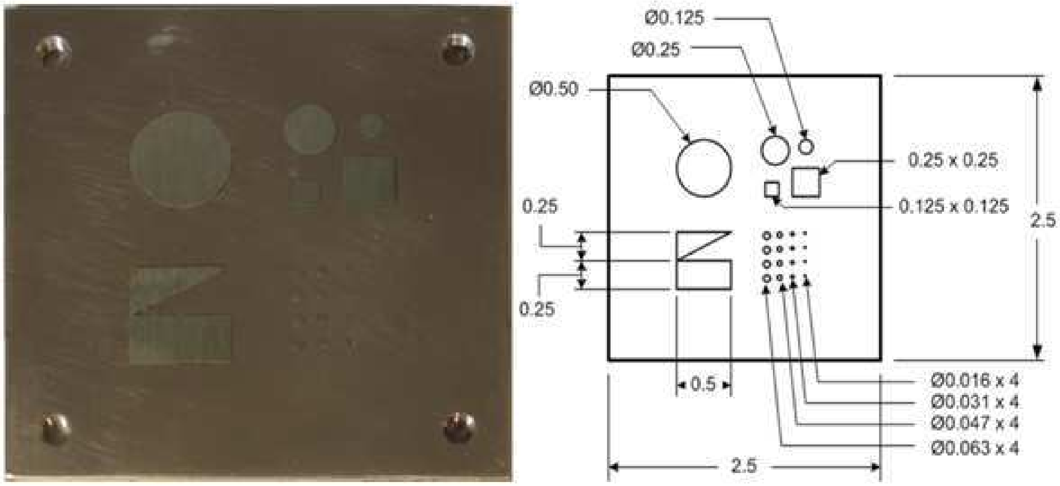

Figure 4.1: (Left) Photograph of aluminum oxide phantom. (Right) Dimensions of the different aluminum oxide patterns (inches).

nominal size of 0.010 mm. The digital detector employed uses a flat panel with amorphous selenium technology (SMAM II, Anrad Corporation, Quebec, Canada). The active area of the imager is 30.4 cm x 23.9 cm (3585 x 2816 pixels) with a pixel pitch of 0.085 mm.

Contrast as a Function of the Operational X-ray Tube Energy for Attenuation Radiography

Since the attenuation coefficients vary as a function of x-ray photon energy, the relative differences between aluminum and aluminum oxide will increase at lower energies and decrease at higher x-ray photon energies where the x-rays are more penetrating. Thus, the first goal was the determination of an operational x-ray tube energy that would provide the maximum separation based upon attenuation differences of aluminum and aluminum oxide. To quantify the separation, we used the contrast ratio (CR) defined as

$$CR = \left| \frac{I_{Al_2O_3} - I_{Al}}{I_{Al}} \right| \tag{4.1}$$

where $I_{Al_2O_3}$ is the averaged x-ray intensity within the 0.5 inch circular aluminum oxide region and I_{Al} is the averaged x-ray intensity within an equivalent thickness aluminum region without the aluminum oxide. The experimental set-up utilized a geometrical magnification factor of 3.8, an x-ray tube power output of 20 watts, no additional external filtration and a seven second exposure time. A range of peak kilovoltage values (from 20 - 120 kVp in 10 kVp increments) were used. At each kVp, three individual radiographs were obtained, averaged together and the CR was determined

Figure 4.2: Disassembled aluminum lap joint with naturally formed corrosion provided by Wyle.

after applying a 2 pixel radius median filter to the resultant image. The area of aluminum oxide used to determine the contrast ratio was from the 0.5 inch diameter circle. A rectangular region-of-interest (ROI) (118 pixels x 108 pixels) was placed in the circle and the average intensity value was found. Similarly, an identical ROI was drawn in the aluminum region close to the 0.5 inch diameter circle and the average intensity value was found in this region. Once the maximum value of CR was found, the study was repeated again by investigating the CR values within a 10 kVp region in 1 kVp increments around the voltage with the maximum CR value.

Contrast as a Function of Selected Beam Filter Materials for Attenuation Radiography

A conventional x-ray tube produces a polychromatic x-ray beam that contains a distribution of x-ray photons at different energies. This distribution of x-ray photons may be plotted against x-ray energy to create an x-ray spectrum. It may be undesirable to the final image formation to have certain x-ray energies present within the x-ray beam. Therefore, the second goal was the determination of an operational x-ray spectrum. The experimental set-up was unchanged from before, however the x-ray tube voltage was fixed at 20 kVp based upon the results from II.A. For this goal, three external elemental filters were used

- Al (0.5 mm thick)
- Cu (0.1 mm thick)
- Mo (0.025 mm thick)

Aluminum and copper tend to shift the mean energy of the x-ray beam higher by attenuating the lower energy x-rays due to their lower K-edges (1.56 keV and 8.98 keV respectively) while molybdenum tends to have the opposite effect since its K-edge is higher (19.9 keV). In addition to these individual filters, a combination filter composed from the single Al filter and the single Mo filter was also used. A simulated mammography spectrum and the associated effective energy (assuming peak tube voltage of 20 kVp, air kerma of 1 Gray and an inherent beryllium filtration thickness of 0.254 mm) was obtained for all four external filters as well as from no external filter and is shown in Figure 4.3 [6]:

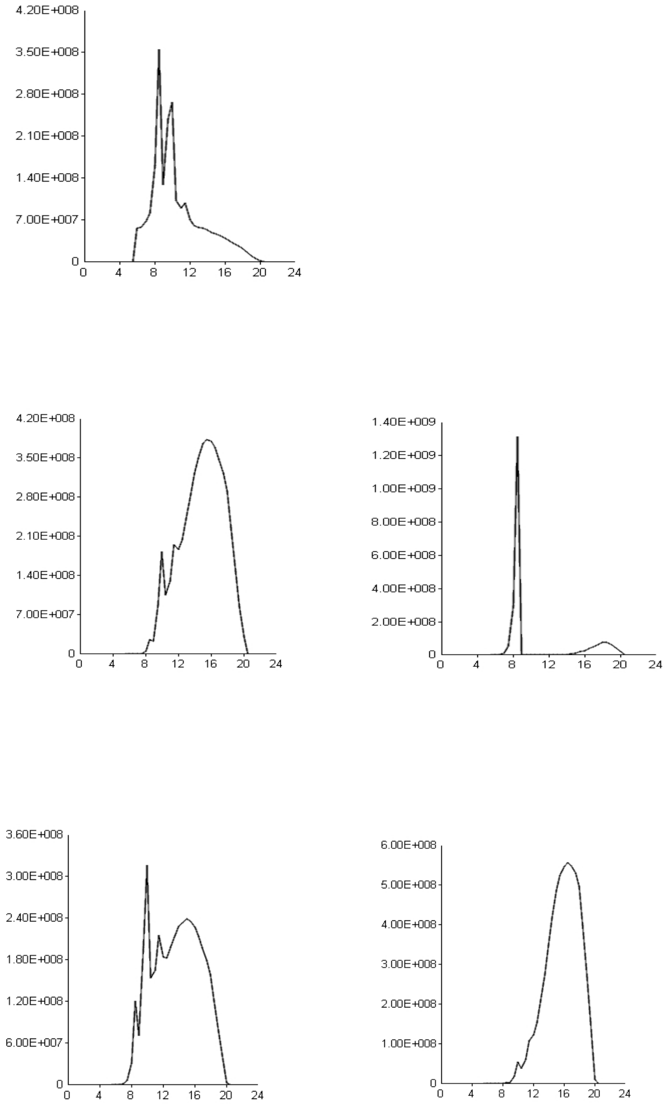

Figure 4.3: Simulated Mammography Spectrum for External Filters (abscissa in keV and ordinate in number of photons per mm^2 per keV): (Top) No external filter. (Middle Left) 0.5 mm Al. (Middle Right) 0.1 mm Cu. (Bottom Left) 0.025 mm Mo. (Bottom Right) Combination of Al and Mo Filters. Abscissa has 0.5 keV bin size for all spectra. Adapted from [6].

For each individual filter or the filter combination, six individual radiographs were obtained, averaged together and a 2 pixel radius median filter was applied. Using the same quantifier as before, the CR was measured using the same rectangular ROI and oxide pattern as in II.A.

Contrast-to-Noise Dependence on Photon Numbers

Even with excellent contrast, the image noise may make a small object undetectable. Image noise is basically a function of the x-ray tube flux which is directly proportional to number of x-ray photons (N) or to the product of the tube current (mA) and the exposure time (s). Thus, the third goal was the determination of the dependence of the image noise on mAs. The experimental set-up consisted of a geometrical magnification of 3.8, a 20 kVp x-ray tube voltage (20 watt output) with a single Mo filter (0.025 mm thick) and a seven second exposure time. 225 images with different mAs values (starting from 7 mAs to 1575 mAs in multiples of 7 mAs) were obtained and a 2 pixel radius median filter applied to each. After each median-filtered image, the contrast-to-noise (CNR) was calculated. A rectangular ROI (148 pixels x 146 pixels) was drawn inside the 0.5 inch diameter circle and the average intensity values was found. Similarly, an identical ROI was drawn in the aluminum region and the average intensity value was found as well as the standard deviation that was used to represent the noise value. The CNR is determined from the equation as

$$CNR = \frac{|I_{Al_2O_3} - I_{Al}|}{\sigma_{Al}} \tag{4.2}$$

where $I_{Al_2O_3}$ is the intensity in the 0.5 inch diameter circular aluminum oxide region, I_{Al} is the intensity in an analogous aluminum region and σ_{Al} is the standard deviation of the noise inside that analogous aluminum region.

Determination of Geometrical Settings for Phase-Contrast Radiography

As discussed in Chapter 1, two important parameters necessary for the formation of an edge enhancement are the appropriate source-to-object and object-to-image distances. The source-to-object distance (SOD or sometimes R1) allows room for the incoming x-ray wave to obtain sufficient spatial coherence and the object-to-image distance (OID or sometimes R2) allows room for the interference effect to occur. Therefore, the fourth goal was the determination of these geometrical settings necessary for maximum phase contrast edge enhancement effects. Throughout this experiment, the x-ray tube voltage was set to 20 kVp (20 watt output) with a seven second exposure and no added filtration. In order to determine the operational SOD, the OID was fixed at one meter and 12 radiographs were obtained at each of the 0.25 meter SOD increments beginning with the x-ray tube at the surface of the sample to the maximum SOD of about two meters. The twelve radiographs were then averaged together and a 2 pixel radius median filter was applied. The phase contrast edge enhancement was measured using the edge-enhancement index (EEI). The EEI is determined by

$$EEI = \frac{\frac{(P-T)}{(P+T)}}{\frac{(H-L)}{(H+L)}} \tag{4.3}$$

where P represents the peak value, T represents the trough value, H represents the higher intensity side and L represents the lower intensity side (see Figure 4.4).

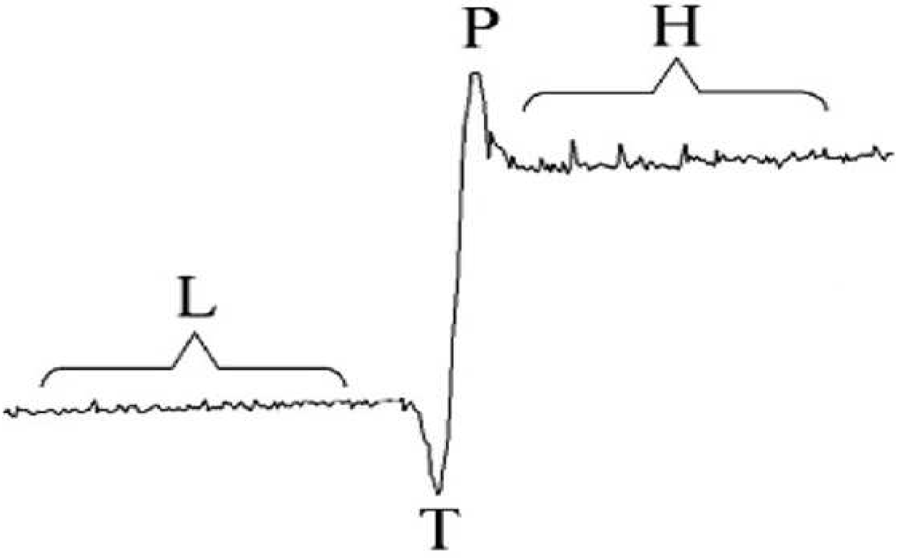

Figure 4.4: Graphical representation of the variables used in the determination of the EEI. Adapted from [7].

The H and L values were determined from an average of 20 pixels on each side. Three separate ROI (each 111 pixels x 26 pixels) were drawn on the 0.50 x 0.25 inch aluminum oxide rectangle and the EEI was evaluated for each ROI. The corresponding SOD to the maximum EEI will be the operational SOD. This particular SOD value was now fixed and the OID was then determined. This was done by obtaining 12 radiographs at each of the 0.25 meter OID increments beginning with the sample at the surface of the x-ray detector to the maximum OID of about two meters. Three EEI values were measured with three similar ROI (each 111 pixels x 26 pixels) at different locations on the same 0.50 x 0.25 inch aluminum oxide rectangle for each OID increment. The corresponding OID to the maximum EEI will be the operational OID.

Determination of the Total Rotational Arc and Step Angular Increment for Digital Tomosynthesis

All previous experiments have used a two dimensional image obtained from a three dimensional object and any spatial information about the third dimension has been lost. Digital tomosynthesis allows for this lost spatial information to be obtained. Two necessary parameters used in digital tomosynthesis are the total rotational arc and the step angular increment. Thus, the sixth goal was the determination of both the total rotational arc and the step angular increment for use in digital tomosynthesis reconstruction. The total rotational arc governs the effective slice thickness in a digital tomosynthesis reconstruction and the step angular increment governs the amount of out-of-plane blurring present in the reconstructed digital tomosynthesis slices. To determine the total rotational arc, the experimental set-up consists of an SOD = OID = 75 cm, 20 kVp tube voltage (20 watt output) and a seven second exposure. A total of four phase contrast radiographs were taken at every 1° rotation and then were averaged together. Using a comparable total rotational arc to that found in clinical settings, this was repeated over a cumulative 22° rotational arc. These 23 averaged phase contrast images were then combined into a stack of images through the program ImageJ [8]. Images were then processed by background subtraction and flat-field corrected using a uniform flood image and a 2 pixel radius median filter was then applied. A custom-written ImageJ plugin performed shift-and-add tomosynthesis on the processed image stack [9]. Tomosynthesis reconstructions were obtained for rotational arcs from $\pm 1^\circ$ to $\pm 11^\circ$ (with respect to the central image) in $\pm 1^\circ$ increments. For each reconstruction, the total rotational arc was determined from the CR values obtained from a rectangular ROI (156 pixels by 17 pixels) on the 0.50 x 0.25 inch aluminum oxide rectangle. To determine the step angular increment, a 15 image subset of the previous image data set was used. From this data set, images were selectively removed before tomosynthesis reconstruction. This selective removal consisted of removing an image at every other degree, removing two images for every two degrees, removing three images for every three degrees, etc. until all that remains is the central image and two extreme images. After each reconstruction, the contrast ratio was calculated as before to determine the operational value of the two parameters.

Digital Tomosynthesis of Phantom 3C

To validate the design parameters previously determined in II.A - II.E for a thicker sample of aluminum and to test the effect of sample thickness on the EEI, phase-contrast digital tomosynthesis was performed on the aluminum corrosion phantom 3C. The experimental set-up consists of a SOD = OID = 75 cm, an x-ray tube voltage of 40 kVp, a 14 ° rotational arc, and total mAs of 7875. A total of one hundred phase-contrast radiographs were taken at every 1 ° rotation and then were averaged together. These averaged phase contrast images were then combined into a stack of images through the program ImageJ. Images were then processed by background subtraction and flat-field corrected using a uniform flood image. A custom-written ImageJ plugin performed shift-and-add tomosynthesis on the processed image stack and a 2 pixel radius median filter was then applied. To evaluate the edge enhancement effect on the thicker engineered corrosion phantom, a rectangular ROI (65 pixels x 33 pixels) was created on the edge of the 0.125 inch square aluminum oxide pattern and the EEI and EE/N were measured as a function of step angular increment.

Additionally, using digital tomosynthesis, the depth of the corrosion was approximately determined based upon where the outlines of the corrosion come into focus in the reconstructed volumetric images. A tomosynthesis reconstruction consisting of 21 image slices (representing a total volume depth of 17.85 mm with an image offset of 0.85 mm) through phantom 3C was made. By defining the tomosynthesis reconstructed slice spacing as 10 pixels in the ImageJ tomosynthesis reconstruction program, the depth of the corrosion was calculated as:

$$\text{Corrosion Depth} = (\text{Number of Slices}) \ * \ (\text{Slice Spacing [pixels]}) \ * \ \frac{0.085 \text{ mm}}{1 \text{ pixel}} \tag{4.4}$$

Alternatively, another method of approximating the corrosion depth was found by using the same tomosynthesis data set but utilized a reconstruction through a cross-section of sample 3C (see Figure 4.5). After counting the distance from the smooth surface (with 3C etched on it) to the point of maximum concavity, multiply this value by the pixel/linear dimension relationship and the result is the approximate corrosion depth.

Phase-Contrast Radiography of an Aluminum Lap Joint

To validate the preceding results in the natural corrosion phantom, a planar phase-contrast radiograph of the natural corrosion phantom was compared to the planar attenuation radiograph of the natural corrosion phantom. The acquisition of the planar phase-contrast and planar attenuation radiographs were performed on two separate aluminum halves of a lap joint: one labeled 2555 and the other 2708. The experimental technique used in obtaining both of the planar phase-contrast radiographs consisted of an x-ray tube voltage of 35 kVp, a total mAs of 173.25 and a SOD = OID = 75 cm. A total of fifty planar phase-contrast radiographs were taken for each half and then averaged

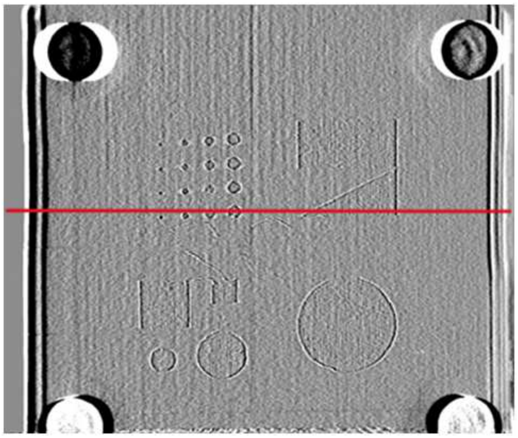

Figure 4.5: Sample 3C tomosynthesis slice showing the level where the cross-section was taken.

together. These averaged planar radiographs then had a 2 pixel radius median filter applied to them. For the acquisition of the planar attenuation radiographs, the same experimental parameters were used except for a change in the SOD and OID. The attenuation SOD was changed to 150 cm and the OID was set to 0 cm. Once obtained, the planar attenuation radiographs were averaged together and had a 2 pixel radius median filter applied to them.

The second part is to obtain a planar phase-contrast radiograph of the combined halves of an aluminum lap joint. The experimental technique used in the phase-contrast acquisition consisted of an x-ray tube voltage of 45 kVp, a total mAs of 175 and a SOD = OID = 75 cm. A total of one hundred planar phase-contrast radiographs were obtained and averaged together with a 2 pixel radius median filter applied to them.

Three rectangular ROI (182 pixels x 122 pixels) were placed in the corrosion and the non-corrosion areas of the planar phase-contrast radiograph and the average intensities of each were measured. Similarly, three rectangular ROI were placed in the corrosion and non-corrosion areas of the planar attenuation radiograph and the average intensities of each were measured. The CR of each area in both planar radiographs were calculated.

Phase-Contrast Digital Tomosynthesis of an Aluminum Lap Joint

In this section, the combined halves of the aluminum lap joint were used as the object in a digital tomosynthesis reconstruction. The experimental technique consisted of an x-ray tube voltage of 45 kVp, a mAs of 7000, a SOD = OID = 75 cm and a 80° total rotational arc where the phase-contrast radiographs were acquired in 2° angular increments. At each angular increment, one hundred planar phase-contrast radiographs were acquired and averaged together. The 40 averaged images were combined into a stack of images through the program ImageJ. Images were then processed by background subtraction and flat-field corrected using a uniform flood image. A custom-written ImageJ plugin performed the shift-and-add tomosynthesis reconstruction on the processed image stack and a 2 pixel radius median filter was then applied. The tomosynthesis reconstruction produced a volumetric image stack of 51 images (resulting in a total volume depth of 21.675 mm with an image offset of 0.425 mm). Another custom-written ImageJ plugin performed a corrosion slice location analysis based upon the assumption that the tomosynthesis slice with the greatest pixel standard deviation will occur on the corrosion level and then return this slice number.

IV.3 Results

Contrast as a Function of the Operational X-ray Tube Energy for Attenuation Radiography

From Figure 4.6, the maximum contrast ratio occurs at 20 kVp. As would be expected, the optimum kVp is likely to be the lowest available because of the rapid increase of the mass attenuation coefficient as a function of decreasing photon energy.

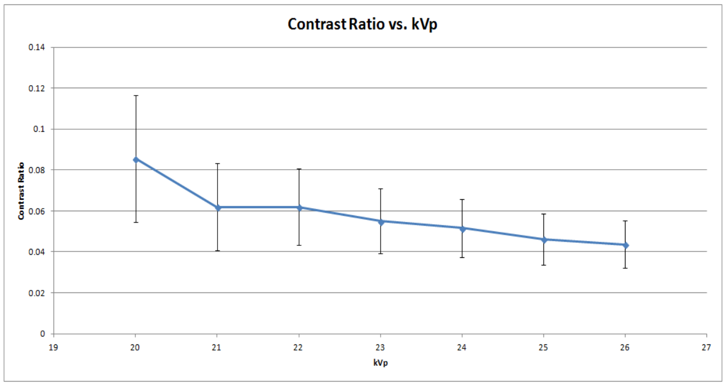

Figure 4.6: The contrast ratio as a function of kVp determined using the 0.5 inch diameter circle.

Contrast as a Function of Selected Beam Filter Materials for Attenuation Radiography

The same aluminum oxide area and an equal area of aluminum were used to determine the contrast ratio for each individual filter and the filter combination. Table 4.1 shows the contrast ratio as a function of external filtration and the greatest CR value occurs when there is no external filtration added.

Table 4.1: Contrast ratio values from the 0.5 inch diameter circle obtained at 20 kVp.

Filters	Contrast Ratio	Effective Energy [keV]
No external filter	0.086 ± 0.013	10.6
1 Mo	0.051 ± 0.013	13.7
1 Al	0.027 ± 0.012	14.9
1 Al and 1 Mo	0.026 ± 0.012	15.9
1 Cu	0.019 ± 0.006	10.6

Contrast-to-Noise Dependence on mAs

Noise can be reduced by increasing the number of x-ray photons passing through the object and can be achieved by increasing the tube current and/or increasing the exposure time. Since the image noise is proportional to the $\sqrt{mAs}$ and the image contrast difference is proportional to mAs, then CNR is proportional to the $\sqrt{mAs}$ as is seen in Figure 4.7.

Determination of the Optimal Geometrical Settings for Phase Contrast Radiography

The average EEI values are shown in Figure 4.8:

From Figure 4.8, there is a rise in EEI with increasing SOD distance as expected since increasing the SOD will provide a more coherent x-ray wavefield impinging upon the object as noted from equation (1.10) in chapter 1. Beyond the 75 cm distance, there is a decrease in EEI due to the inability to define the EEI at low flux due to noise. For a fixed OID of 1 meter, the operational EEI was taken to be at 75 cm. Note: At 0 cm, no geometric oxide patterns were found in the radiograph and an undefined value was assigned for that EEI.

Having obtained the operational SOD, the operational OID was obtained in a similar manner. The EEI values are shown in Figure 4.9:

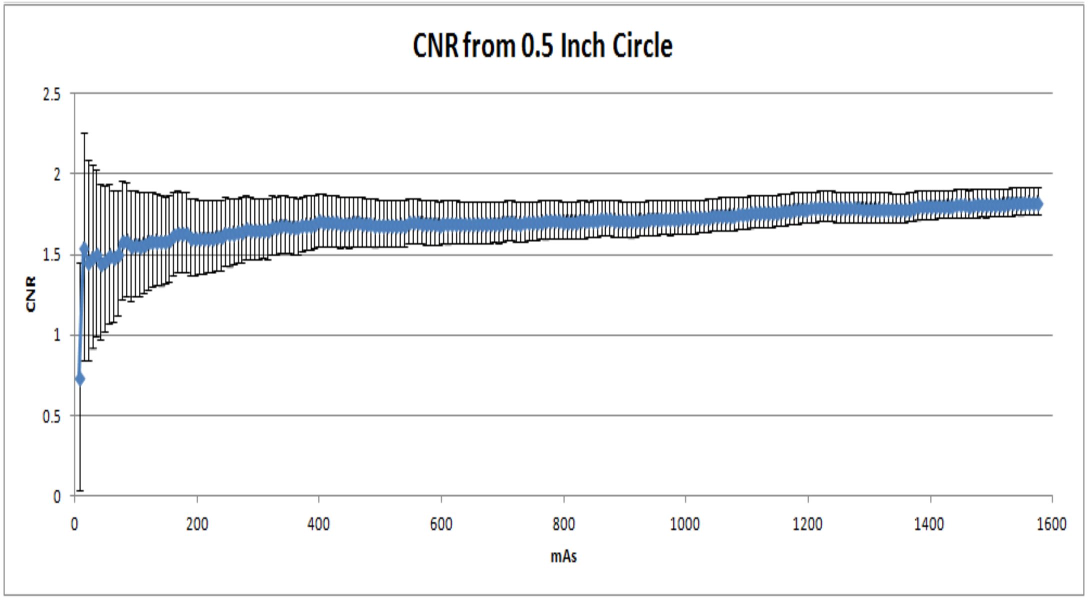

Figure 4.7: The contrast-to-noise ratio as a function of mAs for the 0.5 inch diameter circle.

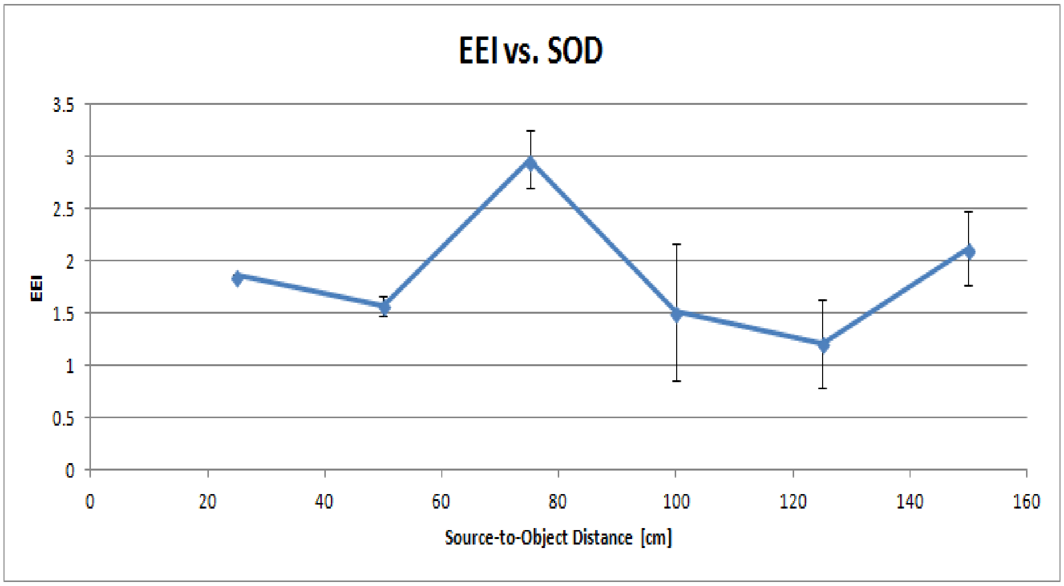

Figure 4.8: The EEI versus SOD at 25 cm intervals.

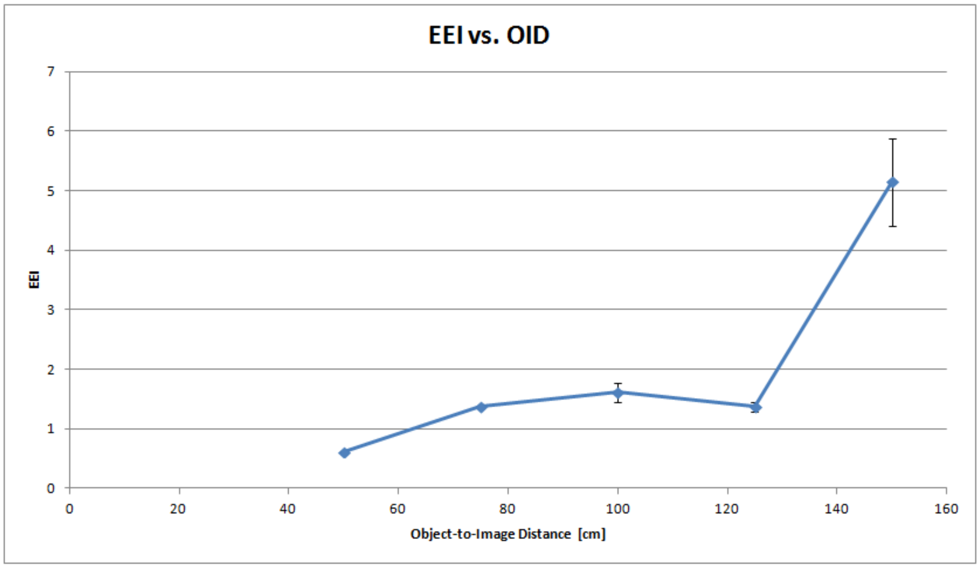

Figure 4.9: The EEI versus OID at 25 cm intervals.

For a fixed SOD of 75 cm, the EEI increases as the OID increases. This is due to the greater propagation distance for the x-ray wavefield to generate the necessary interference effects between x-ray waves of different phase shifts. The EEI goes down after 100 cm probably due to the divergence between the refracted and original x-ray waves while the high EEI value at 150 cm is likely due to noise from low flux. While the largest EEI value occurs at the 100 cm OID, the operational value of OID was chosen to be 75 cm due to the smaller uncertainty in the EEI at this distance. Note: At 0 and 25 cm, no geometric oxide patterns were found in the radiographs and an undefined value was assigned for both EEIs.

Determination of Total Rotational Arc and Step Angular Increment for Digital Tomosynthesis

From previous experiments, the total rotational arc was taken to be 22°. For the step angular increment, the more angles that are used in the tomographic reconstruction then the lower the image noise that will be present in the volumetric image. Thus the step angular increment should be 1°; however, due to the acquisition time in obtaining 1° increments, a 2° step angular increment was chosen instead.

Digital Tomosynthesis of Phantom 3C

The surface of the object with no corrosion (labeled 3C) is defined to be at 0.0 mm (see Figure 4.10).

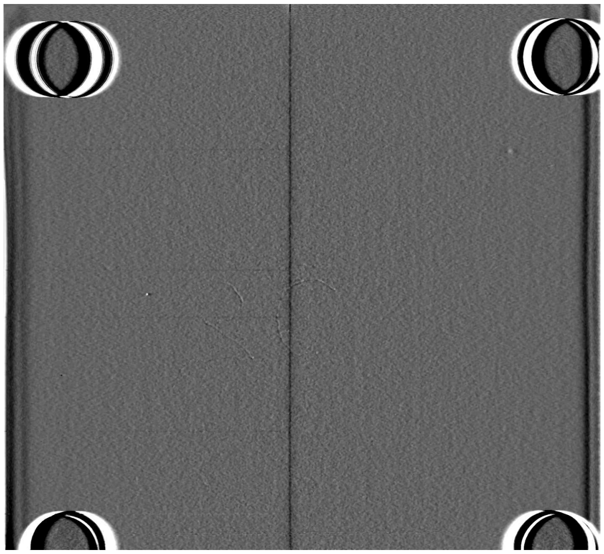

Figure 4.10: Phantom Surface 3C at 0.0 mm. Note: The vertical line is the result of the butt-joint of the Anrad detector.

With the number of slices until the geometric corrosion comes into focus as 4 and the tomosynthesis reconstructed slice spacing as 10 pixels, it was calculated from equation (4.4) that the depth of the corrosion pattern is at 3.40 mm (see Figure 4.11). This corresponds to the known thickness of the engineered corrosion phantom (1/8 inch or 3.175 mm).

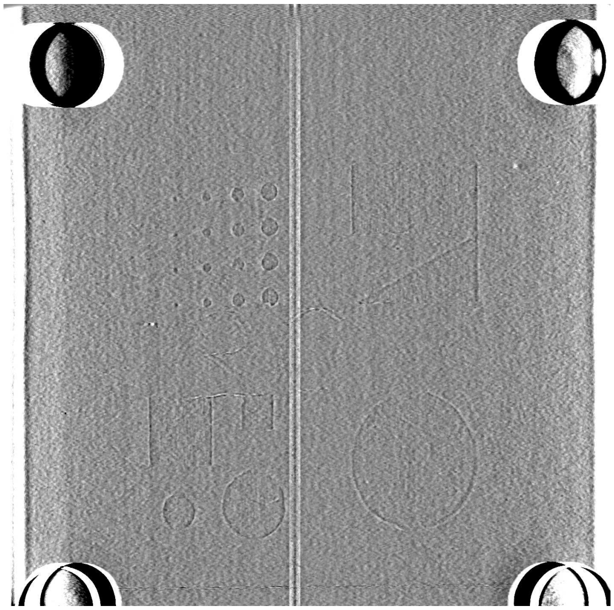

Figure 4.11: Corrosion Surface of Phantom 3C at 3.40 mm. Note: The vertical line is the result of the butt-joint of the Anrad detector.

The alternative method for approximating the corrosion depth produced the Figure 4.12:

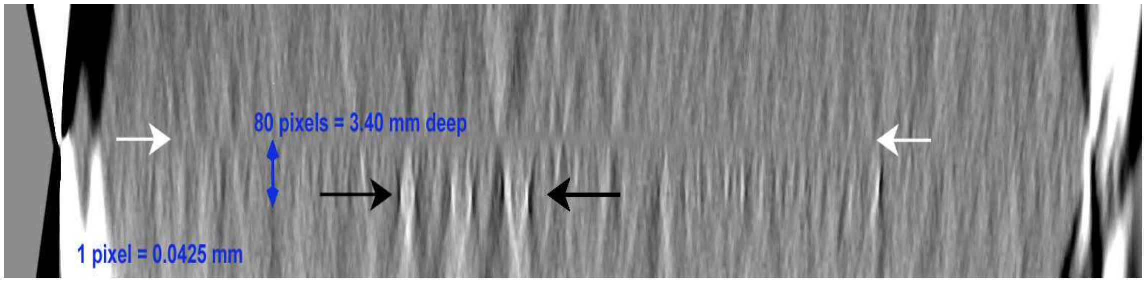

Figure 4.12: Reconstructed cross-section used in approximating corrosion depth in sample 3C. Note: The white arrows show the location of the 3C surface and the blue arrows show the location of the maximum concavity with respect to the 3C surface.

From the reconstructed cross-section, the distance from the 3C surface (white arrows) to the maximum concavity (blue arrows) is approximately 80 pixels and with 1 pixel equal to 0.0425 mm, the approximate corrosion depth is 3.4 mm. Again, this corresponds to the known thickness of the engineered corrosion phantom (1/8 inch or 3.175 mm).

Phase-Contrast Radiography of an Aluminum Lap Joint

The attenuation radiograph of plate 2555 is shown in Figure 4.13:

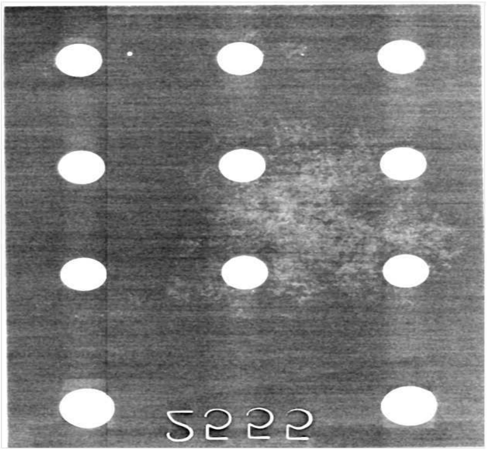

Figure 4.13: Attenuation Radiograph of Plate 2555.

and the phase-contrast radiograph of plate 2555 is shown in Figure 4.14:

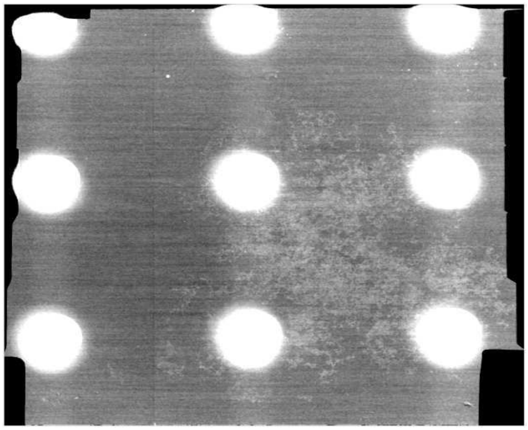

Figure 4.14: Phase-Contrast Radiograph of Plate 2555.

The calculated CR values from Figure 4.15 and Figure 4.16 are shown in Table 4.2:

Table 4.2: CR Values of Plate 2555

Phase-Contrast	Attenuation
0.0109 ± 0.0007	0.0104 ± 0.0012

Upon closer inspection of a similar area between the two middle holes on the right hand side, spatial resolution appears to be better in the planar phase-contrast corrosion radiograph than in the planar attenuation corrosion radiograph:

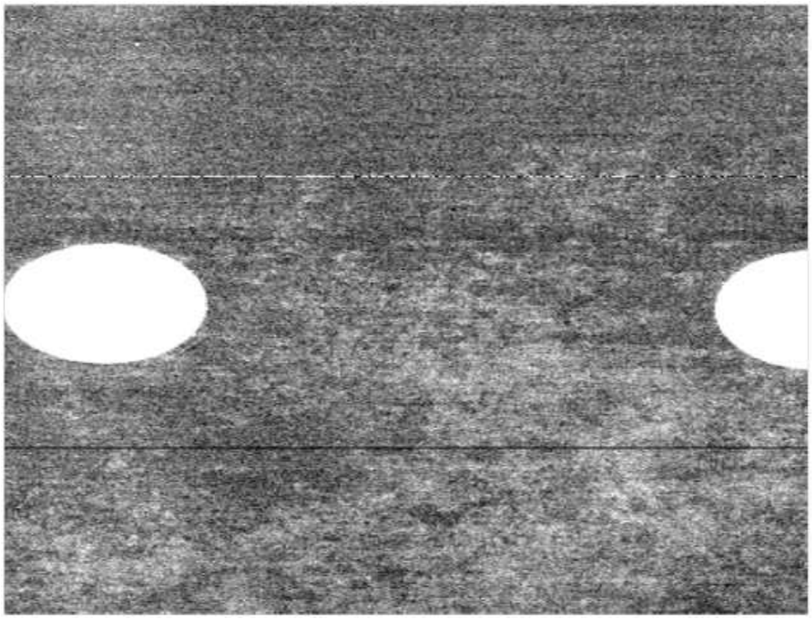

Figure 4.15: Plate 2555 Attenuation Radiograph. Note: The horizontal line is a row of saturated pixels

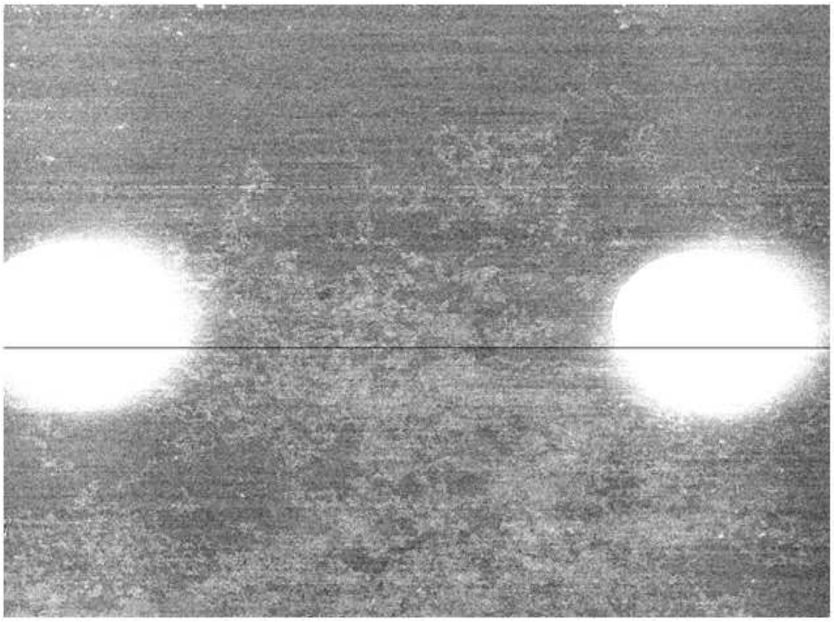

Figure 4.16: Plate 2555 Phase-Contrast Radiograph. Note: The horizontal line is a row of saturated pixels

The combination of plate 2555 and plate 2708 provides a lap joint. The phase-contrast radiograph of the lap joint is shown below in Figure 4.17:

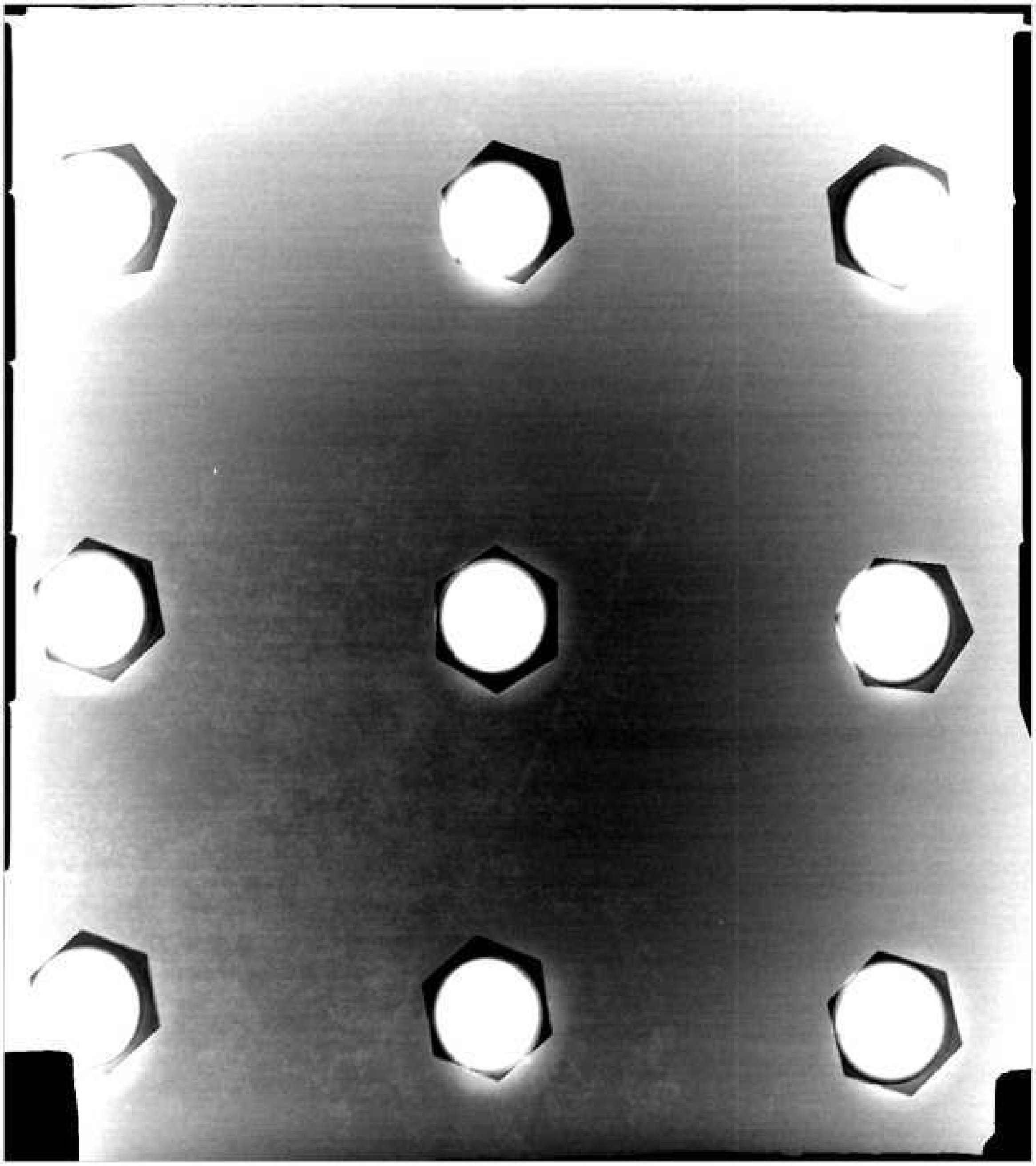

Figure 4.17: Plate 2555 and Plate 2708 Lap Joint. Note: the diagonal line is not corrosion but is a scratch in the plate 2708.

Phase-Contrast Digital Tomosynthesis of an Aluminum Lap Joint

The corrosion was found to be in-focus on the 26th image (see Figure 4.18):

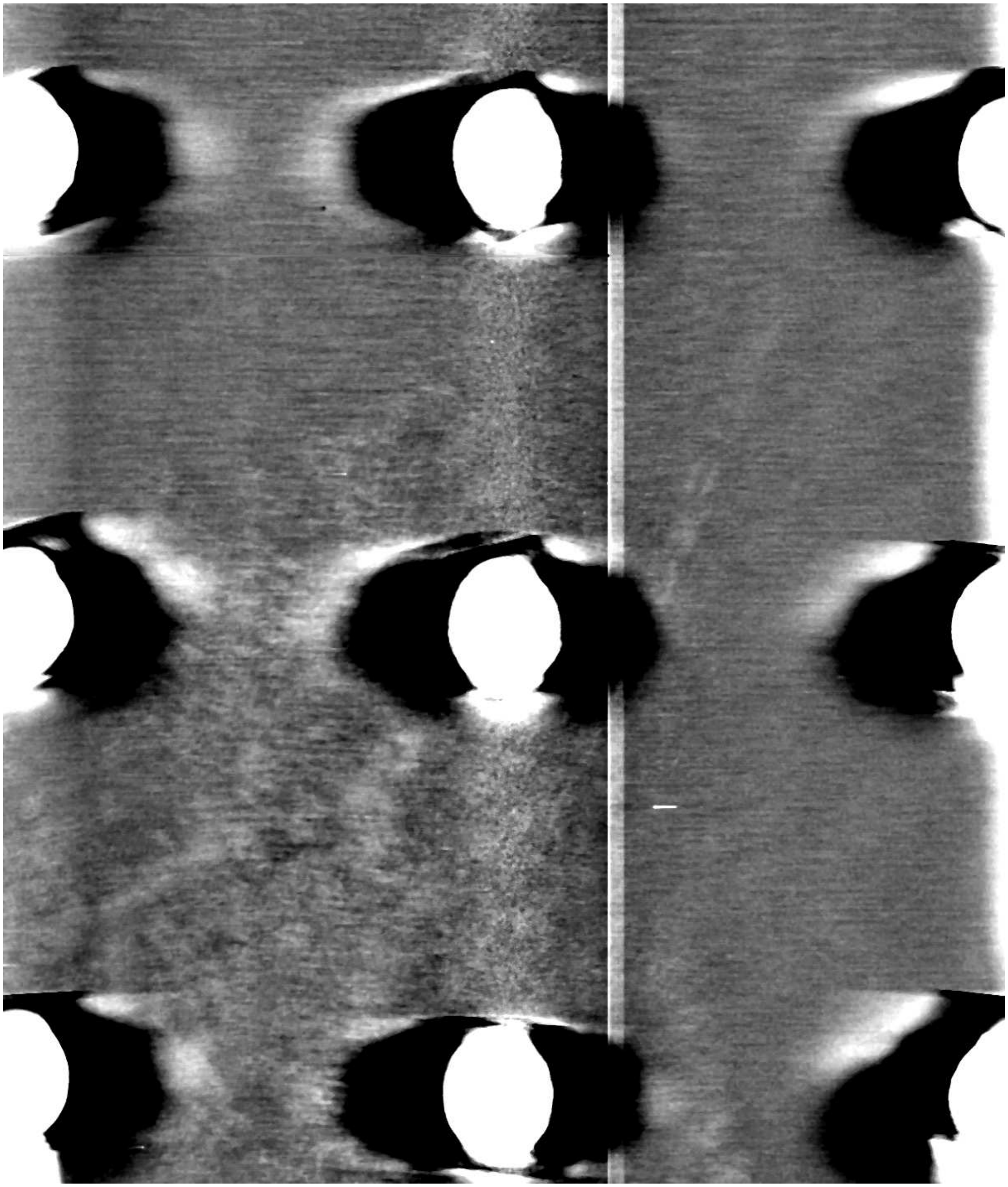

Figure 4.18: Reconstructed Tomosynthesis Slice Number 26

IV.4 Conclusions

In the determination of the operational x-ray tube energy, the value of 20 kVp was found to provide the greatest CR due to the increase in the total cross-section scattering experienced at lower x-ray energies. For the operational energy bandwidth, it was determined that the CR was better for no external filter than for any filter or filter combination involved. The impact of mAs on image noise showed that as the mAs increased, the CNR also increased because mAs $\propto$ N, contrast $\propto$ N and $\sigma \propto \sqrt{N}$, then CNR $\propto \sqrt{N} \propto \sqrt{mAs}$. The geometrical settings of SOD and OID were determined to provide the necessary distance to obtain the partial spatial coherence for the incoming x-ray wavefield and the necessary propagation distance to obtain an interference effect on the detector respectively. The operational values chosen for the geometrical settings are SOD = OID = 75 cm. The total rotational arc was chosen to be 22° based on previous experiments and the step angular increment was chosen to be 2° in order to reduce acquisition time. From Table 4.2, imaging of the individual aluminum lap joint sections using phase-contrast radiography seems to provide a better CR compared to the attenuation radiography. This result is most likely due to the better spatial resolution found in phase-contrast radiography. Digital tomosynthesis also has the potential to provide corrosion depth information as shown in section III.F. Using either the brute force method of physical counting the reconstructed slices or the cross-section reconstruction method, one can get an approximate depth of the corrosion. Also, using the assumption that the corrosion level will have the greatest standard deviation in pixel values, it is possible to find which reconstructed tomographic slice contains the corrosion as was shown in section III.H.

Chapter 4 has shown one extension of the phase-contrast digital tomosynthesis (PC-DTS) imaging method developed in chapter 3. Originally, PC-DTS was intended as a novel medical imaging technique; however, this chapter has shown that PC-DTS has the potential to be successfully applied to imaging in the aerospace industry. It also has the strong possibility of being a useful imaging technique to other parts of the industrial sector where non-destructive imaging or evaluation is highly desirable. The flexibility of PC-DTS can be extended beyond that reported in this dissertation when attached to a mobile C-arm like structure to image irregularly shaped or extended objects. However, to fully exploit PC-DTS, it is crucial to not only have a micro-focal spot x-ray source but to have the geometrical distances necessary for edge-enhancement to occur. As seen in Figures 4.8 and 4.9, there are distances where there were no corrosion patterns seen. Thus, PC-DTS can not be used with arbitrary SOD and OID distances. Also, the sensitivity of EEI to noise was noticed in this chapter. From equation 4.3, noise in an image may affect the factors in the numerator, denominator or both.

For example, if noise were to affect the peak or trough values in the numerator, this could result in a larger or smaller EEI value than would be expected. Likewise, structural noise may influence the denominator by altering the average values from the high and low areas of Figure 4.4.

Bibliography

[1] Michael Shepard, **More Miles for Tired Iron: The Application of Engineered Residual Stresses in Aging Aircraft**, August 4, 2008, Denver, Colorado.

[2] Richard Kinzie, **2004 USAF Direct Costs of Corrosion**, Air Force Corrosion Prevention and Control Office, 2004.

[3] Adam Cooney and James L. Blackshire, **Advanced Imaging of Hidden Damage under Aircraft Coatings**, Advanced Sensor Technologies for Nondestructive Evaluation and Structural Health Monitoring II edited by Norbert Meyendorf, George Y. Baaklini and Bernd Michel, Proc. of SPIE (2006), Vol. **6179**, 617902-1 to 617902-11.

[4] George A. Matzkanin and H. Thomas Yolken, **Nondestructive Evaluation Techniques for Detecting Hidden Corrosion**, The AMMTIAC Quarterly, Vol. **2**, Number 2.

[5] B.F. Peters, **Non-Destructive Testing for Corrosion Evaluation**, The Engineering Journal (March 1972), Reproduced by the National Technical Information Service, U.S. Department of Commerce

[6] Simulated X-ray Spectrum, siemens.com, Web, $\langle https://w9.siemens.com/cms/oemproducts/Home/X-rayToolbox/spektrum/Pages/Default.aspx\rangle$ (as of 02-20-2013).

[7] E. F. Donnelly, R. R. Price, and D. R. Pickens, **Quantification of the effect of system and object parameters on edge enhancement in phase-contrast radiography**, Med. Phys. **30**, 2888 - 2896 (2003).

[8] W. S. Rasband, Image J, U. S. National Institutes of Health, Bethesda, Maryland, USA, $\langle http://rsb.info.nih.gov/ij/\rangle$, 1997-2008.

[9] Z. Kolitsi, G. Panayiotakis, V. Anastassopoulus, A. Scodras, and N. Pallikarakis, **A multiple projection method for digital tomosynthesis**, Med. Phys. **19**, 1045-1050 (1992).

[10] E. F. Donnelly, K. G. Lewis, K. M. Wolske, D. R. Pickens, and R. R. Price, **Characterization of the phase-contrast radiography edge enhancement effect in a cabinet x-ray system**, Phys. Med. Biol. **51**, 21-30 (2006).

Chapter V

In-line Phase Shift Tomosynthesis

Jeffrey C. Hammonds[a], Ronald R. Price, Edwin F. Donnelly, and David R. Pickens

Department of Radiology and Radiological Sciences,

Vanderbilt University Medical Center,

Nashville, TN.

(Published in similar format to *Medical Physics*)

V.1 Abstract

Purpose

The purpose of this work is to 1) demonstrate laboratory measurements of phase shift images derived from in-line phase-contrast radiographs using the Attenuation-Partition Based Algorithm (APBA) of Yan *et al.*, 2) verify that the APBA reconstructed images obey the linearity principle, and 3) reconstruct tomosynthesis phase shift images from a collection of angularly-sampled planar phase shift images.

Methods

An unmodified, commercially available cabinet x-ray system (Faxitron LX-60) was used in this experiment. This system contains a tungsten anode x-ray tube with a nominal focal spot size of 10 μm. The digital detector uses CsI/CMOS with a pixel size of 50 μm x 50 μm. The phantoms used consisted of one acrylic plate, two polystyrene plates and a habanero pepper. Tomosynthesis images were reconstructed from 51 images acquired over a ± 25 degree arc. All phase shift images were reconstructed using the APBA.

Results

Image contrast derived from the planar phase shift image of an acrylic plate of uniform thickness exceeded the contrast of the traditional absorption image by an approximate factor of two. Comparison of the planar phase shift images from a single, uniform thickness polystyrene plate with two polystyrene plates demonstrated an approximate linearity of the estimated phase shift with plate thickness (-1600 radians vs. -2970 radians). Tomographic phase shift images of the habanero pepper exhibited acceptable spatial resolution and contrast comparable to the corresponding attenuation image.

Conclusions

This work demonstrated the feasibility of laboratory-based phase shift tomosynthesis and suggests that phase shift imaging could potentially provide a new imaging bio-marker. Further investigation will be needed to determine if phase shift contrast will be able to provide new tissue contrast information or improved clinical performance.

V.2 Introduction

A number of laboratories have previously reported the creation of planar phase-contrast radiographs using a partially-coherent x-ray beam from a conventional x-ray tube [1–3]. Planar phase-contrast radiographs are characterized by an edge enhancement that results from differential phase shifts that the x-ray beam experiences as it passes through different tissues. These differential phase shifts lead to a characteristic edge enhancement at tissue boundaries due to the interference of the original x-ray wavefront with the diffracted x-rays. In addition to the improved conspicuity provided by edge enhancement, there is also considerable enthusiasm for phase-contrast imaging due to its potential for improved sensitivity of soft-tissue mass detection [4]. While there are different methods to produce a phase-contrast image, the one used in this technical note is the in-line or free-space propagation method, which is the simplest method due to the lack of any x-ray optics needed. The in-line method relies upon a micro-focus x-ray source to generate a partially coherent x-ray wave that propagates to the sample and a non-zero object-to-image distance (OID) that allows the diffracted and non-diffracted x-ray waves to propagate freely until their detection as intensity variations on a detector due to constructive and destructive interference effects between the two x-ray waves.

The origin of this phase shift lies in the refractive decrement of the complex index of refraction, n,

$$n = 1 - \delta + i\beta \tag{5.1}$$

where δ is the refractive decrement and β is the component responsible for attenuation. The phase shift experienced by the x-ray as it traverses an object is given by

$$\Delta\phi = -\frac{2\pi}{\lambda}\int \delta\left(s\right)ds = -\frac{hc}{E}r_e\int \rho_e\left(s\right)ds = -\frac{hc}{E}r_e\rho_{e,p} \tag{5.2}$$

where $\Delta\phi$ is the amount of the x-ray phase shift with respect to the vacuum x-ray phase, λ is the x-ray wavelength, h is Planck's constant, c is the speed of light, E is the x-ray energy, r_e is the classical electron radius, and $\rho_{e,p}$ is the projected electron density from the integration of the electron density ρ_e along the x-ray path length [5, 6]. Thus, the phase shift is equivalent to a measure of the phantom's projected electron density. Thus, the phase shift is equivalent to a measure of the phantom's projected electron density.

Algorithms for retrieving phase shift information from planar phase-contrast images have been previously proposed and used to produce planar phase shift images [7–10]. In this work we have chosen to use the algorithm published by Yan, *et al.* [6]. The attenuation-partition based algorithm

(APBA) is an iterative algorithm that uses two acquired radiographs (the attenuation and phase-contrast) and, by taking advantage of the correlation between the phase and attenuation due to the phase-attenuation duality found at higher x-ray energies (60 keV or higher), produces a planar phase shift image. APBA has the advantage of being robust against quantum noise; however, the convergence speed is proportional to the amount of correlation between the object's phase and attenuation [6].

Other approaches to phase shift imaging have been demonstrated. These include diffraction enhanced imaging (DEI) tomosynthesis, grating-based differential phase contrast (DPC) tomosynthesis, an in-line phase contrast imaging method by Zhang *et al.*, and a grating-based differential phase-contrast computed tomography (DPC-CT) [11–15]. Of particular interest is the multi-contrast DPC method that employs the Talbot-Lau interferometry that can be achieved either with or without mechanical phase stepping of the gratings. A limitation of the DPC method with multi-shot phase stepping is the speed of data acquisition. However, the DPC method without phase stepping uses a single shot acquisition that can significantly improve acquisition speed but at the expense of anisotropic spatial resolution. The potential advantages of the proposed in-plane phase shift system discussed here include: 1) no need for gratings that are generally limited to lower x-ray energies, 2) no trade-off between acquisition speed and spatial resolution and 3) minimal restriction on the image field-of-view.

V.3 Materials and Methods

The x-ray source used was a conventional small focal-spot, tungsten anode x-ray tube (Faxitron LX-60, Wheeling IL). For the biological phantom, the tube was operated at 36 kVp and 0.3 mAs; for the non-biological phantoms, the tube was operated at 36 kVp and 1.8 mAs. The nominal focal spot was 0.010 mm. The digital detector employed by this system uses CsI/CMOS elements with 2368 pixels x 2340 pixels across a 118.4 mm x 117.0 mm field of view that results in a pixel size of 0.05 mm x 0.05 mm. Additional details about the x-ray system and detector have been previously published by Donnelly *et al* [3].

Three phantoms were used in this work: one (10 cm x 10 cm x 0.3 cm) acrylic plate, two (10 cm x 10 cm x 0.1 cm) polystyrene plates, and a habanero chili pepper (*Capsicum chinense*). Both the acrylic and polystyrene plates had a source-to-detector distance (SDD) of 554 mm and an object-to-detector distance (ODD) of 414 mm for the phase-contrast image acquisition. For the attenuation image acquisition, the acrylic and polystyrene plates had a SDD of 554 mm and ODD of approximately 0 mm (contact). The planar attenuation radiographs and the planar phase-contrast radiographs were placed into two distinct image stacks using ImageJ, each stack was averaged to a single image and then processed by background subtraction and flat-field corrected using a uniform flood image [16]. No other image processing was done. The corrected planar phase-contrast image and the corrected attenuation image were then used as inputs for the attenuation-based partition algorithm (ABPA) [10]. This produced one phase shift image after 10 iterations for both acrylic and polystyrene plates.

The habanero pepper was attached to a computer-controlled rotating stage and located at a source-to-object distance (SOD) of 460 mm. The detector had a ODD of 212 mm for the planar phase-contrast acquisition and an ODD of 73 mm for the planar attenuation acquisition. The pepper was rotated 51 degrees about a central position in one degree increments. At each degree increment, a planar attenuation radiograph and a planar phase-contrast radiograph were separately acquired. The planar attenuation radiographs and the planar phase-contrast radiographs were placed into two distinct stacks using ImageJ and then processed by background subtraction and flat-field corrected using a uniform flood image [16]. No other image processing was done. One planar attenuation radiograph and the angularly coincident planar phase-contrast radiograph were used as the ABPA inputs. This generated one planar phase shift image per degree increment after 10 iterations. This process was repeated to produce a 51 planar phase shift image dataset.

Our experimental set-up involved a modified isocentric arrangement such that the habanero pepper rotates about an axis while the x-ray source and detector remain stationary. This set-up is equivalent to the more traditional isocentric arrangement of the x-ray source and detector revolving synchronously about a fixed object. Figure 5.1 illustrates the geometric set-up of our system. For the acrylic and polystyrene plates, the experimental set-up was similar to Figure 5.1 except that the plates remained stationary during the entire acquisition process.

Planar Image Contrast

To quantify image contrast improvement in the planar phase shift image, we calculate the contrast-to-noise ratio (CNR) using two identical rectangular regions-of-interest (ROIs) in the acrylic attenuation image and the acrylic phase shift image. One ROI was drawn in the acrylic region and another identical ROI was drawn in the air region. CNR was calculated using the equation

$$\left|\frac{I_{acrylic} - I_{air}}{\sigma_{air}}\right| \tag{5.3}$$

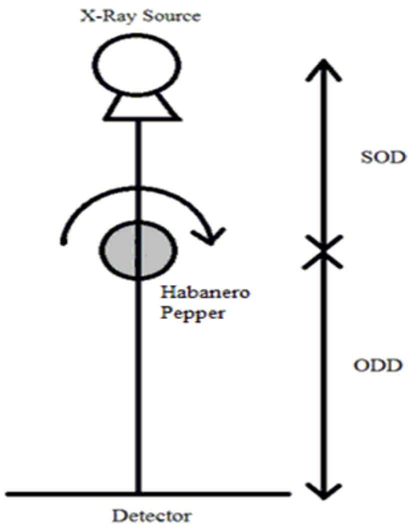

Figure 5.1: Experimental set-up.

where $I_{acrylic}$ is the absolute average value in the acrylic region, I_{air} is the absolute average value in the air region and σ_{air} is the standard deviation in the air region.

Linearity

A system is linear if a weighted sum of input signals results in an output that also consists of a weighted summation of the responses of the system to each individual input signal [17]. To verify that the ABPA obeys the linearity principle, the average phase shift value within an identical ROI from the single polystyrene plate and the dual polystyrene plates were compared.

3D Tomogram Image Contrast

To quantify image contrast improvement in the longitudinal tomographic phase shift reconstruction, we compared the image contrast using two identical ROIs in the phase shift reconstruction to the image contrast found in the attenuation longitudinal tomographic reconstruction. The identical ROIs were drawn over the image of one of the pepper seeds (A) and then over the adjacent background (B) with σ_B the standard deviation in the background ROI. The image contrast was calculated using the CNR equation:

$$\frac{|I_A - I_B|}{\sigma_B} \tag{5.4}$$

V.4 Results

Planar Image Contrast

Below are two planar images of the acrylic plate:

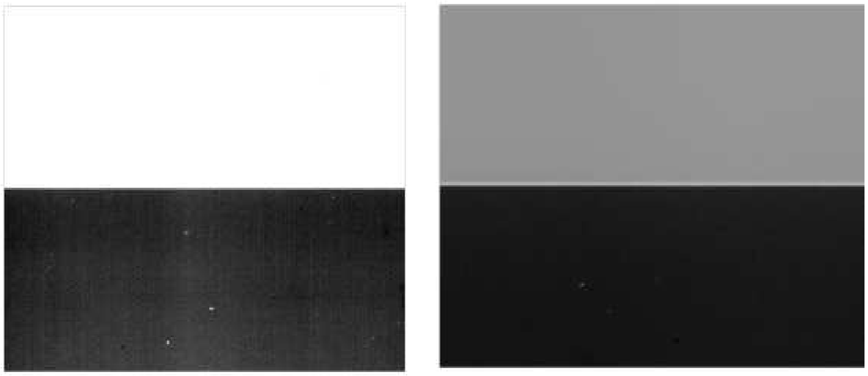

Figure 5.2: (Left) Acrylic attenuation image. (Right) Acrylic phase shift image. Note: The air region is on top and the acrylic region is on the bottom in both images.

An identical, rectangular (140 x 357 pixels) ROI was drawn in both images in the acrylic and air regions. The average intensity value from those regions were obtained from each image as well as the standard deviation from the air region. The CNR was calculated and displayed in Table 5.1:

Table 5.1: CNR Values for Absorption and Phase Shift Images.

Acrylic Image	Image Contrast
Attenuation	51 ± 1
Phase Shift	101 ± 2

The CNR for the phase shift image was found to be approximately a factor of two greater than the CNR measured in the conventional attenuation image.

Linearity

To verify that the ABPA maintains the principle of linearity, an identical, rectangular (140 x 357 pixels) ROI was drawn within the polystyrene region in both the single and dual polystyrene plates phase shift images. The values in the polystyrene region were averaged together and displayed in Table 5.2.

Table 5.2: Linearity.

Number of Polystyrene Plates	Phase Shift Values [radians]
1	-16$\underline{0}$0 ± 30
2	-2970 ± 40

Within the uncertainties of the measurements, we found that the estimated phase shift was consistent with linearity with plate thickness.

3D Tomogram Image Contrast

51 images were used in a custom-written ImageJ tomosynthesis reconstruction program, details of which have been previously published by Hammonds *et al* [18]. The ImageJ tomosynthesis reconstruction program produced a series of 51 longitudinal tomographic images (perpendicular to the x-ray beam) reconstructed with an image offset increment of 0.5 mm resulting in a total volume depth of 25.5 mm. In Figure 5.3, the planar attenuation radiograph and the planar phase shift map are shown:

In Figure 5.4, the tomosynthesis reconstructed phase shift images is shown along with the tomosynthesis reconstructed attenuation image for comparison. All tomosynthesis reconstructed images have the same image offset increment and were derived from the same subset of images from within their respective image stacks. No filter was applied during either tomographic reconstructions.

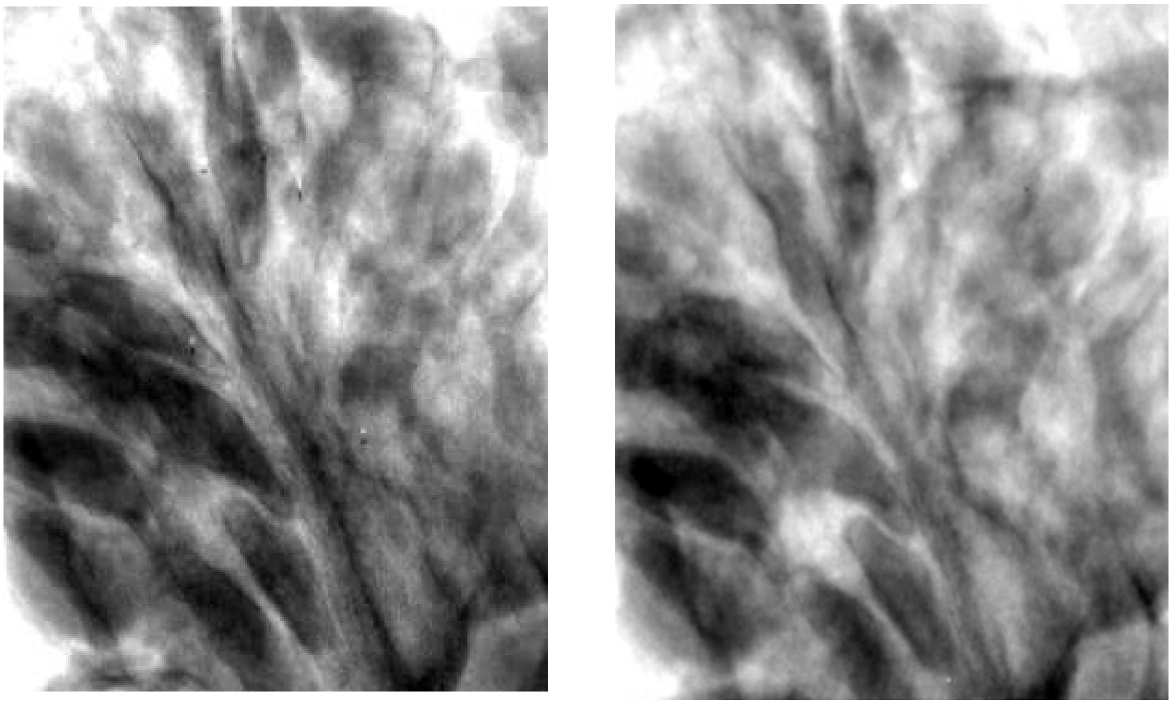

Figure 5.3: Figure 3: (Lef) Planar attenuation radiograph. (Right) Planar phase shift map.

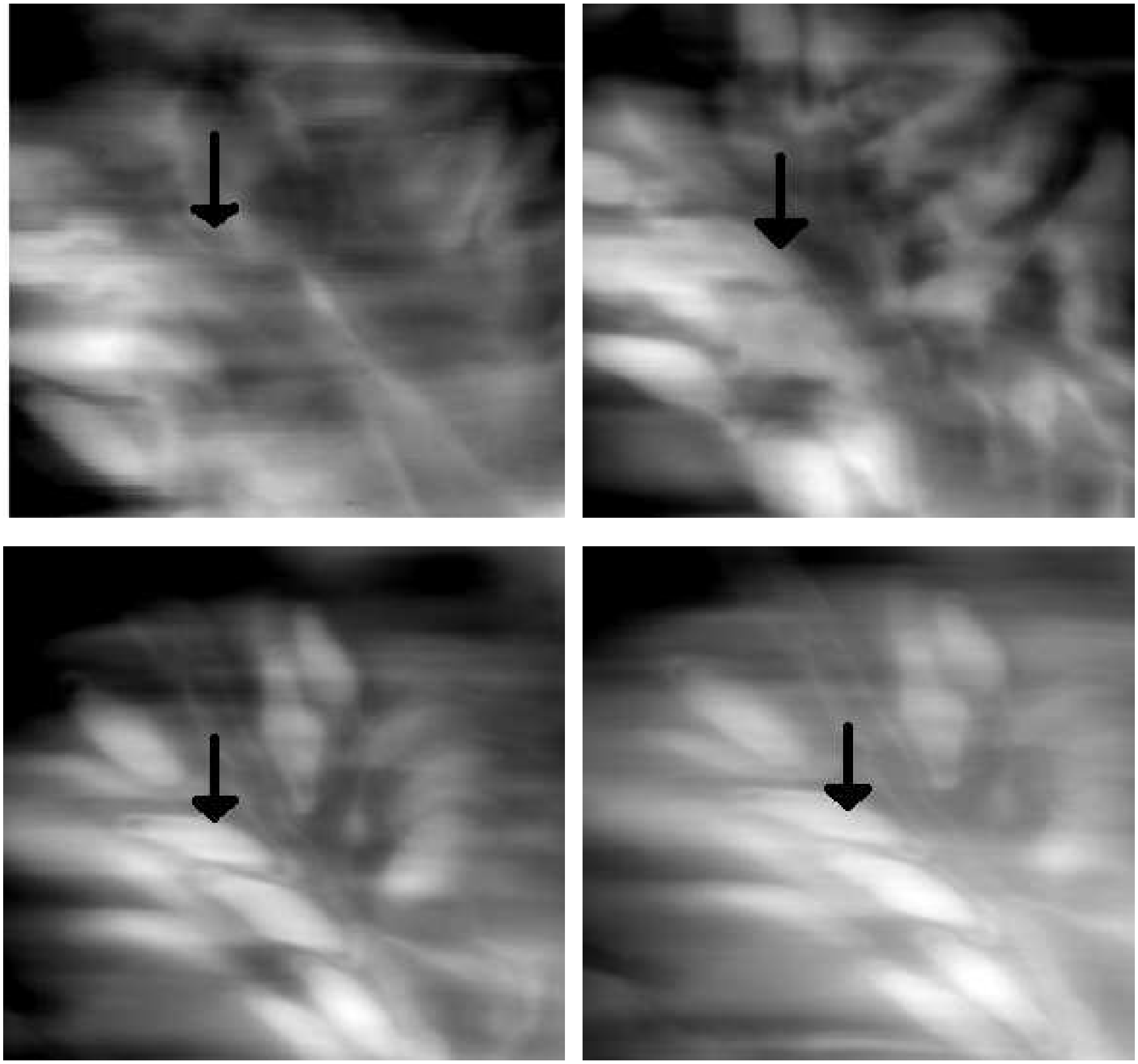

Figure 5.4: (Top Left and Top Right) Phase shift tomosynthesis reconstruction slices showing area where a seed is coming into focus (arrow). (Bottom Left) Phase shift tomosynthesis reconstruction slice with seed now in focus. (Bottom Right) Attenuation tomosynthesis reconstruction slice showing seed in focus. Note: The image blur is due to the presence of out-of-focus planes.

A (35 x 7 pixel) ROI was drawn within the same in-plane seed in both tomosynthesis reconstructions. An identical ROI was drawn in an adjacent (background) region. The CNR for both longitudinal tomographic reconstructions are given in Table 5.3.

Table 5.3: Habanero CNR Values for Attenuation and Phase Shift Tomographic Reconstruction Images.

Tomographic Reconstruction	CNR
Attenuation	15 ± 2
Phase Shift	$2\underline{0} \pm 1$

V.5 Conclusions

In an acrylic phantom, we found that the phase shift image provides an approximate factor of two increase in the CNR over the conventional attenuation radiograph. Our measurements also found that phase shift images of the polystyrene phantoms reconstructed with the APBA technique were consistent with the linearity principle. Specifically, we observed an approximate factor of two increase in the amount of phase shift when the thickness of the phantom is doubled. One possible source of uncertainty in the phase shift calculations is the use of a monochromatic wavelength in the algorithm. For the biological phantom, the improvement in the CNR was less than that found for the acrylic phantom. The reason for this is possibly due to the lower electron density of the pepper relative to that of the acrylic. This work demonstrates the feasibility of laboratory-based phase shift tomosynthesis and suggests that phase shift imaging may provide a new bio-marker that should undergo further investigation and evaluation to determine its utility for clinical applications.

V.6 Addendum

This addendum is due to a request from my doctoral committee to compare the CNR of an attenuation tomosynthesis reconstruction to that of a phase-contrast (PC) tomosynthesis reconstruction using the habanero pepper from the previous section. A (35 x 7 pixel) ROI was drawn in the same in-plane seed used in Section V.4 in the PC tomosynthesis reconstruction. An identical

ROI was drawn in an adjacent (background) region. The CNR for both longitudinal tomographic reconstructions are given in Table 5.4.

Table 5.4: Habanero CNR values for Attenuation and Phase-Contrast Tomographic Reconstruction Images

Tomographic Reconstruction	CNR
Attenuation	15 ± 2
Phase-Contrast	14 ± 1

Thus the CNR values from the attenuation and phase-contrast tomographic images are essentially equivalent. This is understandable since the phase-contrast effect is an edge enhancement effect and does not affect regions away from the edges.

Bibliography

[1] S. Wilkins, T.E. Gureyev, D. Gao, A. Pogany and A.W. Stevenson, **Phase-contrast imaging using polychromatic hard x-rays.** Nature (London) **384**, 335-338 (1996)

[2] T.J.Davis, T.E. Gureyev, D. Gao, A.W. Stevenson, and S.W. Wilkins, **X-ray image contrast from a simple phase object.**, Phys. Rev. Lett. **74**, 3173-3176 (1995)

[3] E.F.Donnelly, K.G. Lewis, K.M. Wolske, D.R. Pickens and R.R. Price, **Characterization of the phase-contrast radiography edge enhancement effect in a cabinet x-ray system.** Phys. Med. Biol. **51**, 21-30 (2006)

[4] T. Vo-Dinh (Ed.), Biomedical Photonics Handbook, CRC Press, Boca Raton, Fl. (2003)

[5] X. Wu, H. Liu, and A. Yan, **Phase-contrast X-ray tomography: Contrast mechanism and roles of phase retrieval.** Euro. Journal of Radiology **68S**, S8-S12 (2008)

[6] A. Yan, X. Wu and H. Liu, **Performance analysis of the attenuation-partition based iterative phase retrieval algorithm for in-line phase-contrast imaging.** Optics Express, Vol. **18**, No. 15, 16074-16089 (2010)

[7] J.Fineup, **Phase retrieval algorithms: a comparison.** Applied Optics **21**, 2758 - 2769 (1982)

[8] K. Nugent, T. Gureyev, D. Cookson, D. Paganin and Z. Barenea, **Quantitative phase imaging using hard x-rays.**, Phy. Rev. Lett. **77**, 2961 - 2965 (1996)

[9] L. Allen and M. Oxley, **Phase retrieval from series of images obtained by defocus variation.**, Opt. Comm. **199**, 65 - 75 (2001)

[10] A. Yan, X. Wu and H. Liu, **An attenuation-partition based iterative phase retrieval algorithm for in-line phase-contrast imaging.** Optics Express, Vol. **16**, No. 17, 13330 - 13341 (2008)

[11] A. Maksimenko, T. Yuasa, M. Ando, and E. Hashimoto, **Refraction-based tomosynthesis: Proof of the concept.** Applied Physics Letters, Vol. **91**, 234108-1 to -3 (2007)

[12] K. Kang, Z. Huang, P. Zhu, and L. Zhang, **DEI-based Phase-contrast Tomosynthetic Experiment on Biological Samples with High Resolution X-ray CCD Camera.** 2008 IEEE Nuclear Science Symposium Conference Record, 1451 - 1454

[13] K. Li, N. Bevins, J. Zambelli, G-H. Chen, *Differential phase contrast tomosynthesis imaging* Medical Imaging 2012: Physics of Medical Imaging, Proceedings of SPIE, Vol. **8313**, 83131Z-1 to -6

[14] L. Zhang, M. Jin, Z. Huang, Y. Xiao, H. Yin, Z. Wang, and T. Xiao, **Phase-contrast Tomosynthetic Experiment on Biological Samples with Synchrotron Radiation.** 2010 IEEE, 1619 - 1621

[15] N. Bevins, J. Zambelli, K. Li, Z. Qi, and G-H. Chen, **Multicontrast x-ray computed tomography imaging using Talbot-Lau interferometry without phase stepping.** Med. Phys., Vol. **39** (1), 424 - 428 (2012)

[16] W. S. Rasband, Image J, U. S. National Institutes of Health, Bethesda, Maryland, USA, $\langle http://rsb.info.nih.gov/ij/\rangle$, 1997 - 2008.

[17] J.L. Prince and J.M. Links, Medical Imaging Signals and Systems, Pearson Prentice Hall (2006)

[18] J. Hammonds, R. Price, D. Pickens, E. Donnelly, **Phase-contrast digital tomosynthesis.**, Med. Phy., Vol. **38** (5), 2353 - 2358 (2011)

Chapter VI

Summary and Future Work

VI.1 Summary

X-ray phase-contrast imaging is an imaging technique in which an image's contrast comes not only from the x-ray attenuation but also relies upon interference effects due to the differential phase shifts that the x-rays experience as they pass through different materials. An intensity variation can be created from the interference of phase-shifted x-rays that originate from within the object and the non phase-shifted x-rays from the source. This intensity variation shows both constructive and destructive interference effects occurring at the edge of the object resulting in enhanced visualization of the object's boundary or an edge enhancement effect. One portion of chapter 4 dealt with the operational parameters necessary for the production and application of phase-contrast radiography to the detection aluminum corrosion on an aluminum substrate. Chapter 3 dealt with the effect of digital tomosynthesis, which is one method of volumetric imaging, has on the edge enhancement effect and a portion of chapter 4 of this dissertation dealt with its capability of providing an approximate method of determining the depth of corrosion. As mentioned previously, as an x-ray passes through a material, its phase is changed or shifted. This x-ray phase shift has been used to produce planar x-ray phase shift images. Chapter 5 dealt with the production of a phase shift digital tomosynthesis image from a collection of planar phase shift images with the use of a conventional x-ray source. The following paragraph gives a more complete breakdown of the dissertation.

The first chapter began with a look at planar absorption radiography and its limitations. Then the introduction of planar phase-contrast radiography was made and its comparison with planar absorption radiography was shown. The physical origins of the phase-contrast edge enhancement effect are explored and the relevant experimental parameters necessary for an edge enhancement effect are discussed. The second chapter discussed the various methods of producing a planar phase-contrast radiograph and, due to the resulting superposition of an object's complex internal structure in planar radiography, a review of three-dimensional imaging was also provided. The third chapter demonstrated that digital tomosynthesis preserved the edge enhancements that are seen in planar phase-contrast radiographs and that it was possible to use a conventional x-ray source in the generation of a phase-contrast digital tomosynthesis (PC-DTS) reconstructed volumetric image. The fourth chapter provided the operational parameters essential for the production of a potential x-ray corrosion inspection system for the detection of Al_2O_3 in aircraft structures. The fifth chapter demonstrated the ability to produce phase shift volumetric images from the phase shift radiographs obtained from the attenuation-partition based algorithm (APBA) and verification that APBA obeyed the linearity or superposition principle.

VI.2 Future Work

VI.2.1 Computational Programs

Reconstruction Algorithms: Digital tomosynthesis (DTS) reconstructions are invariably influenced by tomographic noise. This tomographic noise is due to the blurring of objects that lie outside of the fulcrum plane and are superposed on the focused image. Future work in PS-DTS and PC-DTS could focus on the type of reconstruction algorithm that is used in the production of the volumetric image. This dissertation, only the multiple projection algorithm (MPA) was used in the reconstruction of digital tomosynthesis images. This algorithm is a variant of the traditional shift-and-add reconstruction method mentioned earlier. One could explore the utility of pre-processing the projection data using different filters and then applying the MPA thus creating a filtered MPA or post-processing of the reconstructed tomogram. The latter would investigate the potential of wavelet transform algorithms, applications of artifact reduction methods, the use of direct Fourier algorithms, statistical and algebraic reconstruction techniques mentioned in Chapter 2 or specialty algorithms such as matrix inversion tomosynthesis (MITS).

X-ray Corrosion Inspection System: Continuing the work on the determination of the corrosion depth using phase-contrast digital tomosynthesis, especially with the cross-section reconstruction method. It would be reasonable to assume that natural corrosion would neither be as well defined nor spatially uniform in their depth as in the engineered corrosion samples. Thus a more efficient way of corrosion depth determination needs to be developed; one such possibility includes writing a computer program to automatically search for the maximum concavity signatures.

VI.2.2 Technology

PC-DTS and PS-DTS: Currently there are no dedicated PC or PS-DTS equipment available. Thus, the construction of such equipment could be another avenue of research. In reality, only the PS-DTS system needs to be constructed since it requires both the acquisition of attenuation radiographs as well as phase-contrast radiographs. It would automatically fulfill the role of a dedicated PC-DTS system. There are basically two methods to acquire the attenuation and phase-contrast radiographs needed for a phase shift image: one method is to make two separate exposures at two separate object-to-detector distances and the other method is to simultaneous use two different detectors to make one exposure for the two separate radiographs. The former method was used in this dissertation and may serve as a prototype system to be built. The objection to this particular method comes at the potential increase of radiation dose that an object is subjected to during two separate radiograph acquisitions. Also, another objection is the increase acquisition time necessary to obtain the two separate radiographs. This could be detrimental in the imaging of living organisms. The latter method of using a dual detector system may help to alleviate both objections. However, it would require the use of a detector that has the ability to both detect some of the x-ray photons and pass enough of the remaining x-ray photons to be detected by the other detector. One method discussed in the literature is to use two photostimulable plates as the dual detectors. While this system does allow one exposure per acquisition of two separate radiographs, the time needed to change out the photostimulable plates for unexposed plates may become objectionable especially when obtaining the required attenuation and phase-contrast radiographs from a large total rotational arc.

X-ray Corrosion Inspection System: With the determination of the operational parameters, construction of an actual x-ray corrosion inspection system would be a logical next step. This inspection system would possibly take the form of a C-arm with the x-ray tube on one end and a flat panel detector on the other end. Once created, another potential area of work is to test the effect of decoupling the x-ray detector from the C-arm. This decoupling, if feasible, could open up a wider variety of objects to imaging that are too large to be imaged even with the C-arm or areas originally inaccessible to the inspection system to be imaged, such as the interior of a wing or fuselage.

VI.2.3 PS-DTS in Animal Imaging

Another avenue to explore is the potential impact of PS-DTS in small animal imaging. In the production of a planar phase shift image, the acquisition of both an attenuation radiograph and a phase-contrast radiograph has to occur. Therefore, one has three separate planar images (phase shift, phase-contrast and attenuation) of the small animal that can be viewed in a variety of ways (such as different planar 2D images or digital tomosynthesis volumetric images). This lab has done some preliminary work in this area. Using a planar phase-contrast radiograph (with a SOD = 16.8 cm and an OID = 66.2 cm) and a planar attenuation radiograph (with a SOD = 83.0 cm and an OID = 0 cm) both acquired at 34 kVp and 4.5 mAs, figure 6.1 is a planar phase shift image of a mouse thorax.

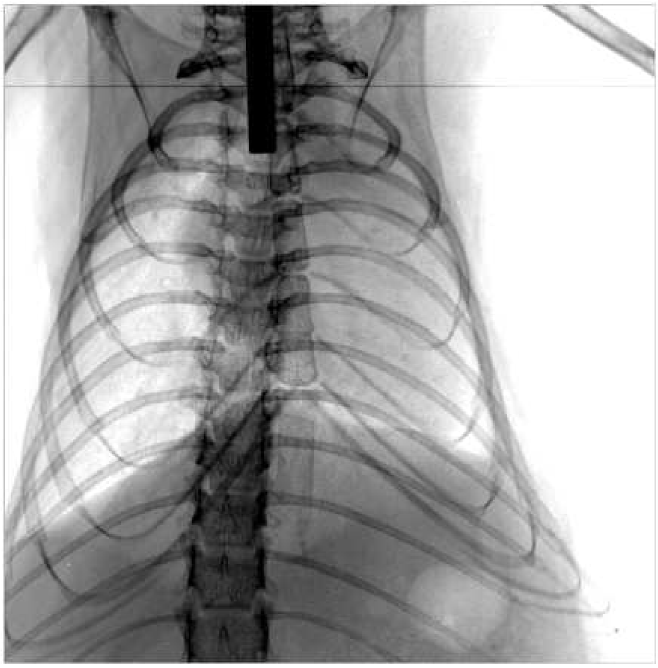

Figure 6.1: A phase shift map of a mouse thorax. Note: The dark, rectangular object at the top of the image is an endotracheal intubation needle and the horizontal line are dead pixels.

PS-DTS would reduce the superimposed patterns and boundaries that are found in the planar phase shift images and would require the use of fewer projections in the final 3D reconstruction than that used in a CT reconstruction. This last advantage would allow for faster data acquisition time and a reduction in the radiation dose delivered to the small animal.

VI.2.4 Linear Phase Shift Coefficeint

Further exploration of the results found from the linearity principle in Chapter 5 should also be investigated further. Using a planar phase-contrast radiograph (with a SOD = 75.0 cm and an OID = 75.0 cm) and a planar attenuation radiograph (with a SOD = 150.0 cm and an OID = 0 cm) both acquired at 30 kVp and 0.20 mAs using both the Wylie notched aluminum plate and a layered structure composed of x-ray film, two phase shift images of each material can be obtained. Looking at Figure 6.2, one can measure the slope from each of the two linear phase shift graphs to find a quantity analogous to the linear attenuation coefficient obtained from a graph plotting the logarithm of the ratio of transmitted x-ray intensity to initial x-ray intensity versus thickness of material at a particular x-ray energy. This quantity could be considered a linear phase shift coefficient with units of radians/cm whereas the linear attenuation coefficient has units of cm^{-1}.

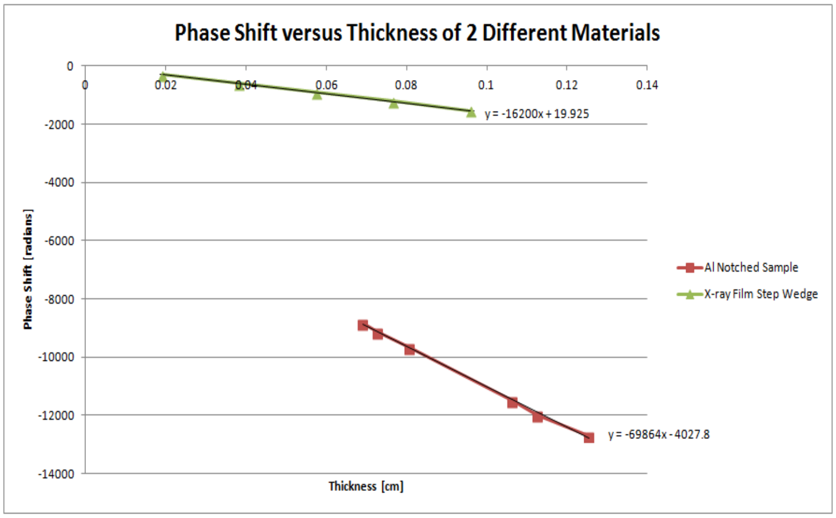

Figure 6.2: Plot of the Phase Shift of the Notched Aluminum Sample and an X-ray Step Wedge.

From this figure, it is seen that the linear phase shift coefficient for aluminum at 30 kVp is approximately -69864 radians/cm and, for the x-ray film step wedge, the linear phase shift coefficient is approximately -16200 radians/cm.

Appendix A

Photons in the diagnostic energy range (25 keV - 150 keV) have three modes for interacting with matter: coherent scatter (Rayleigh and Thomson scatter), photoelectric effect and incoherent scatter (Compton scatter). These interaction modes have the ability to decrease the number of photons exponentially by removing the photon from the incident beam.

A.1 Coherent Scatter

A.1.1 Thomson Scattering

When an incident beam of photons encounters a loosely-bound (essentially free) atomic electron, the beam sets the electron into a forced resonant oscillation due to the frequency of the incident electromagnetic wave. The motion of the electron can be described by non-relativistic physics using Newton's second law of motion, $\mathbf{F} = m\mathbf{a}$ where $\mathbf{F}$ is the Lorentz force, m is the mass of the electron and $\mathbf{a}$ is the instantaneous acceleration of the electron. Since non-relativistic physics is being used, the Lorentz force can be reduced to only the force of photon's electric field. Thus, the instantaneous acceleration of the electron that is being driven by the incident electromagnetic field is given by $\mathbf{a}\left(\mathbf{r},t\right) = -\frac{e}{m}\mathbf{E}_i\left(\mathbf{r},t\right)$ where $\mathbf{r}$ is the position in space, t is time, e is the electron charge and $\mathbf{E}_i$ is the incident electric field of the photon. As a result of this electron acceleration, there is a re-emission of the electromagnetic radiation to a different angle than that of the incident radiation. This process is generally referred to as scattering and the measure of the electron's scattering power is given by the scattering cross-section σ. This is the effective area for redirecting the incident radiation.

The cross-section is defined as the average power radiated divided by the average incident power per area, $\left|\bar{\mathbf{S}}_i\right|$:

$$\sigma = \frac{\bar{\mathbf{P}}_{scattered}}{\left|\bar{S}_i\right|} \tag{1.1}$$

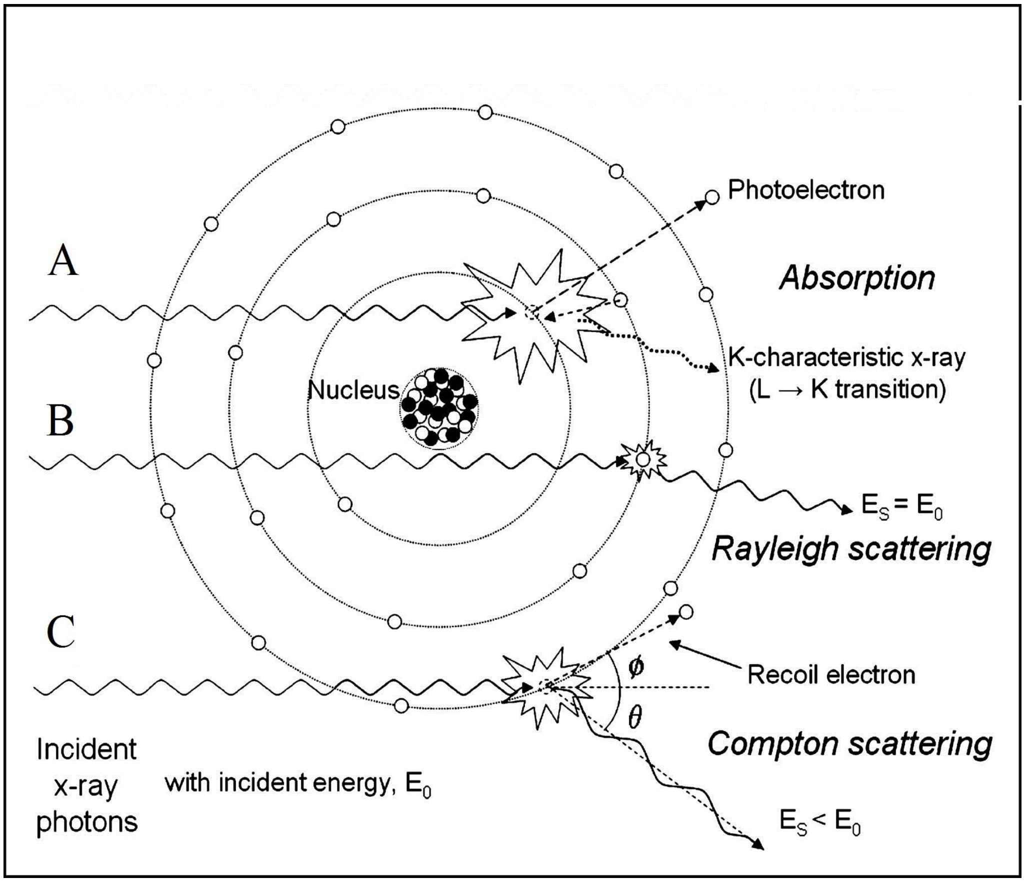

Figure A.1: Photon Interaction Modes. Adapted from [1] where $\bar{\mathbf{P}}_{scattered}$ is the average power scattered to all directions when the incident electric field $\mathbf{E}_i(\mathbf{r},t)$ excites the electron to an instantaneous acceleration $\mathbf{a}(\mathbf{r},t)$ and the average power per unit area carried by the incident electromagnetic radiation is given as

$$\bar{\mathbf{S}}_i = \frac{1}{2}\sqrt{\frac{\epsilon_0}{\mu_0}}\left|\mathbf{E}_i\right|^2 \mathbf{k}_0 \tag{1.2}$$

with ϵ_0 the permittivity of free space, μ_0 the permeability of free space and $\mathbf{k}_0$ the unit direction vector of the incident electromagnetic wave [2].

The scattering cross-section of an electron now becomes

$$\sigma = \frac{\bar{\mathbf{P}}_{scattered}}{\left|\bar{S}_i\right|} = \frac{\frac{4\pi}{3}\left(\frac{e^4\left|\mathbf{E}_i\right|^2}{16\pi^2\epsilon_0 m^2 c^3}\right)}{\frac{1}{2}\sqrt{\frac{\epsilon_0}{\mu_0}}\left|\mathbf{E}_i\right|^2} \tag{1.3}$$

where c is the speed of light in a vacuum. Simplifying the equation and defining $r_e = \frac{e^2}{4\pi\epsilon_0 mc^2}$ as the classical electron radius, one obtains the expression

$$\sigma_e = \frac{8\pi}{3}r_e^2 = 6.65 \ x \ 10^{-25} \ \mathrm{cm}^2. \tag{1.4}$$

where the subscript e represents the the fact that this is the cross-section scattering due to a single electron. Notice that this result is energy-independent so that it has the same value for all incident photon energies and predicts no change in the energy of the scattered electromagnetic radiation.

In addition to the cross-section, a differential scattering cross-section per unit solid angle may be defined as

$$\frac{d\sigma_e}{d\Omega} = \frac{1}{\left|\bar{S}_i\right|}\frac{d\bar{P}}{d\Omega} = \frac{r_e^2}{2}\left(1+\cos^2\theta\right) \tag{1.5}$$

where θ is the scattering angle between the incident photon direction and the scattered photon direction. The equation to obtain the fraction of radiation scattered into a cone contained between θ and $\theta + d\theta$ is given as [3]:

$$\frac{d\sigma_e}{d\theta} = \frac{d\sigma_e}{d\Omega}\frac{d\Omega}{d\theta} = 2\pi\sin\theta\frac{d\sigma_e}{d\Omega} = \pi r_e^2\sin\theta\left(1+\cos^2\theta\right). \tag{1.6}$$

A.1.2 Rayleigh Scattering

In Rayleigh scattering, an incoming photon beam sets the bound atomic electrons into a forced oscillation due to the frequency of the incident electromagnetic field. The atomic electrons are neither excited or ionized and afterward, the electrons return back to their original state since no energy was transferred. All atomic electrons contribute to Rayleigh scattering as opposed to one electron in the Thomson scattering scenario. The photon scattered at an angle θ has the same energy as the incident photon (see B in Figure A.1). The angular spread due to Rayleigh scattering depends upon both the photon energy and the atomic number Z of the scattering material and can be estimated from the equation:

$$\theta_R \approx 2\sin^{-1}\left(\frac{0.026Z^{1/3}}{E}\right) \tag{1.7}$$

where E is the normalized energy of the photon: $E = \frac{E_\gamma}{m_e c^2}$ with E_γ is the photon energy and $m_e c^2$ is the rest mass energy of the electron. θ_R represents the opening half-angle of a cone that contains 75% of the Rayleigh scattered photons [3]. There are listed in Table A.1 several θ_R at different keV for some biologically relevant elements (note: Ca does not have an angular spread for 30 keV). This table shows that, for a given element, the photons are increasingly scattered in the forward direction as the incident photon energy is increased.

Table A.1: θ_R (in degrees) for Various Elements and Incident Photon Energies.

Element	Z	30 keV	40 keV	50 keV	60 keV	70 keV	80 keV
H	1	53	39	31	26	22	19
C	6	107	74	58	47	40	35
N	7	116	79	61	50	43	37
O	8	125	83	64	53	45	39
Ca	20	N.A.N.	129	92	74	62	54

The differential Rayleigh cross-section per unit solid angle can be written as

$$\frac{d\sigma_R}{d\Omega} = \frac{d\sigma_e}{d\Omega}\left\{F\left(x,Z\right)\right\}^2 = \frac{r_e^2}{2}\left(1+\cos^2\theta\right)\left\{F\left(x,Z\right)\right\}^2 \tag{1.8}$$

where $F\left(x,Z\right)$ is the atomic form factor for Rayleigh scattering with $x = \frac{sin\frac{\theta}{2}}{\lambda}$ as the momentum transfer variable defined using the incident photon wavelength λ and the other variables defined earlier. Likewise, the Rayleigh differential cross-section per unit scattering angle can be found to be [4]

$$\frac{d\sigma_R}{d\theta} = \frac{d\sigma_R}{d\Omega}\frac{d\Omega}{d\theta} = \pi r_e^2 \sin\theta\left(1+\cos^2\theta\right)\left\{F\left(x,Z\right)\right\}^2. \tag{1.9}$$

The Rayleigh cross-section can be calculated from this by integrating over all possible scattering angles as

$$\sigma_R = \pi r_e^2 \int_0^\pi \sin\theta \left(1 + \cos^2\theta\right) \left\{F\left(x, Z\right)\right\}^2 d\theta. \tag{1.10}$$

The atomic form factor $F\left(x, Z\right)$ represents a Fourier transform of the electronic charge density distribution of the atom. Calculations of $F\left(x, Z\right)$ are difficult and can only be analytically done for the hydrogen atom. For other atoms, the atomic form factors are approximated using the Hartree, Hartree-Fock, or Thomas-Fermi models. For small scattering angles, the atomic form factor is equal to Z and for large scattering angles, it approaches 0.

A.2 Incoherent Scattering

Another scenario in which a photon interacts with a loosely-bound electron is called Compton scattering. In Compton scattering, a photon of energy $h\nu$ interacts with a stationary electron in such a way as to produce another photon of lower energy $h\nu'$ and a recoil electron (see C in Figure A.1). Thus, unlike coherent scattering, the photon loses energy in the interaction and this interaction is referred to as incoherent scattering. By using relativistic relationships for the conservation of energy and momentum, Arthur Compton derived the wavelength shift experienced by the photon during the interaction [6]:

$$\Delta\lambda = \lambda_1 - \lambda_0 = \frac{h}{m_e c}\left(1 - \cos\theta\right) = \lambda_C \left(1 - \cos\theta\right) \tag{1.11}$$

where λ_0 is the wavelength of the incident photon, λ_1 is the wavelength of the scattered photon, θ is the photon scatter angle, h is Planck's constant, m_e is the mass of the electron and c is the speed of light. The last three variables form what is called the Compton wavelength, λ_C. Sometimes, the wavelength shift can be written as

$$\frac{1}{\lambda_0}\frac{1}{\lambda_1}\cos\theta = \frac{1}{\lambda_0}\frac{1}{\lambda_1} - \frac{m_e c}{h}\left[\frac{1}{\lambda_0} - \frac{1}{\lambda_1}\right] \tag{1.12}$$

where the variables have been previously defined. Either way, the change in the wavelength of the photon is governed by the scattering angle θ and not the incident photon energy.

Using conservation of momentum, it is also possible to find three equivalent relationships between the scattering angle of the photon and the recoil angle of the electron [6]:

$$\cot\phi = (1+E)\tan\frac{\theta}{2} \tag{1.13}$$

$$\tan\phi = \frac{\cot\frac{\theta}{2}}{1+E} \tag{1.14}$$

$$\cot\frac{\theta}{2} = (1+E)\tan\phi \tag{1.15}$$

where ϕ is the recoil angle of the electron, θ is the scattering angle of the photon and E is the normalized energy of the photon: $E = \frac{E_\gamma}{m_e c^2}$ with E_γ is the incident photon energy and $m_e c^2$ is the rest mass energy of the electron. Thus, for a given θ, the higher the incident photon energy or E then the smaller the recoil angle ϕ will be. These relationships also show that the electron recoil angle ϕ is limited to the values $0 \leq \phi \leq \frac{\pi}{2}$ while the photon scatter angle ranges from $0 \leq \theta \leq \pi$. Thus the electron is confined to the forward hemisphere while the scattered photon may experience backscatter.

Additional relationships can be found that relate the scattered photon energy as a function of incident photon energy and photon scattering angle θ or electron recoil angle ϕ [6]:

$$h\nu_1 = h\nu_0 \frac{1}{1+2E\sin^2\frac{\theta}{2}} \tag{1.16}$$

$$h\nu_1 = h\nu_0 \frac{(1+E)^2 - E(E+2)\cos^2\phi}{(1+E)^2 - E^2\cos^2\phi} \tag{1.17}$$

where ν_1 and ν_0 are the frequencies of the scattered and incident photons respectively and the combination of $h\nu_1$ and $h\nu_0$ represent the energies of the scattered and incident photons respectively. Table A.2 shows the scattered photon energy as a result of certain values of θ and the corresponding ϕ values as well as the saturation limit of the scattered photon energy as the incident photon energy goes to infinity, i.e. $h\nu_0 \rightarrow \infty$ [3].

Table A.2: Scattered and Saturation Photon Energy for Specific Cases of θ and ϕ

θ	ϕ	hν_1	h$\nu_{\text{sat.}}$
0	$\frac{\pi}{2}$	hν_0	hν_∞
$\frac{\pi}{2}$	$\cot^{-1}(1+E)$	$\frac{h\nu_0}{1+E}$	511 keV
π	0	$\frac{h\nu_0}{1+2E}$	255 keV

When $\theta = 0$, the scattered photon energy is identical to the incident photon energy so that no energy is imparted to the electron. The second and third entries show that for photons scattered between $\frac{\pi}{2}$ and π, the energy can not exceed 511 keV no matter how large the incident photon energy was. From $\theta = \pi$, the backscattered photon energy will never be larger than 255 keV regardless of the magnitude of the incident photon energy.

The differential cross-section per unit solid angle for the Compton interaction between a photon and a free electron was derived by Oskar Klein and Yoshio Nishina. It is given by the formula [3]

$$\frac{d\sigma_C}{d\Omega} = \frac{r_e^2}{2}\left(\frac{\nu_1}{\nu_0}\right)^2\left\{\frac{\nu_1}{\nu_0} + \frac{\nu_0}{\nu_1} - \sin^2\theta\right\} = \frac{r_e^2}{2}\left(1+\cos^2\theta\right)F_{KN} = \frac{d\sigma_e}{d\Omega}F_{KN} \tag{1.18}$$

where F_{KN} is the Klein-Nishina form factor for a free electron and is given by

$$F_{KN}\left(E,\theta\right) = \frac{1}{\left[1+E\left(1-\cos\theta\right)\right]^2}\left\{1 + \frac{E^2\left(1-\cos\theta\right)^2}{\left[1+E\left(1-\cos\theta\right)\right]\left(1+\cos^2\theta\right)}\right\} \tag{1.19}$$

with all other terms being previously defined. Although the Klein-Nishina is a complicated function, it is easy to see that when $F_{KN} = 1$, then the $\frac{d\sigma_C}{d\Omega} = \frac{d\sigma_e}{d\Omega}$ or the differential Compton cross-section equals the differential Thomson cross-section. Also, when $\theta = 0$, then $F_{KN} = 1$ for any E and in general, for any θ and E, $F_{KN} \leq 1$.

It is also possible to derive the differential Compton cross-section per unit scattering angle from equation (1.18).

$$\frac{d\sigma_C}{d\theta} = \frac{d\sigma_C}{d\Omega}\frac{d\Omega}{d\theta} = \pi r_e^2 F_{KN}\left(1+\cos\theta\right)\sin\theta \tag{1.20}$$

where $d\Omega = 2\pi\sin\theta d\theta$. Also, it is possible to derive the differential Compton cross-section per unit recoil angle using equation (1.18) and equations (1.13) through (1.15):

$$\frac{d\sigma_C}{d\phi} = \frac{d\sigma_C}{d\theta}\frac{d\theta}{d\phi} = 2\pi r_e^2 F_{KN}\frac{\left(1+\cos^2\theta\right)\sin\theta\cos^2\frac{\theta}{2}}{\left(1+E\right)\sin^2\phi} \tag{1.21}$$

$$\text{or} \tag{1.22}$$

$$\frac{d\sigma_C}{d\phi} = \frac{d\sigma_C}{d\theta}\frac{d\theta}{d\phi} = 2\pi r_e^2 F_{KN}\frac{\left(1+E\right)\left(1+\cos^2\theta\right)\sin\theta\sin^2\frac{\theta}{2}}{\cos^2\phi} \tag{1.23}$$

Integration of equation (1.18) over the whole solid angle leads to the Klein-Nishina cross-section for Compton scatter and is given as:

$$\sigma_C = \int\frac{d\sigma_C}{d\Omega}d\Omega = 2\pi r_e^2\left\{\frac{1+E}{E^2}\left[\frac{2\left(1+E\right)}{1+2E} - \frac{\ln\left(1+2E\right)}{E}\right] + \frac{\ln\left(1+2E\right)}{2E} - \frac{1+3E}{\left(1+2E\right)^2}\right\} \tag{1.24}$$

where all variables have been previously defined. From this complicated expression, one can see that the Klein-Nishina cross-section for Compton scatter is independent of the atomic number Z which follows from the fact that the initial assumption that Compton made involved a loosely bound orbital electron whose binding energy was negligible to that of the incident photon energy.

A.3 Photoelectric Effect

When a photon interacts with a tightly bound orbital electron, there is the possibility of the photoelectric effect occurring. Usually, in the photoelectric and Compton effect, the photon energy is completely absorbed and the orbital electron is ejected from the atom and is now called a photoelectron (see A in Figure A.1). The kinetic energy E_K of the photoelectron is assumed to be equal to the incident photon energy E_γ minus the binding energy E_B of the orbital shell:

$$E_K = E_\gamma - E_B. \tag{1.25}$$

However, if the photon energy is not sufficient to eject an electron from the atom, then it may be sufficient to raise the electron to a higher energy level in a process called excitation.

All atomic electrons are available for the photoelectric effect to occur; however, the most tightly bound electron has the greatest probability for interaction with the photon. Thus, a photon with an energy exceeding the K-shell binding energy is most likely to interact with the K-shell electrons; a photon with an energy between the K-shell and L-shell binding energies will most likely interact with the L-shell electrons, and so on.The vacancy left behind by the ejected electron will be filled by an electron from a higher orbital shell. This process causes another vacancy to occur in that higher orbital shell until it is filled by an electron from yet a higher orbital shell and this continues until the vacancy reaches the outer shell of the atom and is finally filled by a free electron that neutralizes the ion. This process of filling the vacancy releases energy during the electron transitions that may result in

1. a characteristic x-ray
2. an Auger electron
3. or, most likely, some combination of both

being released from the atom during the electronic transitions.

The probability of a photoelectric effect occurring is approximately proportional to $\frac{Z^3}{E_\gamma^3}$ where Z is the atomic number and E_γ is the photon energy. The photoelectric effect predominates when the lower energy photons interact with high Z materials and is the primary mode of interaction of diagnostic x-rays with image receptors, contrast agents and radiation shielding. It is also beneficial in x-ray imaging since there are no scattered x-rays to degrade the resultant image. For photon energies below 50 keV, the photoelectric effect can be used to exploit differences between tissues that have slightly different atomic numbers [5].

Bibliography

[1] http://tech.snmjournals.org/content/33/1/3/F1.large.jpg

[2] David Attwood, *Soft X-rays and Extreme Ultraviolet Radiation*, Cambridge University Press (1999)

[3] Ervin P. Podgorsak, *Radiation Physics for Medical Physicists 2nd Edition*, Springer-Verlag, Berlin (2010)

[4] Harold Elford Johns and John Robert Cunningham, *The Physics of Radiology 4th Edition*, Charles C Thomas Publisher (1983)

[5] Jerrold T. Bushberg, J. Anthony Seibert, Edwin M. Leidholdt Jr., John M. Boone, *The Essential Physics of Medical Imaging 3rd Edition*, Lippincott Williams and Wilkins (2012)

[6] Robert Eisberg and Robert Resnick, *Quantum Physics of Atoms, Molecules, Solids, Nuclei, and Particles 2nd Edition*, John Wiley and Sons, Inc (1985)

Appendix B

B.1 SMAM II Mammography Detector

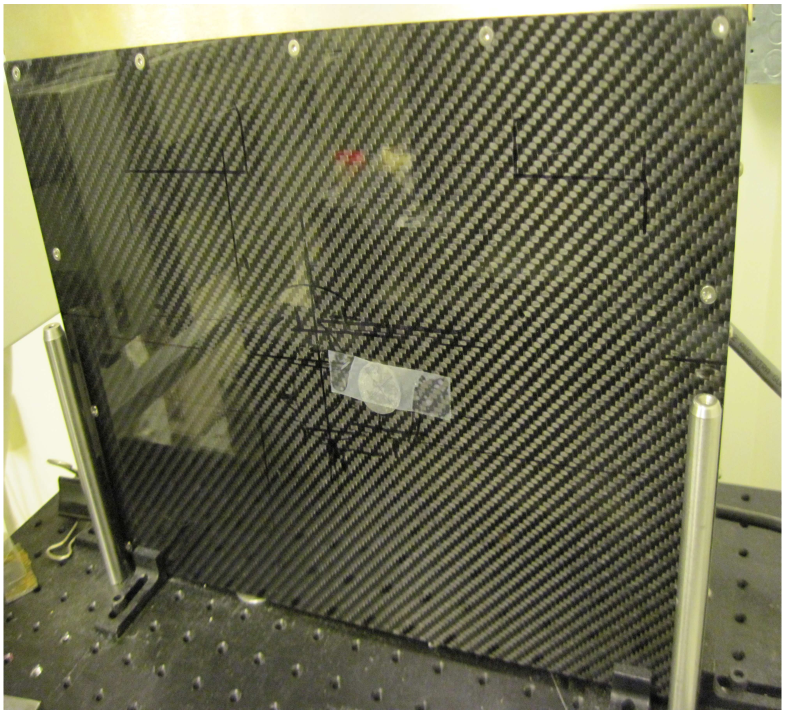

Figure B.1: SMAM II Mammography Detector. Note: A lead beam stop is attached to the detector.

Table B.1: SMAM II Mammography Characteristics

Detector Technology	Amorphous selenium over thin-film transistor panel
Active Area	171.36 mm x 239.36 mm
Detector Element Array	2016 x 2816 pixels
Detector Element Size	85 μm x 85 μm
Detector Element Fill Factor	70% geometric
Panel Read Time	<1.4 seconds for full 13-bit resolution
Minimum Time Between X-ray Images	30 seconds

B.2 Tru-Focus X-ray System

Table B.2: Tru-Focus Characteristics

Target Voltage	20 - 125 kVp
Target Material	Tungsten
Maximum Target Current	2.5 mA
Maximum Power (Small Focal Spot)	10 W
Maximum Power (Large Focal Spot)	60 W
Small Focal Spot Size	<10 μm
Large Focal Spot Size	$\leq$50 μm
Beam Angle	45°
Window Material	Beryllium
Window Thickness	0.010 inches
Window Type	End Window

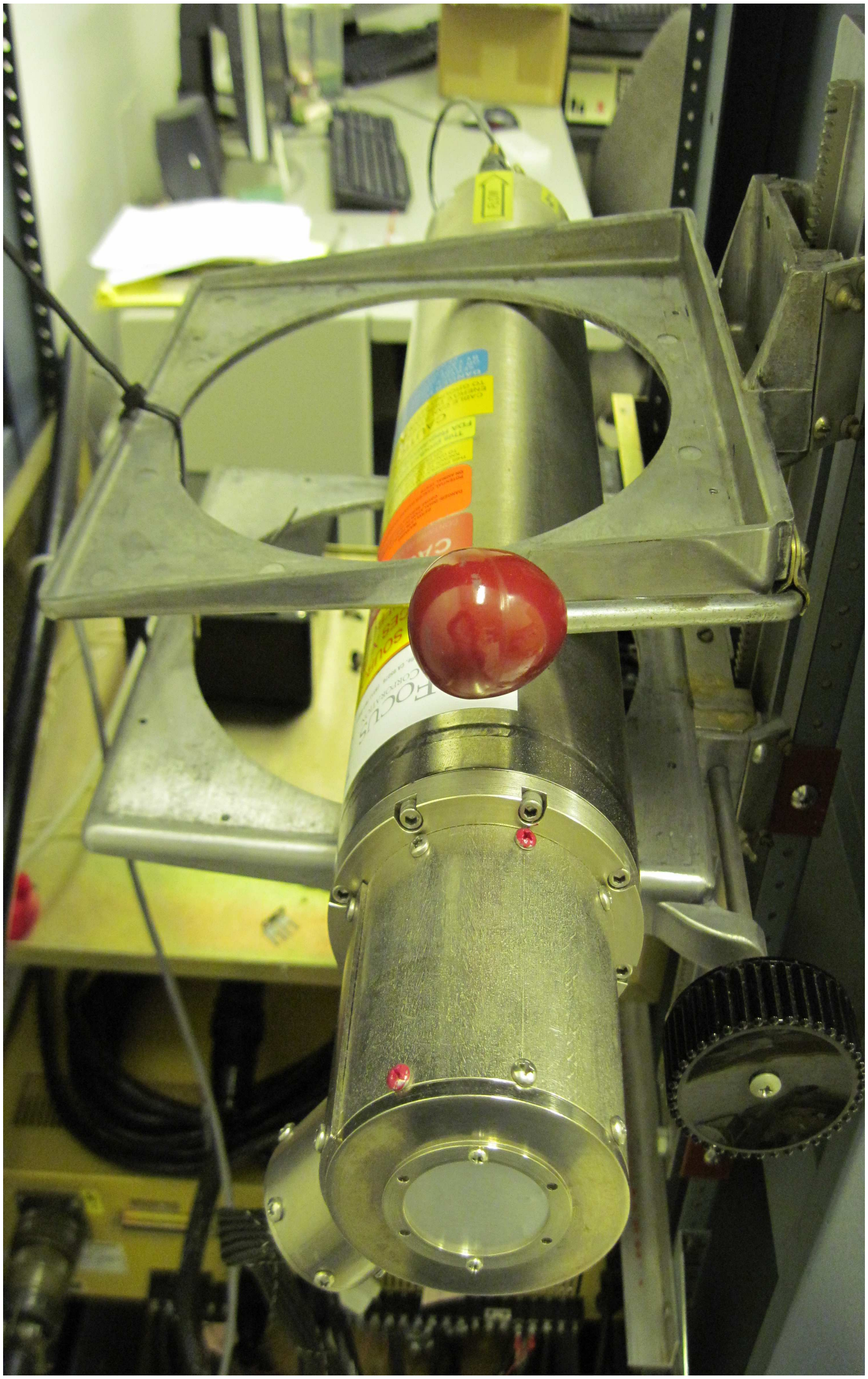

Figure B.2: Tru-Focus X-ray Unit

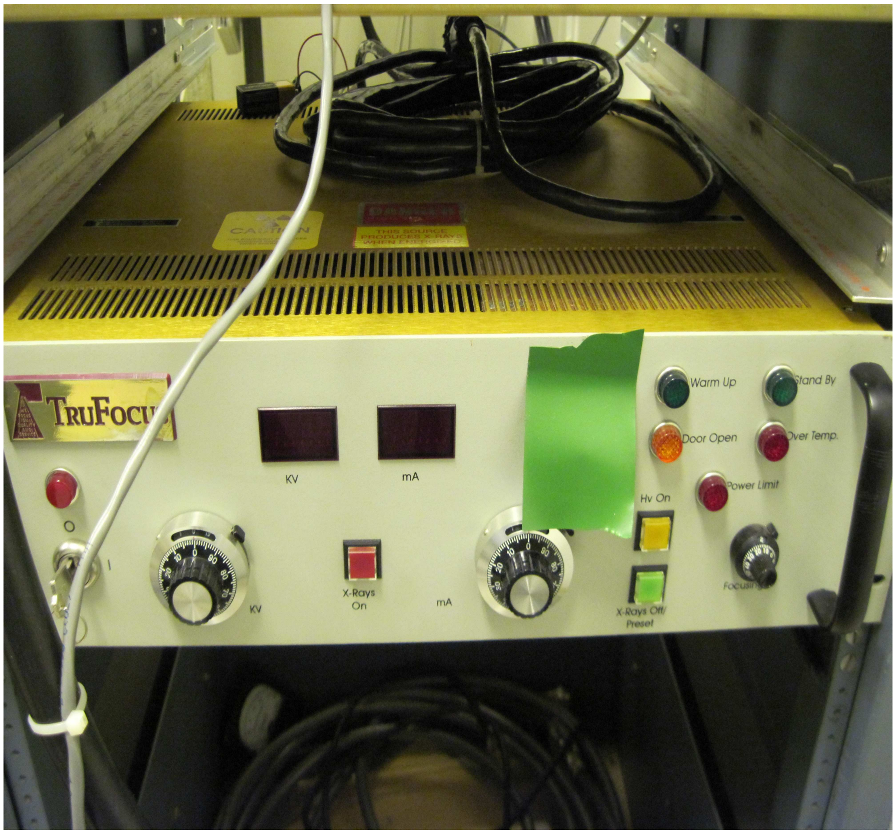

Figure B.3: Tru-Focus X-ray Control Unit. Green tape protects the focal spot switch.

B.3 Faxitron LX-60 X-ray System

Figure B.4: Faxitron LX-60 with x-ray detector at shelf position 1.5.

Table B.3: Faxitron X-ray Characteristics

Focal Spot Size	<0.02 mm
kVp	10 - 60
mA	0.3 from 10 kVp to 40 kVp
Beryllium Window Thickness	0.25 mm
X-ray Beam Divergence	40 °
Target Material	Tungsten

Note: From 40 kVp to 60 kVp, the tube current varies but is iso-watt limited to 12 watts.

Table B.4: Shelf Position and Corresponding Source-to-Object Distance

6	14.0 cm
5	16.8 cm
4	21.0 cm
3	27.8 cm
2	41.7 cm
1.5	55.4 cm
1 (bottom)	83.0 cm

Table B.5: Hamamatsu Detector Characteristics

Detector Technology	CsI/CMOS
Active Area	117.00 mm x 118.40 mm
Detector Element Array	2340 x 2368 pixels
Detector Element Size	50 μm x 50 μm

Appendix C

C.1 Attenuation-Partition Based Algorithm (APBA)

The APBA operates as follows (see Figure C.1).

1. We write the attenuated x-ray amplitude as $A_0(\mathbf{r}) = A_{incoherent}(\mathbf{r}) \cdot A_{pe,coh}(\mathbf{r}) = \tilde{A}(\mathbf{r}) - \delta A(\mathbf{r})$ where $\tilde{A}(\mathbf{r}) = A_{KN}(\mathbf{r}) = A_{incoherent}(\mathbf{r})$ and $\delta A(\mathbf{r}) = A_{KN}(\mathbf{r})(1 - A_{pe,coh}(\mathbf{r}))$.
2. Regard the experimentally acquired phase-contrast image I as if it receives all of its intensity contributions only from Compton scatter. In other words, the amplitude of the phase-contrast image, $\sqrt{I}$, is contributed all from $\tilde{A}(\mathbf{r}) = A_{KN}(\mathbf{r})$.
3. The phase-attenuation duality occurs when both the x-ray's attenuation and phase-shift are determined by the object's electron density. Assuming that the phase-attenuation duality holds, then a duality reversion formula relating the phase-contrast image I and the Compton attenuation map $A_{KN}^2(\mathbf{r})$ can be found:

$$A_{KN}^2(\mathbf{r}) = FT^{-1}\left(\frac{FT\left(\frac{M^2}{I_{in}} I\right)}{1 + 4\pi^2 k \mathbf{u}^2}\right) \tag{3.1}$$

and the Compton attenuation map is related to the phase shift by the equation:

$$A_{KN}^2(\mathbf{r}) = \exp\left(-\int \mu_{KN}(\mathbf{r}, s)\, ds\right) = \exp\left[\frac{\sigma_{KN}}{\lambda r_e}\phi(\mathbf{r})\right]. \tag{3.2}$$

Thus, the approximated phase-map of the object can be solved from equation (3.2):

$$\phi(\mathbf{r}) = \frac{\lambda r_e}{\sigma_{KN}} \ln\left(\tilde{A}^2(\mathbf{r})\right) \tag{3.3}$$

4. The error in the estimation of the object's attenuation map can be computed using the experimentally acquired amplitude image A_0 and is found by

$$\delta A = \tilde{A}\left(\mathbf{r}\right) - A_0 \tag{3.4}$$

5. To improve the estimate on $A^2_{KN}\left(\mathbf{r}\right)$, incorporate the error δA by considering a hypothetical object $\delta T_0\left(\mathbf{r}\right) = \delta A\left(\mathbf{r}\right) \cdot \exp\left(i\phi\left(\mathbf{r}\right)\right)$ and then compute the intensity of the transmitted x-ray wave arriving at the detector. The intensity of this virtual object is given by:

$$\delta I = \left|E_1\right|^2 \tag{3.5}$$

   where $E_1 = \frac{\exp\left[\frac{i\mathbf{r}^2}{2\omega}\right] * \delta T_0}{2\pi\omega}$ and $*$ is the convolution operator.

6. Once computed, replace I in equation (3.1) with $\left[\sqrt{I} + \sqrt{\delta I}\right]^2$ and cycle through 10 iterations.

C.2 Attenuation-Partition Based Algorithm (APBA) Flowchart

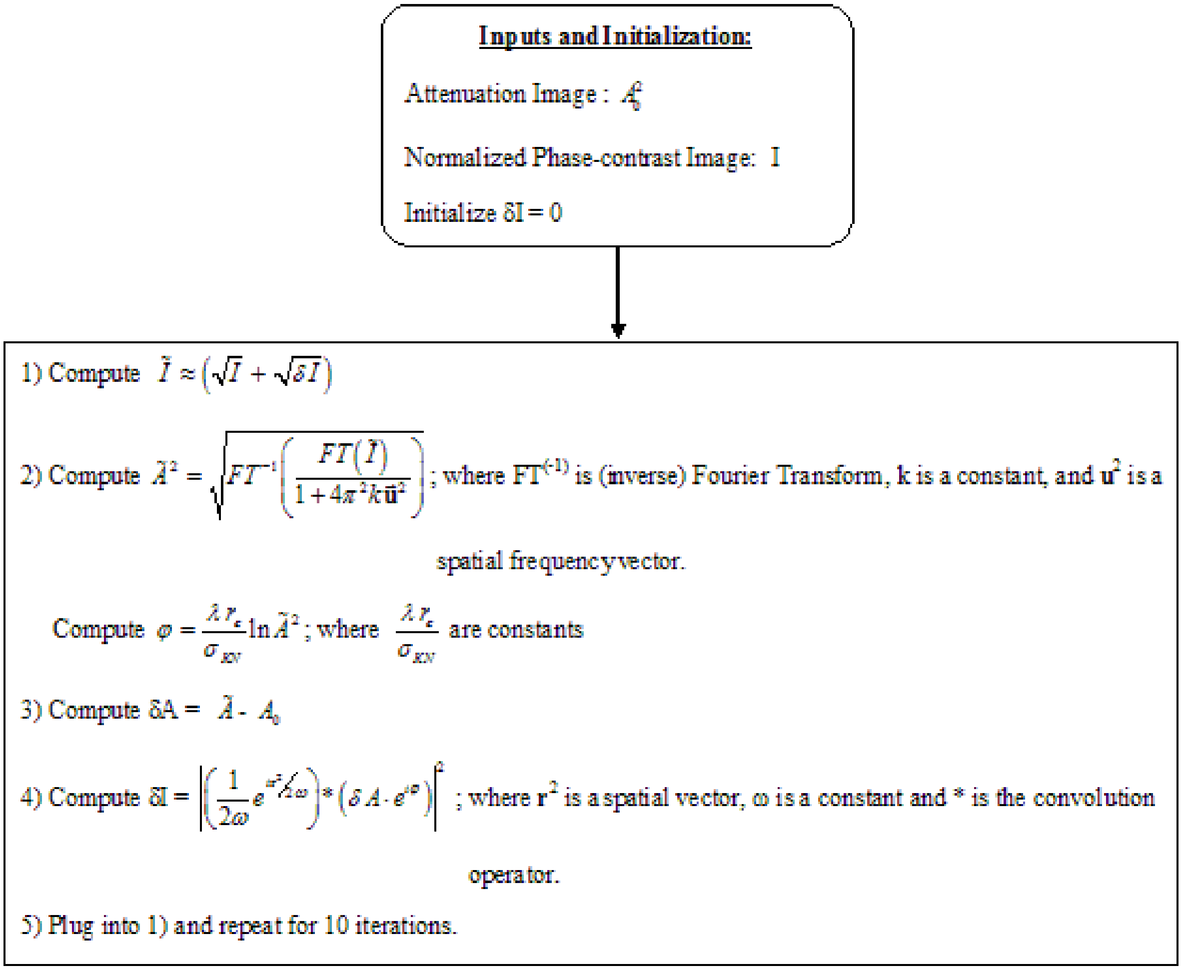

Inputs and Initialization:

Attenuation Image : A_0^2

Normalized Phase-contrast Image: I

Initialize δI = 0

1) Compute $\tilde{I} \approx \left(\sqrt{I} + \sqrt{\delta I}\right)$

2) Compute $\tilde{A}^2 = \sqrt{FT^{-1}\left(\frac{FT(\tilde{I})}{1+4\pi^2 k \vec{u}^2}\right)}$; where $FT^{(-1)}$ is (inverse) Fourier Transform, k is a constant, and $\mathbf{u}^2$ is a spatial frequency vector.

Compute $\varphi = \frac{\lambda r_e}{\sigma_{KN}} \ln \tilde{A}^2$; where $\frac{\lambda r_e}{\sigma_{KN}}$ are constants

3) Compute δA = $\tilde{A}$ - A_0

4) Compute δI = $\left|\left(\frac{1}{2\omega} e^{r^2/2\omega}\right) * \left(\delta A \cdot e^{i\varphi}\right)\right|^2$; where $\mathbf{r}^2$ is a spatial vector, ω is a constant and * is the convolution operator.

5) Plug into 1) and repeat for 10 iterations.

Figure C.1: Attenuation-Partition Based Algorithm (APBA) Flowchart

C.3 MATLAB Code for Attenuation-Partition Based Algorithm (APBA)

The Attenuation-Partition Based Algorithm (APBA) coded in MATLAB R2007a Student Version.

```
%%%%%%%%%%%%%%%%%%%%%%%%%%%%%%%%%%%%%%%%%%%%%%%%%%%%%%%%%%%%%%%%%%%%%%%%%%%%%%%%%%%
%
%Starts the phase mapping program
%
%%%%%%%%%%%%%%%%%%%%%%%%%%%%%%%%%%%%%%%%%%%%%%%%%%%%%%%%%%%%%%%%%%%%%%%%%%%%%%%%%%%
experimental_attenuation = imread('filename_attenuation_image');
Total0 = imread('filename_phase-contrast_image');
experimental_attenuation = double(experimental_attenuation(1:2340,29:2368));
Total0 = double(Total0(1:2340,29:2368));
%Linear Interpolation --Default in MATLAB
[r, c] = size(double(experimental_attenuation));
Inverse_Mag = 1/1.46;            %Spacing in the interpolation procedure.
for i = 1:r
   x = 1:r;
   y = double(experimental_attenuation(i,:));
   xi = 1:Inverse_Mag:r;
   yi(i,:) = interp1(x,y,xi);
end
trial = yi';
[r1, c1] = size(trial);
for i = 1:r1
   x1 = 1:c1;
   y1 = trial(i,:);
   xi1 = 1:Inverse_Mag:c1;
   yi1(i,:) = interp1(x1,y1,xi1);
end
clear i;
final = double(yi1');
[r2,c2] = size(final);
Total = zeros(r2,c2);
Total(577:2916,531:2870)=Total0;
%%%%%%%%%%%%%%%%%%%%%%%%%%%%%%%%%%%%%%%%%%%%%%%%%%%%%%%%%%%%%%%%%%%%%%%%%%%%%%%%%%%
%
%These are the cropped images 2048 x 2048
%
%%%%%%%%%%%%%%%%%%%%%%%%%%%%%%%%%%%%%%%%%%%%%%%%%%%%%%%%%%%%%%%%%%%%%%%%%%%%%%%%%%%
Total = double(Total(797:2844,755:2802));                          %PC Image
A0 = sqrt(final(797:2844,745:2792));    %Experimental Attenuation Amplitude
clear experimental_attenuation Total0 r r1 r2 c c1 c2 Inverse_Mag;
clear final I final1 I1 x x1 xi xi1 y y1 yi yi1 trial;
%%%%%%%%%%%%%%%%%%%%%%%%%%%%%%%%%%%%%%%%%%%%%%%%%%%%%%%%%%%%%%%%%%%%%%%%%%%%%%%%%%%
%
%Initialization values for the APBA
%Note: Any physical distances should be divided by 0.0050 cm/pix to convert
%      to pixels
%
%%%%%%%%%%%%%%%%%%%%%%%%%%%%%%%%%%%%%%%%%%%%%%%%%%%%%%%%%%%%%%%%%%%%%%%%%%%%%%%%%%%
delta_A_old = double(0);
```

```
delta_I = double(0);
error = double(0);
r_e = double(2.8179402894*10^(-15)*100/0.005);%Radius of electron [pixels].
E = double(20);                              %This is the energy of the photons [keV].
eta = double(E/511);
%Equation 11 (Klein-Nishina equation)
sigma = double(2*pi*r_e*r_e*((1+eta)/(eta^2)*(2*(1+eta)/(1+2*eta)-(1/eta)
        *log(1+2*eta))+(1/2*eta)*log(1+2*eta)-(1+3*eta)/((1+2*eta)^2)));
lambda1 = double(((1240/(E*1000))/(1*10^9))*100);      %The wavelength [cm].
lambda = double(lambda1/0.005);                 %This is the wavelength [pixels].
[Row, Column] = size(A0);
R1 = double(20.47/0.005);                           %This is in units of pixels.
z = double((41.7/0.0050)- R1);                      %This is in units of pixels.
I0 = sum(sum(Total(300:600,100:200)))/((size(Total(300:600,100:200),1)
     *size(Total(300:600,100:200),2))); %
n = 1;
while (n <= 10)
    %%%%%%%%%%%%%%%%%%%%%%%%%%%%%%%%%%%%%%%%%%%%%%%%%%%%%%%%%%%%%%%%%%%%%
    %
    %Part 1 of the algorithm
    %
    %%%%%%%%%%%%%%%%%%%%%%%%%%%%%%%%%%%%%%%%%%%%%%%%%%%%%%%%%%%%%%%%%%%%%
    M = 1.46;                                                %Magnification
    I = double(Total)/I0;                             %Normalized intensity
    I_tilde = double((sqrt(I) + sqrt(delta_I)).^2);             %Equation 19
    %%%%%%%%%%%%%%%%%%%%%%%%%%%%%%%%%%%%%%%%%%%%%%%%%%%%%%%%%%%%%%%%%%%%%
    %
    %Part 2 of the algorithm
    %
    %%%%%%%%%%%%%%%%%%%%%%%%%%%%%%%%%%%%%%%%%%%%%%%%%%%%%%%%%%%%%%%%%%%%%
    k = double(((lambda^2)*z*r_e)/(2*pi*M*sigma));              %Equation 13
    B2 = ((2^nextpow2(Row) - length(I_tilde(:,1)))/2);
    C2 = ((2^nextpow2(Row) - length(I_tilde(:,1)))/2);
    I_tilde2 = double(padarray(I_tilde,[B2 C2]));
    i_tilde2 = double(fftshift(fft2(I_tilde)));
    num = double(i_tilde2);               %The numerator of the Equation 12
    %%%%%%%%%%%%%%%%%%%%%%%%%%%%%%%%%%%%%%%%%%%%%%%%%%%%%%%%%%%%%%%%%%%%%
    center = (2^nextpow2(Row))/2;

    for k1 = 1:(2^nextpow2(Row));
        for l = 1:(2^nextpow2(Row));
         u_squared(k1,l) = double(((k1-center)^2
                          +(l-center)^2)/((2*(Row))^2));
        end
    end

    den = double(1 + 4*(pi^2)*k*(u_squared));   %Denominator of Equation 12
    %%%%%%%%%%%%%%%%%%%%%%%%%%%%%%%%%%%%%%%%%%%%%%%%%%%%%%%%%%%%%%%%%%%%%
    A_squared = double(ifft2(ifftshift(num./den)));             %Equation 12
    A_squared = abs(A_squared);
    %%%%%%%%%%%%%%%%%%%%%%%%%%%%%%%%%%%%%%%%%%%%%%%%%%%%%%%%%%%%%%%%%%%%%
    for k1 = 1:(2^nextpow2(Row));
        for l = 1:(2^nextpow2(Row));
            if A_squared(k1,l) <= 0
```

```
            A_squared(k1,l) = eps^2;
        end
    end
end
A_KN = double(sqrt(A_squared));
phi = double((((lambda*r_e)/sigma)*log(A_squared(2^nextpow2(Row)/2
      -(size(A0,1)/2-1):2^nextpow2(Row)/2
      +(size(A0,1)/2),2^nextpow2(Row)/2
      -(size(A0,1)/2-1):2^nextpow2(Row)/2+(size(A0,1)/2)))));
clear A_squared I I_tilde B2 C2 I_tilde2 i_tilde2 num center den;
%%%%%%%%%%%%%%%%%%%%%%%%%%%%%%%%%%%%%%%%%%%%%%%%%%%%%%%%%%%%%%%%%%%%%%%%
%
%Parts 3 & 4 of the algorithm
%
%%%%%%%%%%%%%%%%%%%%%%%%%%%%%%%%%%%%%%%%%%%%%%%%%%%%%%%%%%%%%%%%%%%%%%%%
A_tilde = A_KN(2^nextpow2(Row)/2-(size(A0,1)/2-1):2^nextpow2(Row)/2
          +(size(A0,1)/2),2^nextpow2(Row)/2
          -(size(A0,1)/2-1):2^nextpow2(Row)/2+(size(A0,1)/2));
%%%%%%%%%%%%%%%%%%%%%%%%%%%%%%%%%%%%%%%%%%%%%%%%%%%%%%%%%%%%%%%%%%%%%%%%
delta_A = double(A_tilde - A0);
%%%%%%%%%%%%%%%%%%%%%%%%%%%%%%%%%%%%%%%%%%%%%%%%%%%%%%%%%%%%%%%%%%%%%%%%
delta = double((abs(delta_A_old - delta_A)));
%%%%%%%%%%%%%%%%%%%%%%%%%%%%%%%%%%%%%%%%%%%%%%%%%%%%%%%%%%%%%%%%%%%%%%%%
error = max(max(delta));
delta_A_old = double(delta_A);
%%%%%%%%%%%%%%%%%%%%%%%%%%%%%%%%%%%%%%%%%%%%%%%%%%%%%%%%%%%%%%%%%%%%%%%%
%
%Part 5
%
%%%%%%%%%%%%%%%%%%%%%%%%%%%%%%%%%%%%%%%%%%%%%%%%%%%%%%%%%%%%%%%%%%%%%%%%
omega = double((lambda*z)/(2*pi*M));
T0 = double(delta_A.*exp(i*phi));
[L C] = size(T0);
B3 = ((2^nextpow2(Row) - L)/2);
C3 = ((2^nextpow2(Row) - C)/2);
T00 = double(padarray(T0,[B3 C3]));
%%%%%%%%%%%%%%%%%%%%%%%%%%%%%%%%%%%%%%%%%%%%%%%%%%%%%%%%%%%%%%%%%%%%%%%%
center2 = 0.5*(2^nextpow2(Row));
for k1 = 1:2^nextpow2(Row) ;
    for l = 1:2^nextpow2(Row) ;
        r_squared(k1,l) = double((k1-center2).^2 + (l-center2).^2);
    end
end
%%%%%%%%%%%%%%%%%%%%%%%%%%%%%%%%%%%%%%%%%%%%%%%%%%%%%%%%%%%%%%%%%%%%%%%%
G = double(exp(i*r_squared/(2*omega))); %Equation on top of page 13337
%%%%%%%%%%%%%%%%%%%%%%%%%%%%%%%%%%%%%%%%%%%%%%%%%%%%%%%%%%%%%%%%%%%%%%%%
t0 = fftshift(fft2(T0));
%%%%%%%%%%%%%%%%%%%%%%%%%%%%%%%%%%%%%%%%%%%%%%%%%%%%%%%%%%%%%%%%%%%%%%%%
center3 = 0.5*(2^nextpow2(Row));

for k1 = 1:(2^nextpow2(Row));
    for l = 1:(2^nextpow2(Row));
     u_squared1(k1,l) = double(((k1-center3)^2
                        +(l-center3)^2)/(((2^nextpow2(Row)))^2));
```

```
        end
    end
    %This is the analytical transform of G
    g = i*omega*sqrt(2*pi*sqrt(u_squared1)).*exp(-2*i*omega*pi*pi*u_squared1);
    %%%%%%%%%%%%%%%%%%%%%%%%%%%%%%%%%%%%%%%%%%%%%%%%%%%%%%%%%%%%%%%%%%
    e1 = double((1/(2*pi*omega))*g.*t0);
    E_1 = ifft2(ifftshift(e1));
    E_2 = conj(E_1);
    %%%%%%%%%%%%%%%%%%%%%%%%%%%%%%%%%%%%%%%%%%%%%%%%%%%%%%%%%%%%%%%%%%
    delta_I0 = double(abs(E_1.*E_2));
    delta_I = delta_I0(2^nextpow2(Row)/2-(size(A0,1)/2-1):2^nextpow2(Row)/2
              +(size(A0,1)/2),2^nextpow2(Row)/2
              -size(A0,1)/2-1):2^nextpow2(Row)/2+(size(A0,1)/2));
    clear deltaI0 e1 g center3 t0 G T00 C3 B3 A_KN A_tilde delta_A delta T0
    clear u_squared1 u_squared r_squared
    n = n + 1;
end
```